Uncertainty Modelling of High-precision Trajectories for Industrial Real-time Measurement Applications

Zur Erlangung des akademischen Grades eines

DOKTOR-INGENIEURS

von der Fakultät für
Bauingenieur-, Geo- und Umweltwissenschaften

Karlsruher Institut für Technologie (KIT)
genehmigte

DISSERTATION

von

Dipl.-Ing. Thomas Ulrich

aus

Neunkirchen(Saar)

Tag der mündlichen
Prüfung: 16.6.2016

Referentin:	Prof. Dr.-Ing. Maria Hennes
Korreferenten:	Prof. Dr.-Ing. Heinz Wörn
	Prof. Dr.-Ing. Dr.-Ing. E.h. Günter Schmitt

Karlsruhe (2016)

Contents

Summary **III**

Zusammenfassung **V**

1 Introduction **1**

2 Uncertainty and Kinematic Measurements **4**
2.1 Measurement Uncertainty 4
2.2 Kinematic Measurements 5
2.3 Bayesian Filtering 7

3 Process Description **9**
3.1 Simplified Movement 10
3.2 Known Movement at any Time 10
3.3 Known Movement in Advance 12
3.4 Unknown Movement in Advance 16

4 Measurement Model **18**
4.1 Laser Tracker 18
4.2 Multi Sensor Data Fusion 26

5 Kinematic Ground Truth **28**
5.1 Laser Tracer / Multilateration 29
5.2 Glass Scale / Linear Rail 34

6 Experiments and Results **44**
6.1 Simplified and Known Movement in Advance 44
6.2 Known Movement at any Time 48
6.3 Laser Tracer / Multilateration 52
6.4 Glass Scale / Linear Rail 62

7 Conclusion **71**

Bibliography **74**

Acronyms and Abbreviations **81**

A Papers **82**

Uncertainty modelling of real-time observation of a moving object: photogrammetric measurements. Metrologia, 52(2), 2015 83

Uncertainty estimation and multi sensor fusion for kinematic laser tracker measurements. Metrologia, 50(4), 2013 98

Summary

Within the field of large volume metrology, kinematic tasks such as the movement of an industrial robot have been measured using laser trackers. In spite of these kinematic applications, most research has focused on the uncertainty of static measurements. Accordingly, only very rough estimates have been available regarding the uncertainty of kinematic measurements and for this reason kinematic measurements merit further research.

It is, however, crucial to have a reliable uncertainty of the kinematic measurements, in order to assess spatiotemporal path deviations of the robot. As to potential applications, an approach capable of real-time was developed, in order to determine uncertainties of kinematic measurements. The approach estimates the uncertainties relying on Bayesian filters, and is in accordance with the *Guide to the Expression of Uncertainty in Measurement* which is widely accepted in this field.

The system model description within a Bayesian filter plays a very important role and therefore must be chosen with regard to the application and its requirements. Generally, a standard linear Kalman filter can be used to determine the uncertainty for simple movements. However, to include more than one system model, a hybrid system model filter can be applied, in order to cope with more complex movements. Nevertheless, all issues arising from the approximation of the movement, both within a standard Kalman filter or within a hybrid system model filter, can be avoided by including additional information from a robot control system into the uncertainty analysis method.

Beside the system model description, the measurement model plays an equally important role within the uncertainty determination along the trajectory. Therefore, a kinematic measurement model for a Leica AT901 laser tracker, with a beam steering mirror, was developed to entirely represent the measurements, given that experiments were done with this kind of laser tracker. However, using this model the entire analysis method can be demonstrated without any loss of generality. The kinematic model was developed by augmenting the geometric model with a kinematic part and a meteorological part. As the measurement uncertainty is entirely state dependent, it depends on the object's current position and velocity within the measurement volume. Therefore the measurement model needs to be recalculated within each time step and cannot be calculated in advance.

Even if the following work focuses on laser trackers, photogrammetric systems are also briefly considered, to show that the proposed analysis approach for kinematic measurements is equally valid for photogrammetric measurements.

Within this work, a kinematic measurement is taken to be the spatiotemporal measurement of a moving object so that the spatial measurements can be linked to other measurements through a common time axis. Prior methods to test kinematic laser tracker measurements have solely focused on the internal synchronization of the subsystems of a laser tracker i.e. the angle encoders and the distance measurement rather than on the object's trajectory. Consequently, the new derived probabilistic measurement model of a laser tracker was verified using two new kinds of kinematic ground truth.

PTB's multilateration system was used as a kinematic ground truth in conjunction with a six axis industrial robot. The multilateration system was made up of four synchronized laser tracers which are able to measure the same retro-reflector as the laser tracker. However, only a very small part of the laser tracker's capacity in terms of the velocity and acceleration could be tested, due to some limitations of the laser tracers and the robot in terms of its axis constellation. Because of the restricted space and the acceptance angle of the retro-reflector, the standard analysis method was prone to error. Therefore, the standard analysis method needed to be refined so that the multilateration system provided a ground truth. The strengthening of the network's geometry in general, was accomplished by introducing a new requirement matrix into the free-network adjustment of the standard analysis method. This new requirement matrix can also be applied to any other free-network adjustment, where the standard approaches for strengthening the geometry cannot be used. As the multilateration system could only deliver a ground truth up to 200 mm/s a new ground truth was developed which consists of a linear rail in conjunction with a glass scale. Consequently, no arbitrary trajectories can be chosen in contrast when using the multilateration system, but different motion profiles can be applied. Using this ground truth the derived probabilistic laser tracker measurement model could be verified up to a maximum velocity of roughly 5 m/s.

The results reveal that the internal alignment errors of a laser tracker and the environmental conditions are more important than additional kinematic influences if the delay time is relatively short and the movement is rather slow. However, it is hard to give a rule of thumb for which velocity or acceleration the kinematic influences play a significant role in the uncertainty, as the uncertainty is completely state dependent. As a result, it can be said that the uncertainty of the trajectory is smaller than compared to the manufactures rough approximation of the laser tracker used, when using the augmented measurement model in conjunction with the proposed method. Furthermore, the proposed method delivers a much more authentic uncertainty representation than the manufacturer's approximation and so mitigates the risk of a poor approximation. Therefore, deviations of a robot's path can be reliably assessed in real-time and the method has the potential to provide not only reliable corrections for robots during their movement, but also delivers their uncertainty.

Zusammenfassung

Im Bereich der Industrievermessung, auch bekannt unter der Bezeichnung *large volume metrology*, gibt es eine Vielzahl von kinematischen Anwendungen, wie zum Beispiel die Beobachtung von Industrieroboterbewegungen, wofür Laser Tracker eingesetzt werden. Trotz diesen kinematischen Anwendungen lag bisher der Forschungsschwerpunkt auf der Bestimmung von Unsicherheiten bei statischen Messungen, lediglich sehr grobe Schätzwerte zur Abschätzung der Unsicherheit bei kinematischen Messungen sind vorhanden. Somit gibt es einen großen Forschungsbedarf bei der Bestimmung von Unsicherheiten bei kinematischen Messungen.

Besonders bei der Beurteilung von raumzeitlichen Bahnabweichungen von Industrierobotern ist eine zuverlässige Angabe der Messunsicherheit wichtig, um Abweichung richtig zu interpretieren. Mit besonderem Blick auf zukünftige Anwendungen wie zum Beispiel einer sensorbasierten Bahnführung wurde ein echtzeitfähiger Ansatz zur Bestimmung der Unsicherheit bei kinematischen Messungen entwickelt. Dieser Ansatz basiert auf Bayes-Filtern und ist konform zu GUM, *Guide to the Expression of Uncertainty in Measurement*, welche eine weitverbreitete Norm im Bereich der Industrievermessung ist.

Im Hinblick auf die Anwendung sowie auf deren Bedingungen ist das Systemmodell in einem Bayes-Filter zu wählen. Im Allgemeinen kann ein herkömmlicher Kalman-Filter gewählt werden, um für einfache Bewegungen eine Unsicherheit zu schätzen. Für komplexe Bewegungen kann ein hybrider Filteransatz verwendet werden, der es erlaubt, mehr als nur ein Systemmodell zu definieren, umso die komplexe Bewegung besser beschreiben zu können. Alle Probleme, welche durch die Approximation der Bewegung in einem Kalman-Filter oder einem hybriden Systemfilter bedingt sind, können durch die Integration von Steuerinformation des Roboters vermieden werden.

Neben der Systemmodell-Beschreibung spielt auch das Messmodell eine wichtige Rolle bei der Bestimmung der Unsicherheiten kinematischer Messungen entlang einer Bahn. Daher wurde speziell für den Leica Laser Tracker AT901 ein kinematisches Messmodell entwickelt, welches die Besonderheit des Ablenkspiegels für den Laserstrahl berücksichtigt. Da alle Messungen mit einem AT901 durchgeführt wurden, jedoch kann der gesamte Auswerteansatz ohne Beschränkung der Allgemeinheit demonstriert werden. Die Mes-

sunsicherheit ist dabei abhängig von dem Zustand des Objektes, das bedeutet, sie ist abhängig von dessen Position und Geschwindigkeit im Messvolumen.

Auch wenn die vorliegende Arbeit sich hauptsächlich auf Lasertracker konzentriert, so werden auch photogrammetrische Messsysteme kurz angerissen und aufgezeigt, dass die vorgeschlagene Auswertemethodik auch für kinematische photogrammetrische Messungen übertragbar ist.

In dieser Arbeit wird eine kinematische Messung definiert als eine raum-zeitliche Messung eines bewegten Objekts, die sich über eine gemeinsame Zeitachse mit anderen Messungen verknüpfen lässt. Frühere Methoden zur Bestimmung der kinematischen Eigenschaft von Lasertrackern zielten hauptsächlich auf die interne Synchronität zwischen Distanz- und Richtungsmessung ab. Dem entsprechend musste das abgeleitete probabilistische Messmodell mittels neu entworfenen kinematischen Referenzen verifiziert werden.

Das Multilaterationssystem der PTB wurde als Referenz zusammen mit einem Industrieroboter genutzt und bestand aus vier Laser Tracern, welche untereinander sowie mit dem Lasertracker synchronisiert wurden. Jedoch konnten nur geringe Geschwindigkeiten getestet werden, bedingt durch die geringe Verfolgungsgeschwindigkeit der Laser Tracer und durch Bewegungsrestriktionen der Roboterachsen. Durch den geringen Öffnungswinkel des Retro-Reflektors und dem beengten Raum um den Roboter konnten die Laser Tracer nicht in einer für sie bestmöglichen Konstellation ausgerichtet werden. Dabei fiel auf, dass die übliche Auswertemethode des Multilaterationssystem fehleranfällig ist bei nicht optimalen Konstellationen. Deshalb wurde die Auswertemethode verbessert, indem eine neue Bedingungsmatrix in die Freie-Netzausgleichung eingeführt wurde, um die geometrische Struktur des Netzes zu stärken. Diese neue Bedingungsmatrix ist allgemein einsetzbar, somit auch überall dort, wo herkömmliche Ansätze zur Stärkung der geometrischen Struktur eines Netzes nicht anwendbar sind. Da die Höchstgeschwindigkeit nur 200 mm/s betrug, wurde zusätzlich eine weitere Referenz entwickelt und aufgebaut, welche aus einer präzisen Linearführung und einem Glasmaßstab besteht. Dadurch können zwar keine beliebigen Trajektorien gewählt werden, jedoch können verschiedene Bewegungsprofiele vorgegeben werden. Mittels dieser Referenz wurde das abgeleitete probabilistische Messmodell bis zu einer Geschwindigkeit von 5 m/s verifiziert.

Die Ergebnisse zeigen, dass die internen Achsfehler eines Lasertrackers und die meteorologischen Einflüsse wichtiger sind als kinematische Einflüsse, wenn die Totzeit relativ klein ist und nur langsame Geschwindigkeiten beobachtet werden. Des Weiteren zeigte sich, dass die Unsicherheit durch den vorgeschlagenen Ansatz in Verbindung mit dem kinematischen Lasertracker Modell im Vergleich zu der groben Herstellerabschätzung geringer wird. Wichtiger jedoch ist, dass der neue Ansatz die systematischen Abweichungen besser repräsentiert als die Abschätzung des Herstellers und somit eine verlässlichere Unsicherheit berechnet. Dieses wird dadurch erreicht, dass die Bewegung des Objekts berücksichtigt wird. Demzufolge ist der neue Ansatz besser geeignet, um in Echtzeit Roboterabweichungen zu beurteilen und bietet somit das Potenzial, auch Korrekturwerte während einer Roboterbewegung liefern zu können.

Chapter 1

Introduction

Within the field of industrial metrology, also known as large volume metrology (LVM), there are different kinds of kinematic tasks such as the observation of an industrial robot's movement or the tracking of a hand-held surface scanner. According to [EN ISO 9283, 1998] an industrial robot, should be tested up to a speed of 1.6 m/s. While it is evident, that the uncertainty of the resulting measurements must be smaller than the expected uncertainty of the robot it is also important to note that, the measurement system to perform the measurements is not further specified. The spatio-temporal synchronization of two six axis industrial robots and one extrusion press to fly cutting off spatially curved extrusion profiles was presented in [Munzinger et al., 2006]. Here, the dynamic behaviour of the robots were identified as one of the main issues which decreases the accuracy and accordingly the current behaviour should be taken into consideration.

However, to reliably assess a dynamic path deviation of an industrial robot, observed during the movement, it is crucial to first answer the question: What's the uncertainty in a trajectory measured kinematically?

Because it is possible that the measurement uncertainty is not sufficient to do any assessment of the deviation care should be taken to not defraud the robot by relying upon the assumption that the measurement uncertainty is sufficient. There is a wide range of industrial robots, including articulated robots, consisting of revolute (or rotary) joints, and robots consisting of linear axis, also known as parallel kinematic, for example as shown in Crothers et al. [2010]. In particular small hexapods are accurate to a few µm [Phy, 2012] which makes the calibration of the motion process quite difficult. Due to the fact that the measurement uncertainty is state dependent, as derived in the following, it depends on the object's velocity and position in the measurement volume. Therefore, this might mean that there are parts along the trajectory which can be assessed and others which cannot, as the path deviation of the robot is too small in comparison to the uncertainty.

In order to react in an appropriate way, by stopping the process or applying path corrections, it is important that the method, to determine the measurement uncertainty, is real-time capable. Furthermore, the analysis method should be able to include additional information. This might be derived from additional sensors attached to the robot or this could be the control information of the robot itself. In addition, the probabilistic measurement system model must be extremely accurate in a great measure to determine a thorough/authentic uncertainty in the trajectory.

Common LVM instruments for measuring kinematic movements are photogrammetric systems and laser trackers [Loser, 2004; Luhmann et al., 2013]. Photogrammetric systems are often made up of two or more cameras for observing kinematic movements. This is why an initial guess about the uncertainty can be derived by taking into account the residuals, resulting from the overdetermined equation system. Despite the kinematic applications, most work to date on the evaluation of laser tracker measurement uncertainty has focused on static measurements and the uncertainties in kinematic measurements remain unclear. As a result, the following work focuses on laser trackers, however photogrammetric systems are briefly revisited, in order to show how the previously mentioned approach can be integrated into the proposed analysis method for kinematic measurements.

The laser tracker itself is a device which tracks and measures in spherical coordinates the 3D positions of a moving retro-reflector. These spherical coordinates are made up of the distance to the retro-reflector, which is measured by either an interferometer (IFM) or an absolute distance meter (ADM), and the two directional components are measured by two angle encoders. The outgoing laser beam is returned by the retro-reflector to the laser tracker where a part of the beam is directed onto a position sensitive device (PSD). Accordingly, any lateral movement of the reflector generates an offset signal on the PSD which is then used in a control loop to point the laser beam automatically back to the centre of the reflector, thereby generating real-time distance and angle readings to the reflector. As the offset signal at the PSD is also used to improve the angle encoder readings, the laser tracker is, in principal, able to measure kinematic movements.

Even if, laser trackers are capable of measuring kinematic movements, the current products are only specified for static measurements in terms of their uncertainty, but they are specified in terms of the maximal object velocity and acceleration [Leica Geosystems AG, 2009c; Hexagon Metrology, 2015; API Automated Precision Inc., 2011, 2013; FARO Technologies Inc., 2010, 2012]. However, there are some kind of uncertainty estimates for kinematic measurements but these are only very rough approximations, which even may lead to false assumptions, as will be shown. This is why kinematic measurements merit further research.

A major part of the analysis method's deduction and some early experiments have already been published in Ulrich [2013]; Ulrich and Irgenfried [2014]; Ulrich [2015]. However, the verification of the derived measurement model as well as the realization of different kinematic ground truths have not yet been published. In order to present the subject entirely also the main parts of these publications will be revised in the following.

In general the uncertainty of a kinematic measurement can be determined by using Bayesian filters. However, in order to apply a Bayesian filter, a system model and a measurement model must be available. The system model can be derived differently and so it is governed by decisions made in advance, e.g. about the modelling and approximations, as its result will be. As the focus is on laser trackers a static measurement model was augmented in order to reflect its kinematic properties.

The entire analysis method was tested in experiments using a laser tracker in conjunction with a six axis industrial robot, consisting of revolute (or rotary) joints. It can be said that the analysis method can be used to improve the uncertainty determination and delivers an authentic uncertainty of the robot's trajectory.

Due to the fact that the analysis method is highly dependent on the measurement model, it was verified using two different kind of ground truths. One ground truth was made up of four laser tracer, the multilateration system of the Physikalisch-Technische Bundesanstalt (PTB), which was synchronized with a laser tracker, and the retro-reflector was moved along certain trajectories using an industrial robot. Because of a special configuration of the laser tracers and the trajectory the standard analysis method was prone to error. This was shown by the weak form analysis for geodetic networks which is based on eigenvalue analysis. Because of that, a refined method needed to be developed, in order to get reliable multilateration results which could be regarded as a ground truth for laser tracker measurements. As only rather slow velocities could be tested using the multilateration system, a second ground truth was developed, consisting of a linear rail and a glass scale. Using this ground truth the measurement model could be tested and verified up to velocities at 5 m/s.

As the entire analysis method could be verified the next steps would be to implement a sensor guided robot experiment. Furthermore, the robot model used should be enhanced in order to get a better understanding of the observed path deviations.

Chapter 2

Uncertainty and Kinematic Measurements

In order to use a measurement to make an explicit assessment of a deviation, it is vital to associate that measurement with a statement of reliability which expresses its uncertainty, so that the occurred deviation can be checked for significance. A widely accepted framework to evaluate measurement uncertainties is provided by the Guide to the Expression of Uncertainty in Measurement (GUM).

There are a number of analysis techniques to determine the uncertainty of kinematic measurements for different kinds of applications. However, the most of them cannot be applied for real-time purposes or they have strong requirements about the kinematic process [Ulrich, 2013].

2.1 Measurement Uncertainty

To make a thorough assessment of spatiotemporal deviations between the planed trajectory and the one observed by a measurement instrument, e.g. laser tracker, it is essential to have a statement of uncertainty expressing the reliability of the measurements. In GUM a probability density function (PDF) is applied to express the uncertainty of a quantity ζ. In general, the uncertainty evaluation can be divided into forward-uncertainty evaluation and inverse-uncertainty evaluation [Sousa and Forbes, 2007]. According to Ulrich [2015], the kinematic uncertainty evaluation belongs to the latter case. Thereby, the desired parameter β is only indirectly related to the measured quantities ζ by a function $f(\beta)$. Here, the Bayesian paradigm can be used to derive a density of β with respect to the observed information ζ. This results in the posterior density $p(\beta|\zeta)$ which

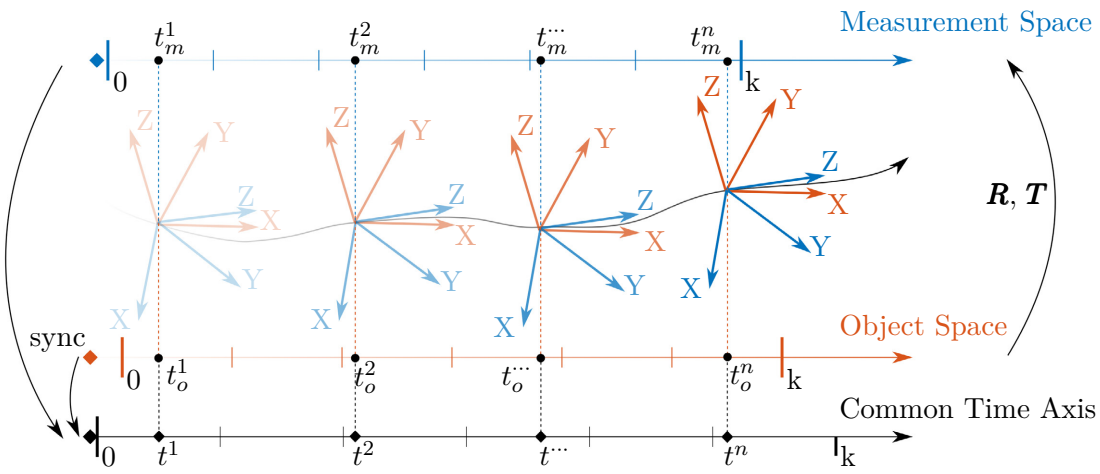

Figure 2.1: The kinematic measurement principle, relating the measurement space to the object space including the common time axis, according to Ulrich [2015].

is based on the quantities observed and any prior information. By using the Bayesian theorem this posterior can be determined as follows:

$$p(\beta|\zeta) = \frac{p(\zeta|\beta)\ p(\beta)}{p(\zeta)} \tag{2.1}$$

Here, $p(\zeta|\beta)$ is the likelihood function and $p(\beta)$ is the prior density including all information about the parameter β available prior to the observations ζ or from other, independent sources.

If systematic influences can be inferred, but cannot be measured directly, then the Bayesian statistic is well-suited to determining the uncertainty, according to Lira and Wöger [2006]. Therefore, the Bayesian statistic is ideally suited to the analysis of kinematic measurements' uncertainties given that the velocity of the object causes a systematic effect which cannot be measured directly using a common LVM instrument such as a laser tracker or a photogrammetric system.

2.2 Kinematic Measurements

The term 'kinematic measurement' can be construed in different ways as Foppe et al. [2004] showed. However, in this report it is taken to be the spatiotemporal measurement of a moving object so that the spatial measurements can be linked to other measurements through a common time axis, the principle can be seen in figure 2.1 as shown in Ulrich [2015]. Generally, the analysis of the moving object is done in the object space or any other space, which is different to the measurement space in terms of its reference system definition. Therefore the measurements observed need to be transformed into

the appropriate space. Besides the geometrical transformation, the alignment of the time axis also needs to be taken in to account due to the fact that these may have different zero points, scales or drifts. In figure 2.1 these time axes are aligned using a synchronization impulse. A point in time is t, the superscript indicates the number of the point, the subscript m stands for the measurement space and the subscript o stands for the object space. The geometrical transformation between each of the spaces is defined by the rotation matrix $\boldsymbol{R}$ and the translation vector $\boldsymbol{T}$. Assuming that the geometrical transformation parameters are known, then a first order approximation of a kinematic measurement can be expressed as follows

$$\boldsymbol{\Psi} = M\left(\boldsymbol{V}\right) + \boldsymbol{V} \cdot dt \cdots . \tag{2.2}$$

The time offset between the time axes is dt. The result of the vector function M are the measurements, with respect to the velocity $\boldsymbol{V}$ and the final point on the trajectory is $\boldsymbol{\Psi}$. Using equation (2.2) it becomes clear, why the determination of the uncertainties of kinematic measurements should be treated as an inverse uncertainty evaluation. This is due to the fact that the process parameter $\boldsymbol{V}$ affects the desired quantity but cannot be measured directly using a common LVM measurement instrument like a laser tracker or a photogrammetric system. Accordingly, the uncertainty estimation of kinematic measurements needs to involve the kinematic process.

In principle there are interferometers designed to measure solely velocity e.g. the velocity interferometer system for any reflector (VISAR) [Neyer, 1986]. However, to date, no commercially available laser tracker additionally includes a velocity interferometer. In addition, a velocity interferometer does not measure a 3D velocity vector, which is needed for the analysis, it measures solely a part of the velocity which is in line of sight.

For kinematic measurements there are a number of analysis methods for different applications. However, these often do not work in real-time or they do not track the kinematic behaviour. Instead it is assumed that the kinematic behaviour is known in advance [Ulrich, 2013]. For example that the object will move at a constant velocity. Furthermore, as shown in Ulrich [2015] a straightforward approach, using the most recent measurement and the measurement one time step earlier to derive the velocity results in a velocity estimate which is too inaccurate. Especially when the measurement frequency is higher than 1 Hz, which is quite common in the LVM to observe movements.

Nonetheless, a very common approach to include the object's kinematic is called the state-space approach. The state vector of this approach is made up of all relevant information to describe the state of the object. Within kinematic laser tracker measurements, this information could be e.g. the retro-reflectors position, velocity and acceleration. According to Ulrich [2015] the state space equations of a non-linear stochastic discrete-time state space model can be expressed as

$$\boldsymbol{x}_{t+1} = f_t\left(\boldsymbol{x}_t, \boldsymbol{u}_t, w_t\right) \tag{2.3}$$

$$\boldsymbol{z}_t = h_t\left(\boldsymbol{x}_t, v_t\right). \tag{2.4}$$

The system model function is f, its system process noise is denoted using w, $\boldsymbol{x}$ stands for the state vector and $\boldsymbol{u}$ denotes the control input. The measurement function h, also includes the measurement noise v. In general the state space approach can be analysed using Bayesian filters while focussing on the state vector $\boldsymbol{x}$ under investigation.

2.3 Bayesian Filtering

Bayesian filters are optimal non-linear state estimators and so are ideally suited to determining the PDF of the state vector $\boldsymbol{x}(t)$ conditioned on all information given at time t. This information consists of the knowledge about the system's prior state, the control inputs as well as the measurements available. Accordingly, the requirements postulated by GUM are fulfilled by a Bayesian filter and this filter therefore is particularly suitable for determining uncertainties of kinematic measurements in real-time [Ulrich, 2015].

Using the information set I_t at time t the required conditional state PDF is $p(x_t|I_t)$. The information set is made up of

$$I_t = \{\boldsymbol{z}_{1:t}, \boldsymbol{u}_{1:t-1}\}. \tag{2.5}$$

Here, $\boldsymbol{u}_{1:t-1}$ are all control inputs up to time $t-1$ and $\boldsymbol{z}_{1:t}$ are all measurements up to time t [Bar-Shalom et al., 2001]. Taking into account independent process and measurement noise sequences and further taking the state vector to be a Markov process then the conditional PDF of the state vector $\boldsymbol{x}(t+1)$ at time $t+1$ can be expressed using the Bayes' formula as

$$p(\boldsymbol{x}_{t+1}|I_{t+1}) = \frac{1}{c} p(\boldsymbol{z}_{t+1}|\boldsymbol{x}_{t+1})\ p(\boldsymbol{x}_{t+1}|I_t, \boldsymbol{u}_t), \tag{2.6}$$

here, $c = p(\boldsymbol{z}_{t+1}|I_t, \boldsymbol{u}_t)$ is the normalization constant as shown in Ulrich [2015]. Equation (2.6) is known as the state update equation of a Bayesian filter [Bar-Shalom et al., 2001; Thrun et al., 2005]. As a Markov process it is assumed that the state $\boldsymbol{x}_t$ is complete and that no future state is influenced by a variable prior to $\boldsymbol{x}_t$ [Thrun et al., 2005]. However, for the following analysis it is worth mentioning that state-dependent process and measurement noise are permitted. For the common LVM instruments, like laser trackers and photogrammetric systems this is especially important as their measurement uncertainty is highly state depended, as can be seen in chapter 4. According to Bar-Shalom et al. [2001] the Chapman-Kolmogorov equation can be used to calculate the PDF prediction $p(\boldsymbol{x}_{t+1}|I_t, \boldsymbol{u}_t)$ as follows

$$p(\boldsymbol{x}_{t+1}|I_t, \boldsymbol{u}_t) = \int p(\boldsymbol{x}_{t+1}|\boldsymbol{x}_t, \boldsymbol{u}_t)\ p(\boldsymbol{x}_t|I_t)\ d\boldsymbol{x}_t. \tag{2.7}$$

Commonly, a Bayesian filter consists of two steps, the prediction step using equation (2.7) and the update step using equation (2.6). For these steps two models are required, the

system evolution over time, is described in a system model and relating the measurements to the state vector is carried out using a measurement model. To use these models in a Bayesian filter they must be available in a deterministic form and in a probabilistic form [Ristic et al., 2004].

Chapter 3

Process Description

Within the last chapter it was deduced that the uncertainty estimation of kinematic measurements needs to be considered an inverse uncertainty evaluation. This is due to the fact that the estimation depends on additional process information, e.g. the velocity of the object being observed, which cannot be measured by any common laser tracker or photogrammetric system in the LVM. Nor can this information be derived with sufficient variance, as shown in Ulrich [2015]. Furthermore, the velocity alone is not necessarily sufficient to describe the general kinematic behaviour. Therefore, the uncertainty estimation should involve the kinematic process.

Taking into consideration the kinematic task, the kinematic process description can be divided into different application scenarios. This means the description can be highly complex or relatively simple depending on the amount of additional knowledge available of the kinematic task.

For all applications, the movement can either be described in a continuous time state, whereby the object state equations must then be transformed into the corresponding discrete time equations, or the movement can be directly modelled using discrete time equations. Using discrete time equations result in process noise covariance matrices which are easier to interpret, but are slightly different to the one transformed from the continuous time state. However fundamentally, both methods approximate the movement differently, the latter assumes a piecewise constant noise whereas the former assumes a continuous-time noise. Furthermore, the difference between the covariance matrices of both methods can be considered to be marginal as shown in Ulrich [2015] and Bar-Shalom et al. [2001].

However, considering kinematic measurements in the LVM these are discretized observations of the object's movement, which is continuous so it appears to be more appropriate to describe the process continuously and the measurements in a discrete model. Even if

both methods are just approximations of the real kinematic process and the differences are marginal, as shown in Ulrich [2015].

3.1 Simplified Movement

Considering the example of a kinematic measurement of a linear rail where the carriage moves at a constant velocity. If the acceleration time at the beginning and the deceleration time at the end of the movement are negligible then the whole movement can be described using a single constant velocity model. The constant velocity can be expressed in a continuous white-noise acceleration model as in Bar-Shalom et al. [2001]. In this case the state space vector $\boldsymbol{x} = [x\, y\, z\, \dot{x}\, \dot{y}\, \dot{z}]^\intercal$ consists of the position and the velocity. The discrete-time state equation of this model is

$$\boldsymbol{x}_{t+1} = \begin{bmatrix} \boldsymbol{I}^{3\times3} & \Delta t\, \boldsymbol{I}^{3\times3} \\ \boldsymbol{0} & \boldsymbol{I}^{3\times3} \end{bmatrix} \boldsymbol{x}_t + \boldsymbol{w}_t \tag{3.1}$$

with the sampling period Δt and the covariance of this discrete-time process noise w_t can be expressed as

$$\operatorname{cov}(\boldsymbol{w}_t) = \begin{bmatrix} \frac{1}{3}\Delta t^3\, \boldsymbol{I}^{3\times3} & \frac{1}{2}\Delta t^2\, \boldsymbol{I}^{3\times3} \\ \frac{1}{2}\Delta t^2\, \boldsymbol{I}^{3\times3} & \Delta t\, \boldsymbol{I}^{3\times3} \end{bmatrix} \tilde{q}. \tag{3.2}$$

The matrix is derived by discretizing the continuous time model with additional noise, using the inverse Laplace transformation as proposed in Bar-Shalom et al. [2001] and Ulrich [2015]. Here it is assumed that the power spectral density of the process noise $\tilde{q}$ is constant. This model is ideally suited to be used in a common Kalman filter as a simple Bayes filter e.g. in Ulrich [2015].

However, as it is obvious that the model, on which the filter is based, does not accurately represent the kinematic behaviour of the carriage at all times – e.g. the acceleration time and brake time –, the process noise covariance must be artificially enlarged to include these parts too. This technique can be found throughout in the literature e.g. Simon [2006] but it can also result in wrong state estimates as shown in Simon [2006]; Ulrich [2013] or at least it decreases the performance during the parts the process description was designed to. Due to the fact that the uncertainty estimation relies on this derived information, uncertainty would increase.

3.2 Known Movement at any Time

Assuming that there is synchronization between the measurement system, e.g. a laser tracker, and the control system of an industrial robot and that the robot control data are accessible, then they can be incorporated into the analysis method. However, beside these data a probabilistic model also needs to be provided for the incorporation, as can be seen

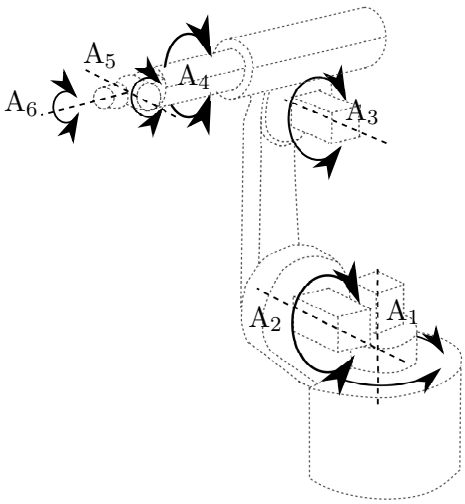

Figure 3.1: Axis configuration of a KUKA KR 5 arc robot according to[KUKA, 2011]

in equation (2.3). Due to the incorporation, all problems arising from predefined motion models in Bayesian filters of the tracking problem can be avoided, see the discussion in section 3.1,3.3 and 3.4. This is a big advantage especially if the robot moves along arbitrary trajectories with complex kinematic behaviour.

Considering as an example the synchronization of a six axis robot manipulator KUKA KR 5 arc having six revolute joints and a laser tracker which is measuring a retro reflector attached to the robot's tool centre point (TCP). Figure 3.1 depicts a sketch of a KUKA KR 5 arc with its six axis. The position and orientation of the TCP with respect to the robot's base can be calculate at any time t with the current joint angles $\boldsymbol{\vartheta}_t = [\vartheta_1, \ldots, \vartheta_6]_t$ readings using sequential homogeneous matrix multiplication

$$\prod_{i=1}^{6} \boldsymbol{\Gamma}_i^{i-1} = \begin{bmatrix} \boldsymbol{R}^{3\times 3} & \begin{matrix} x \\ y \\ z \end{matrix} \\ \mathbf{0} & 1 \end{bmatrix} \Rightarrow \begin{bmatrix} x \\ y \\ z \\ \phi \\ \theta \\ \psi \end{bmatrix} \tag{3.3}$$

also known as forward transformation. Here $\boldsymbol{\Gamma}_i^{i-1}$ describes the transformation from coordinate frame attached to joint $i-1$ to the coordinate frame attached to i. The position of the TCP is (x, y, z) and its orientation –roll, pitch, yaw– is described with the angle parameters (ϕ, θ, ψ) derived of the rotation matrix $\boldsymbol{R}$. The transformation matrix

$\boldsymbol{T}_i^{i-1}$ is replaced with the Denavit-Hartenberg matrix containing the geometry parameter of the robot which is

$$\boldsymbol{D}_i^{i-1} = \begin{bmatrix} \cos\vartheta_i & -\sin\vartheta_i \cos\alpha_i & \sin\vartheta_i \sin\alpha_i & \cos\vartheta_i\, a_i \\ \sin\vartheta_i & \cos\vartheta_i \cos\alpha_i & -\cos\vartheta_i \sin\alpha_i & \sin\vartheta_i\, a_i \\ 0 & \sin\alpha_i & \cos\alpha_i & l_i \\ 0 & 0 & 0 & 1 \end{bmatrix}. \tag{3.4}$$

Due to the fact that all joints are revolute joints, the link offset l_i is a constant parameter of the robot model describing the distance from the origin frame $i-1$ along the z_{i-1} axis to the intersection with the x_i axis. The joint angle is ϑ_i and is defined as the rotation about the z_{i-1} axis between the x_{i-1} axis and x_i axis. The distance parameter a_i is the link length measured along the x_i axis between the z_{i-1} axis and the z_i axis. α_i is a rotation about the x_i axis until the z_{i-1} axis is parallel to the z_i axis. More details about the Denavit-Hartenberg matrix and its definition can be found in Corke [2011]; Craig [2005]. In addition to these parameters there are further geometric calibration parameters which need to be taken into account. According to Wiest [2001] these are per frame, the index offset which is a deviation of the zero position, the tilt deviation which means that the two successive z axis are not parallel to each other and the link deviation which defines the deviation of two successive axis in all three coordinate directions from their nominal values. Alongside these geometrical errors, there are non-geometrical influences which need to be considered, the most importance are the temperature and the transmission elasticity according to Wiest [2001].

The joint variable can also be determined with respect to the forces and torques applied by using the forward dynamic model. This model includes the friction force, the gravity loading, the joint-space inertia matrix and the Coriolis and centripetal coupling matrix. Within this list, the gravity is the dominant term and needs to be taken into account at all times i.e. when the robot is stationary, or moving along a trajectory [Corke, 2011; Craig, 2005].

3.3 Known Movement in Advance

Assuming that the movement of an industrial robot along a complex trajectory should be monitored, but only the starting point can be synchronized, this means there is no additional information about the robot control system available. However, the movement of the robot is known in advance, because the trajectory has to be programmed in advance. To avoid including the model inaccuracy i.e. one model cannot sufficiently describe the whole complex trajectory, a hybrid system estimator can be utilized. It estimates the continuous state of the robot and the discrete system model. As shown in Ulrich [2013], the hybrid system estimator has been thoroughly researched particularly in the field of air traffic control [Hwang et al., 2006; Rong Li and Jilkov, 2003; Bar-Shalom et al., 2001; Blackman and Popoli, 1999], autonomous vehicles and driving assistance systems [Althoff, 2010]. Within a hybrid system estimator, the most probable system models

are included to represent the robot's kinematic behaviour along the whole trajectory not only along the largest parts, see section 3.1. These system models can be e.g. an acceleration model, a model for a constant velocity, or a constant turn model to describe a curve and so on. In the following, the continuous dynamic of the hybrid system is modelled using difference equations and the discrete-state dynamic is modelled applying a finite Markov chain as proposed e.g. in Hwang et al. [2006]. Therefore, the common state space equations (2.3) and (2.4) needs to be adjusted as

$$\boldsymbol{x}_{t+1} = f_t^i\left(\boldsymbol{x}_t, w_t^i\right) \tag{3.5}$$

$$\boldsymbol{z}_t = h_t^i\left(\boldsymbol{x}_t, v_t^i\right) \tag{3.6}$$

to represent a discrete-time stochastic hybrid system. The system model function of model i is f^i and its process noise is w^i. h^i is the measurement model function of model i with its measurement noise v^i. Here the state space vector is $\boldsymbol{x}$ and $\boldsymbol{z}$ are the measurements.

A widely used hybrid system estimator is the Interacting Multiple Model (IMM) filter because of its performance compared with other hybrid system estimators [Rong Li, 2000; Hwang et al., 2006]. An IMM filter approximates the required posterior density $p\left(\boldsymbol{x}_t|\boldsymbol{z}_t\right)$ using a weighted sum of Gaussian density functions as

$$p\left(\boldsymbol{x}_t|\boldsymbol{z}_t\right) \approx \sum_{i=1}^{r} g_t^i \mathcal{N}\left(\boldsymbol{x}_t^i; \hat{\boldsymbol{x}}_t^i, \boldsymbol{P}_t^i\right) \tag{3.7}$$

$$\text{with} \quad \sum_{i=1}^{r} g_t^i = 1.$$

Here the model-conditioned state estimate is $\hat{\boldsymbol{x}}_t^i$ with its covariance $\boldsymbol{P}_t^i$ and the weights are g_t^i. The exponent i denotes the model which is governed by the finite Markov chain as

$$\boldsymbol{\mu}_{t+1} = \boldsymbol{\Pi}\boldsymbol{\mu}_t. \tag{3.8}$$

Here, r is the count of the discrete models in this chain. The vector $\boldsymbol{\mu} \in \mathbb{R}^r$ contains the model probabilities and $\boldsymbol{\Pi}$ is the model transition probability matrix of the dimension $\boldsymbol{\Pi} = \{\pi_{ij}\} \in \mathbb{R}^{r\times r}$ which also needs to be defined in advance with respect to the real process. An IMM filter calculates the final hybrid state estimate as

$$\hat{\boldsymbol{x}}_{t+1} = \sum_{i=1}^{r} \hat{\boldsymbol{x}}_{t+1}^i p\left(m_{t+1}^i|\boldsymbol{z}_{1:t+1}\right) \tag{3.9}$$

The model probabilities are $p\left(m_{t+1}^i|\boldsymbol{z}_{1:t+1}\right)$, which are comparable to the weights in equation (3.7). Under the condition that the model at time $t+1$ is m_{t+1}^i the model-conditioned state estimate of $\boldsymbol{x}_{t+1}$ can be calculated as

$$\hat{\boldsymbol{x}}_{t+1}^i = \int \boldsymbol{x}_{t+1}\, p\left(\boldsymbol{x}_{t+1}|\boldsymbol{z}_{t+1}, m_{t+1}^i\right) d\boldsymbol{x}_{t+1}, \tag{3.10}$$

using the model estimator of model i according to Hwang et al. [2006]. This can be directly compared to an optimal state estimator with respect to the minimum mean-square error of a common Bayesian filter as shown in Ulrich [2015].

To sum up the hybrid filter IMM is a weighted sum using the model probabilities to also include the states of the process during the transition from one model to another model and so to reduce the number of models. Because of the inclusion of the transition phase, there is no need to include further models, to describe the transition from one model to another model precisely. This, on the other hand, may even deteriorate the overall performance, as the transition phase is rather short, compared to the others. As mentioned above, the most probable system models are included to represent the process, meaning also the models representing the longest phase. It is clear that an IMM filter's performance must decrease if the mismatch between the modelled kinematic process behaviour and the real kinematic movement increases. In Rong Li [1994] it was shown that adding more models does not guarantee a better performance as the mismatches alone may increase, which may further deteriorate the performance. This becomes clear when taking into account equation (3.16) as they just represent a 'relative' probability with respect to the subspace of the chosen models. However, the issue that a common IMM or other hybrid system filters has a fixed structure which needs to be defined in advance and therefore is not able to adapt itself is further discussed in 3.4.

The work of an IMM filter can be subdivided into three steps, an interaction and mixing step, a filter step and a state estimation step. The following description is loosely based on the derivation of Bar-Shalom et al. [2001] and Hwang et al. [2006].

Assuming that all models can be implemented using a Kalman filter, then new initial states and covariance matrices are calculated within the interaction and mixing step to be used in each filter. The mixed means and covariance matrices for each filter can be calculated as

$$\hat{\boldsymbol{x}}_t^{0j} = \sum_{i=1}^{r} \hat{\boldsymbol{x}}_t^i \mu_{t|t}^{ij} \tag{3.11}$$

$$\boldsymbol{P}_t^{0j} = \sum_{i=1}^{r} \left\{ \boldsymbol{P}_t^i + \left[\hat{\boldsymbol{x}}_t^i - \hat{\boldsymbol{x}}_t^{0j} \right] \left[\hat{\boldsymbol{x}}_t^i - \hat{\boldsymbol{x}}_t^{0j} \right]^\intercal \right\} \mu_{t|t}^{ij} \qquad \text{j=1,...,r,} \tag{3.12}$$

as proposed in Ulrich [2013]. Here the state estimate is $\hat{\boldsymbol{x}}_t^i$ and the covariance is $\boldsymbol{P}_t^i$ which are results of the Kalman filter i after the measurement update at time t. The conditional probability $\mu_{t|t}^{ij}$ includes the transition probability that the system made the transition from model i to j at time $t+1$ which can be determined with

$$\begin{aligned} \mu_{t|t}^{ij} &= \frac{\pi_{ij} \mu_t^i}{\overline{c}_j} \\ \overline{c}_j &= \sum_{i=1}^{r} \pi_{ij} \mu_t^i. \end{aligned} \tag{3.13}$$

Here $\overline{c}_j$ is the normalization constant and the model probability of model i at time t is μ_t^i. Hwang et al. [2006] introduced an improvement of the IMM filter by reducing the model estimation delay. This was achieved by increasing the difference between the likelihood of the correct model and the others. The improved version is called Residual-Mean Interacting Multiple Model (RMIMM). However, in Ulrich [2013] no big difference between the common IMM filter and the RMIMM filter was detected for the application observing an industrial robot with a laser tracker.

As presented in Ulrich [2015] the filter step includes the common prediction and update step of a Kalman filter which can be briefly expressed as

$$\left[\hat{\boldsymbol{x}}_{t+1}^{-,i}, \boldsymbol{P}_{t+1}^{-,i}\right] = \mathrm{KF}_p\left(\hat{\boldsymbol{x}}_t^{0j}, \boldsymbol{P}_t^{0j}, \boldsymbol{A}_t^i, \boldsymbol{Q}_t^i\right) \tag{3.14}$$

$$\left[\hat{\boldsymbol{x}}_{t+1}^{i}, \boldsymbol{P}_{t+1}^{i}\right] = \mathrm{KF}_u\left(\hat{\boldsymbol{x}}_{t+1}^{-,i}, \boldsymbol{P}_{t+1}^{-,i}, \boldsymbol{z}_{t+1}, \boldsymbol{H}_{t+1}^i, \boldsymbol{\Sigma}_{t+1}^i\right). \tag{3.15}$$

Here the prediction step of a Kalman filter is denoted using KF_p and the update step using KF_u. The matrix $\boldsymbol{A}$ is the transition matrix of the system model m^i with its covariance matrix $\boldsymbol{Q}$. The measurement matrix is represented by $\boldsymbol{H}$ and the covariance matrix of the measurement model is denoted using $\boldsymbol{\Sigma}$. Here, the predicted state estimate is $\hat{\boldsymbol{x}}_{t+1}^{-,i}$ and the predicted covariance is $\boldsymbol{P}_{t+1}^{-,i}$ which are results of the Kalman filter applying model i. In equation (3.14) and (3.15) a generic brief expression of a Kalman filter is shown, as a realization depends on the motion model and the chosen Kalman filter. Accordingly, the Kalman filter equations are also effected.

Furthermore, the needed model probability, within an IMM filter, can be calculated as

$$\mu_{t+1}^j = \frac{1}{c}\Lambda_{t+1}^j \overline{c}_j \qquad j = 1, \ldots, r \tag{3.16}$$

using the normalization constant

$$c = \sum_{j=1}^{r} \Lambda_{t+1}^j \overline{c}_j.$$

For each model the likelihood is required which can be determined as

$$\Lambda_{t+1}^j = \mathcal{N}\left(\boldsymbol{d}_{res.t+1}; 0, \boldsymbol{S}_{t+1}^j\right). \tag{3.17}$$

Here $\boldsymbol{S}_{t+1}^j$ is the innovation covariance matrix in the KF update step of model m^j and $\boldsymbol{d}_{res.t+1}$ are the appropriate residuals at time $t+1$.

The final step, the state estimation step, calculates the combined state estimate and covariance over all filter results as a weighted sum as follows

$$\begin{aligned}
\hat{\boldsymbol{x}}_{t+1} &= \sum_{j=1}^{r} \mu_{t+1}^j \hat{\boldsymbol{x}}_{t+1}^j \\
\boldsymbol{P}_{t+1} &= \sum_{j=1}^{r} \mu_{t+1}^j \left\{\boldsymbol{P}_{t+1}^j + \left[\hat{\boldsymbol{x}}_{t+1}^j - \hat{\boldsymbol{x}}_{t+1}\right]\left[\hat{\boldsymbol{x}}_{t+1}^j - \hat{\boldsymbol{x}}_{t+1}\right]^{\mathsf{T}}\right\}.
\end{aligned} \tag{3.18}$$

3.4 Unknown Movement in Advance

Even if there is no immediate application for a variable hybrid system model estimator in conjunction with an industrial robot and a laser tracker, it is briefly presented for the sake of completeness. An IMM filter describes non manoeuvre motion and different manoeuvres in different motion models with a fixed set of models. These models represent possible system behaviour patterns, which are highly interesting in regard to the problem under consideration. In a general description of a hybrid system, the system mode refers to a real-world behaviour pattern and a model refers to a mathematical representation of the system at a certain accuracy level. The model set M_{set} usually has fewer elements than the mode space B and an element of M_{set} is usually just an approximated description of a mode, up to a certain accuracy level [Rong Li, 2000].

On the one hand the performance of an IMM filter depends largely on the type of models used, on the other hand it also depends on the number of models used in the IMM. Rong Li [1994] showed that the use of more models and filters does not guarantee performance improvements. Including more models into M_{set} may increase the mismatch between M_{set} and B_t the system modes at time t and lead to performance deterioration.

For the scenario where a person carries a reflector, it can be assumed that there will be a large mode space and that the set of likely system modes is highly time variant. Furthermore, the mode space is not known in advance, in comparison with when an industrial robot carries the reflector. The robot must be programmed in advance, and there is some more information available e.g. its repeatability, which can be used to deduce a reasonable and limited number of system models, as shown in Ulrich [2013]. Therefore, variable structures of a hybrid system estimator have to be considered for scenario where a person carries the reflector.

The likely-model set structure belongs to the most important class, the adaptive structure of the variable structure. Its active model set is generated by deleting the unlikely models in the total set to match the true mode at the given time [Rong Li and Zhang, 2000].

The likely-model set (LMS) algorithm uses a subset of the models in the total set which are likely to match the true mode. For implementation the state dependency of the mode set can be utilized. Therefore, the set of possible system modes at the next time is determined by the mode transition law, this is the adjacency relations of the modes, which is a subset of the mode space given the current system mode according to Rong Li [2000].

The two major steps in a LMS algorithm are

- Model classifying, as unlikely, significant and principal
- Model-set adaptation, discard the unlikely ones, keep the significant ones and activate the models adjacent from the principal ones

However, even if the LMS is used, there is still the issue that there must be some knowledge in advance about the process, in order to set up a reasonable subspace of models in which the process might stay. Additionally, the transition probability matrix needs to be defined. In the scenario where a person carries a reflector, reasonable boundaries maybe deduced from the kinematic performance of the measurement system e.g. the maximum acceleration at which the instrument can work, but this needs further investigation.

Chapter 4

Measurement Model

Within the field of LVM there are different kinds of measurement instruments, the two most common ones for carrying out kinematic measurements are laser trackers and photogrammetric systems. In order to integrate one of these instruments into a Bayesian filter technique, an appropriate measurement model must be used.

In Ulrich [2015] a stereo photogrammetric system was used to measure the movement of a rotating arm. Within these experiments, the standard deviation of the 3D point calculation provided an initial guess for the probabilistic model within the Bayesian filter. As this standard deviation includes a large portion of the elements taking part in the 3D point determination within a stereo photogrammetric system e.g. the calibration parameter, the image processing. Furthermore, the shutter-time was considered, with respect to its influence on the resulting geometry and to a common time axis. The use of the 3D point standard deviation as an initial guess can also be applied to multi-camera systems, however more research is required to clearly deduce single kinematic influences of all the internal and external elements on the final 3D point standard deviation.

The kinematic process can also be observed by more than one measurement instrument which may lead to different state space estimates about the process. Therefore, these different estimates needs to be fused together to one state estimate.

4.1 Laser Tracker

As mentioned in chapter 1, the main focus is on laser trackers in order to be integrated into the robot control system. To get the most out of this integration the uncertainty of the trajectory measured by a laser tracker is needed.

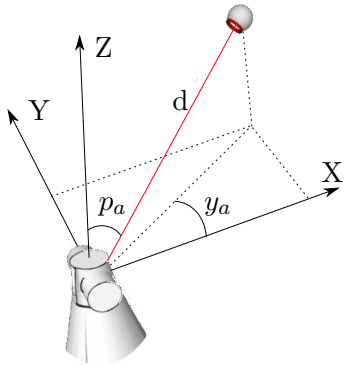

Figure 4.1: A sketch of a laser tracker together with a retro-reflector.

Commercial laser trackers can be subdivided into two design types. These are the gimbal mounted beam source type and the gimbal mounted beam steering mirror, as can be seen in Ulrich [2013]. For calibration purposes, geometric models already exist, for the latter one the model was developed by Loser and Kyle [1998]. For the first one a calibration model was published by Muralikrishnan et al. [2009] which is an adoption of the well-known model of tacheometers and theodolites which can be found e.g. in Deumlich [1982]. A mathematically revised version of this model can be found in Hughes et al. [2011]. These models describe the geometrical beam path within the laser tracker by considering its sub-parts. They consequently also need to be taken into account to determine the uncertainties of kinematic measurements.

Due to the fact that the Leica AT901 laser tracker has a beam steering mirror and all experiments were done with this kind of laser tracker, only the beam steering model is considered in the following. Using this model the entire analysis method can be demonstrated without any loss of generality. Figure 4.1 illustrates a laser tracker together with a retro-reflector. Here, the pitch angle is denoted using p_a, the yaw angle is y_a and d is the distance.

Geometry

There are three groups of geometric parameters. The offset parameters model the deviation of the transit axis not intersecting the primary/standing axis and the parallel deviation between the laser beam and the primary axis. In figure 4.2a the offset parameters are depicted and they are made up of the distance between the mirror and the primary axis named e, the parameter f_p the offset between the mirror and the rotation centre, the beam offset O_1 between the beam and the primary axis and the beam offset O_2 due to the cover plate. The parameter O_1 and O_2 can be further divided into a x and y component.

The second group is the tilt parameters, which are shown in figure 4.2b. The deviation of the perpendicularity of transit axis to the primary axis is described by the transit axis

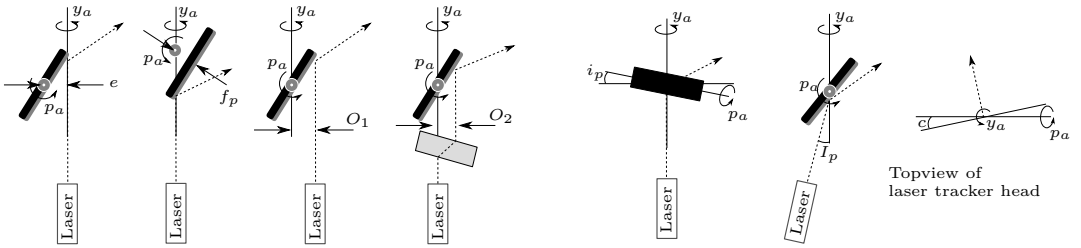

(a) Offset parameters

(b) Tilt parameters

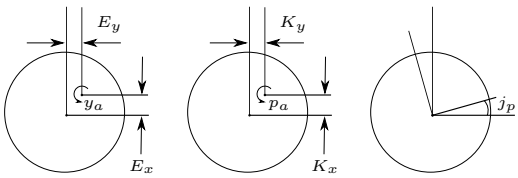

(c) Eccentricity parameters and the pitch index offset.

Figure 4.2: Geometry parameters of a beam steering mirror laser tracker according to Loser and Kyle [1998].

tilt i_p. The parameter beam axis tilt I_p is the parallelism deviation between the primary axis and the beam axis which can be further sub-divided into a x and y component. Furthermore the parameter c, mirror tilt, is the tilt between mirror and the transit axis as they should be parallel.

The last group is the encoder offsets and the pitch index offset, as depicted in figure 4.2c. The eccentricity of the pitch encoder K is the distance between the rotation centre and the encoder centre and E is the eccentricity of the yaw encoder E. The pitch index offset is j_p. The parameter E and K are divided into a x and y components for calculation purposes as can be seen in equation (4.1) and (4.2).

The yaw angle, $y_{a.\mathrm{corr}}$, is determined by using the geometric calibration model of Loser and Kyle [1998] as follows

$$\begin{aligned} y_{a.\mathrm{corr}} = y_{a.m} &+ \frac{\left(O_{1x}\cos\left(y_{a.m}\right) - O_{1y}\sin\left(y_{a.m}\right) + O_{2x} + y_{a.\mathrm{off}}\right)/d_m}{\sin\left(p_{a.m} + j_p\right)} \\ &+ \frac{I_{p.x}\cos\left(y_{a.m}\right) - I_{p.y}\sin\left(y_{a.m}\right)}{\sin\left(p_{a.m} + j_p\right)} - \frac{i_p \sin\left(\frac{p_{a.m}+j_p}{2}\right) + c}{\cos\left(\frac{p_{a.m}+j_p}{2}\right)} \\ &+ E_y \sin\left(y_{a.m}\right) - E_x \cos\left(y_{a.m}\right). \end{aligned} \tag{4.1}$$

The yaw angle value measured is $y_{a.m}$, the pitch angle value measured is $p_{a.m}$ and d_m is the distance corrected with respect to the meteorological conditions. In order to easily distinguish the variables, a is additionally used as a subscript variable to denote an angle

measurement. A correction when the reflector is moving provides the term $y_{a.\text{off}}$. All other terms are explained above.

The corrected pitch angle can be calculated as

$$\begin{aligned} p_{a.\text{corr}} = p_{a.m} + j_p - I_{p.x}\sin\left(y_{a.m}\right) - I_{p.y}\cos\left(y_{a.m}\right) - \frac{O_{1x}\sin\left(y_{a.m}\right) + O_{1y}\cos\left(y_{a.m}\right)}{d_m} \\ + \frac{p_{a.\text{off}} + O_{2y}}{d_m} - \cos\left(\frac{p_{a.m} + j_p}{2}\right)\left(\frac{2}{d_m}\left(e\cos\left(\frac{p_{a.m} + j_p}{2}\right) + f_p\right) + K_x\right) \\ + K_y\sin\left(\frac{p_{a.m} + j_p}{2}\right). \end{aligned} \tag{4.2}$$

Similar to the term $y_{a.\text{off}}$, the term $p_{a.\text{off}}$ provides a correction when the reflector is moving. Again, all other terms are explained above.

In addition, the distance measured is corrected as follows

$$d_{\text{corr}} = d_m - 2\sin\left(\frac{p_{a.m} + j_p}{2}\right)\left(e\cos\left(\frac{p_{a.m} + j_p}{2}\right) + f_p\right) + b \tag{4.3}$$

The home point distance is denoted using b which represents the datum reference for the interferometer. The other parameters are described above.

When applying the calibration procedure on the Leica laser tracker AT901, available at the institute, the standard deviations of the calibration parameter, as explained above, can be determined. The maximal standard deviation for each group can be seen in table 4.1. Here, the vertical index shift is subsumed into the tilt parameters due to its unit,

	Max. std value
Offset parameters	$\approx 1.4\,\mu\text{m}$
Tilt parameters	$\approx 2.2\,\mu\text{rad}$
Eccentricity parameters	$\approx 3.0\,\mu\text{m}$

Table 4.1: Maximal standard deviation of the calibration parameters after the calibration process.

despite the above proposal. Further parameters concerning the laser tracker can be found in [Leica Geosystems AG, 2009b,c], as mentioned in chapter 1.

Meteorology

As mentioned in the chapter introduction, a laser tracker may have implemented an ADM and an IFM as a length measurement device. When using a Leica laser tracker AT901, for kinematic measurements only the implemented IFM can be used, because of this, only the meteorological correction for IFM measurements are considered which means only the standard index of refraction, the phase index, is taken into account.

A distance measured by an interferometer needs to be corrected with respect to the refractive index of air considering the given wavelength as well as the air temperature, the pressure and the humidity. Due to the fact, that the basic length scale is the wavelength in air, the distance can be corrected by

$$d_m = d_0 \frac{10^6}{10^6 + n\left(T_m, p_m, H_m, \lambda_m\right)}. \tag{4.4}$$

Here the distance measured by the interferometer is d_0 without considering a refraction compensation and d_m is the distance with refraction compensation. The refractive index with respect to the temperature T_m, the pressure p_m, the humidity H_m and the wavelength λ_m is $n\left(T_m, p_m, H_m, \lambda_m\right)$. In general the refractive index of air can be calculated using either the equation developed by Ciddor or the updated version of the Edlén equation. Even if the Ciddor equation delivers somewhat better results, under rough conditions in terms of temperature, pressure and humidity, than the Edlén equation, the latter is commonly used for precision measurements at temperature near 20 °C [Stone and Zimmerman, 2011]. Due to the rough environmental condition issue the International Association of Geodesy (IAG) adopted the Ciddor equation as the standard equation for calculating the refraction index [Stone and Zimmerman, 2011].

The refractive index considering the interferometer of a laser tracker can be calculated using the Edlén approach as

$$n = n_{\mathrm{tp}} - 10^{-10}\left(3.7345 - 0.0401\lambda_m^{-2}\right) p_v. \tag{4.5}$$

Here the wavelength λ_m is in µm, the water vapour partial pressure is p_v and when using relative humidity H_r, p_v can be calculated as $p_v = H_r/100 p_{sv}$. For the calculations presented here it is assumed that the temperature, T, is in °C and that the pressure values, p, are given in Pa, this is important as the coefficients are dependent on that. Furthermore, the saturation vapour pressure p_{sv} can be calculated using the equations described in Huang [1998]. Using the revised Edlén equation the dry air refractive index n_{tp} can be determined as

$$n_{\mathrm{tp}} = 1 + \frac{p\left(n_s - 1\right)}{96095.43} \frac{1 + 10^{-8}\left(0.601 - 0.00972\,T\right) p}{1 + 0.003661\,T} \tag{4.6}$$

according to Birch and Downs [1994]. Using the deduction in Birch and Downs [1994] the revised dispersion equation leads to

$$n_s = 1 + 10^{-8}\left(8342.54 + \frac{2406147}{130 - \lambda_m^{-2}} + \frac{15998}{38.9 - \lambda_m^{-2}}\right). \tag{4.7}$$

Finally the corrected distance can be calculated, as proposed in equation (4.4).

So far, only the change in wavelength due to the refractive index is considered to correct the distance measurement. Using only this approach to treat all meteorological issues can be considered as insufficient. As this would assume that the refractive index is homogeneous in the whole working volume along the laser beam which cannot be guaranteed and

specially for typical laser tracker working volumes it is not realistic. In Eschelbach [2007] an approach was proposed to correct the angle measurements as well as the distance measurement using 3D temperature gradient. Thereby, solely the temperature gradient was used as it was assumed that pressure inhomogeneity and humidity inhomogeneity along the laser beam do not occur when making indoor measurements. Unfortunately, this approach requires well disturbed temperature sensors along the laser beam which is not feasible.

In order to refine the probabilistic model, the turbulence theory could be used and particularly the angle part could take advantage of it. The variance of the angle for a plane wave propagating through weak turbulence has to be calculated with respect to the aperture diameter b_m of the receiving telescope and with respect to the inner and outer boundaries l_0 and L_0 of the inertial sub-range. They describe the atmospheric inhomogeneities (eddies), the smallest eddies l_0 are between 1 mm to 3 mm [Brunner, 1984].

As proposed by Brunner [1984] the variance of the angle can be calculated with respect to the inner boundary as follows

$$\sigma_\alpha^2 \cong 1.46\, b_m^{-1/3}\, S_m\, \overline{C}_n^2 \qquad l_0 \ll b \ll R_m \tag{4.8}$$

and with respect to the outer boundary

$$\sigma_\alpha^2 \cong 2.92\, b_m^{-1/3}\, S_m\, \overline{C}_n^2 \qquad L_0 > b \gg R_m \tag{4.9}$$

Here, R_m is the radius of the first Fresnel zone which is given by

$$R_m = (\lambda_m\, S_m)^{1/2}\,. \tag{4.10}$$

Where, S_m is the path length and λ_m is the wavelength. Furthermore, the average value of the strength of the atmospheric turbulence is denoted using $\overline{C}_n^2$ which can be calculated as

$$\overline{C}_n^2 = \frac{1}{S} \int_0^S C_n^2\,(x)\; dx. \tag{4.11}$$

Here, the refractive index structure parameter C_n^2 is a measure of the magnitude of the fluctuation of the refractive index and can be related to the 3D refractive index spectrum.

Furthermore, the variance of the distance can be calculated as proposed by Hennes [1995] and Brunner [1984] using the following equation

$$\sigma_L^2 = a_m\, S_m\, \overline{C}_n^2\, L_0^{5/3}. \tag{4.12}$$

Here, a_m depends on the spectral model selected and can vary between 3 to 30 [Brunner, 1984]. The equations (4.8) to (4.12) are used for individual observation; however, Brunner [1984] derived several augmentations for multiple observations. Nevertheless,

for kinematic measurements these equations can be directly applied, as there is only a single measurement for a point available.

However, to apply the equation (4.8) to (4.12) the measurement of $\overline{C}_n^2$ along the laser beam is needed. In principle, $\overline{C}_n^2$ can be determined by the measurements of a scintillometer. However, these measurements take some time, so it is not suitable for kinematic measurements and more important it made up of rather big sender and receiver devices which cannot be attached next to a laser tracker retro-reflector.

To sum up, to date there is no feasible method to precisely correct the laser tracker measurements due to environmental influences, during kinematic measurements in conjunctions with an industrial robot. In subsection "Integration Within Bayesian Filter" there is a method proposed to get a rough estimate of the variance of the angle and distance measurement influenced by the environmental conditions.

Reflector

Three different kinds of retro-reflectors can be used in conjunction with a Leica laser tracker, spatial mounted reflectors carrying a glass prism, cat's eye reflectors and air path corner cube reflectors.

According to Markendorf [2000] there is a systematic deviation with respect to the laser beam's angle of incidence when using the spatial mounted reflector carrying a glass prism. A similar effect has been reported by Pauli [1969] when using glass in a reflector, which can be calculated by using Snell's law along the beam path. In consequence this kind of reflector is unsuitable when a small uncertainty is needed due to the fact that the angle of incidence cannot be controlled throughout kinematic measurements.

A cat's eye reflector is made up of different glass hemispheres of differing refractive indices and sizes. All incident beams should be reflected back, parallel to the incident beams. However, throughout kinematic measurements the laser tracker's beam is not at all time perpendicular to the outer glass hemisphere which leads to an imperfect back reflection. Owing to the spherical glass surface incident beams being non-perpendicular are back reflected non-parallel to the incident beam. In figure 4.3 this additional angle of reflection is ι. The cat's eye model was developed as published in Loser [2001] and Zuercher et al. [1995]. With respect to the height h_r of the beam according to the figure 4.3 the divergence angle ι of-non-perpendicular beams can be derived to be

$$\begin{aligned}\iota = 2\Bigg(&-\arcsin\left(\frac{h_r}{r_{r.1}}\right) - \arcsin\left(\frac{h_r}{r_{r.2}}\frac{n_1}{n_2}\right) + \arcsin\left(\frac{h_r}{r_{r.1}}\frac{n_1}{n_2}\right)\\ &+ \arcsin\left(\frac{h_r}{r_{r.2}}\frac{n_1}{n_3}\right) + \arcsin\left(\frac{h_r}{r_{r.3}}\frac{n_1}{n_3}\right)\Bigg),\end{aligned} \tag{4.13}$$

which is similar to a n2 reflector as developed in Yongbing et al. [2003]. The radiuses of the different glass spheres used in the cat's-eye $r_{r.1}$ to $r_{r.3}$ can be seen in figure 4.3, n_2 to n_5 are the different refraction indexes of these spheres. Figure 4.3 implies, that

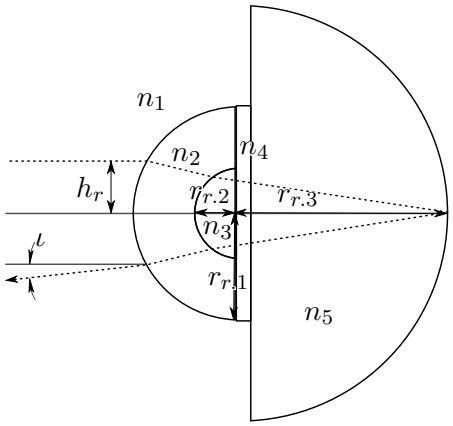

Figure 4.3: Cat's eye reflector

a perpendicular beam has the height $h_r = 0$ and is reflected without deviation. Due to the fact that there is not enough time for the control algorithm of the laser tracker to be regulated to the PSD control point, the PSD values are used in the terms $y_{a.\text{off}}$ and $p_{a.\text{off}}$ to correct the angle measurements throughout kinematic measurements. This is why the additional divergence angle directly effects the $y_{a.\text{off}}$ and $p_{a.\text{off}}$ term and in consequence the yaw and pitch angle. Accordingly, an unpredictable uncertainty source remains when using a cat's eye reflector throughout kinematic movements.

On the other hand, air path corner cube reflectors may also introduce additional uncertainties. This is due to their dihedral angle error of the mirror planes if the reflector's roll angle cannot be held steadily throughout the kinematic measurement. Only the yaw and pitch angle are effected due to an additional deviation on the PSD. According to ASME B89.4.19 [2006] the maximum allowable dihedral angle error is set according to the accuracy of the PSD control point and the stringency of the laser tracker specifications.

In summary, when using air path retro-reflectors specified by the laser tracker manufacturer and holding the reflector's roll angle, fixed additional effects caused by reflectors can be largely mitigated.

Integration within a Bayesian Filter

For the integration within a Bayesian filter additionally the synchronization between the measurement and the control data has also to be considered. Within the Leica laser tracker the internal control loop runs at a frequency of 3000 Hz. The PSD outputs, the angle encoder and the distance readings are stored together with an associated time stamp. The measurements are interpolated to match the timing of the external trigger impulse, so that the trigger impulse does not interrupt the measurement process according to Kihlman et al. [2004] and Leica Geosystems AG [2009a]. Loser [2001] described the synchronization of this trigger impulse as the main source of uncertainty in

kinematic laser tracker measurements. This is due to the fact that the PSD control point is determined during the initialization procedure of the laser tracker [Loser, 2004]. As the PSD control point effects the terms $y_{a.\text{off}}$ and $p_{a.\text{off}}$ which are used during kinematic measurements to improve the angle measurements, as can be seen in equation (4.1) and (4.2). Therefore, an error in the PSD control point would lead to big systematic deviations, as also described in ASME B89.4.19 [2006]. As a result, a 3D point of an object's movement can be expressed in the first approximation as follows

$$\begin{aligned} x &= d_{\text{corr}} \cdot \cos\left(y_{a.\text{corr}}\right) \cdot \sin\left(p_{a.\text{corr}}\right) + V_x \cdot t_s + \dots \\ y &= d_{\text{corr}} \cdot \sin\left(y_{a.\text{corr}}\right) \cdot \sin\left(p_{a.\text{corr}}\right) + V_y \cdot t_s + \dots \\ z &= d_{\text{corr}} \cdot \cos\left(p_{a.\text{corr}}\right) + V_z \cdot t_s + \dots \quad . \end{aligned} \tag{4.14}$$

Here V_x, V_y, V_z are the components of the velocity according to the corresponding coordinate axis and the synchronization error is t_s.

As mentioned above, when using a Bayesian filter, a deterministic and a probabilistic model of the measurement model is needed. In order to deduce a probabilistic measurement model, the Monte-Carlo Method in conjunction with equation (4.14) can be used to determine a probability density for any arbitrary point as proposed in Ulrich [2013]. Taking equation (4.14) into consideration, it becomes clear that the measurement model is highly dependent on the object's state, meaning the position and the current kinematic behaviour. Consequently, the measurement model needs to be recalculate every Bayesian filter cycle to take into account the object's new state.

Due to the fact that there are several influences on the angle measurement which cannot be further quantified, the standard deviation of the angle encoder readings has to be adjusted. This is because normal users cannot get the PSD values during kinematic measurements, which effects the terms $y_{a.\text{off}}$ and $p_{a.\text{off}}$ as can be seen in equation (4.1) and (4.2). Furthermore, the meteorological correction does not include the angle measurements, as explained above, and the error due to the dihedral angle error of the reflector is unknown. As proposed in Leica Geosystems AG [2009b] a good estimate of the meteorological part can be deduced, by observing a stable point for a certain period of time within the measurement volume. Applying this method an overall approximation for the standard deviation of the angle measurement can be estimated to be $\approx 4\,\mu\text{rad}$, when using the Leica AT901 indoors having weak turbulence.

4.2 Multi Sensor Data Fusion

The uncertainty of a state space vector estimate can be decreased by including further information about the state into the analysis. This information can also be the same kind of information, simply measured using another sensor e.g. two laser trackers measure the same reflector attached to the tool centre point of an industrial robot. For this kind of multiple sensor data fusion either the fusion can be accomplished within a centralized architecture, or within a decentralized architecture as described in Mitchell [2007]. If

all raw measurements are sent to a single fusion node before they are processed then this architecture is called centralized architecture, also known as measurement fusion. The drawback with this type of architecture is that it is very sensitive to spatial and temporal misalignments. On the other hand this architecture has a higher performance than the decentralized architecture also called track-to-track fusion [Mitchell, 2007; Chen et al., 2003; Zhansheng and Rong Li, 2008]. Before transmitting the measurements to a fusion node in order to join all sensor data together, every sensor node preforms its own Bayesian filtering within a decentralized architecture.

Where the measurements of two LVM instruments, e.g. two laser trackers, should be fused together one can expect that the measurements can be precisely synchronized and that the transformation parameters between the instruments can be determined within a reasonable uncertainty. Therefore, only the measurement fusion architecture type is considered in the following.

In order to use the measurement fusion architecture, the update equation of the Bayesian filter needs to be adjusted as shown in Ulrich [2013], e.g. equation (3.15) becomes:

$$\left[\hat{\boldsymbol{x}}^{i}_{t+1}, \boldsymbol{P}^{i}_{t+1}\right] = \mathrm{KF}_u\left(\hat{\boldsymbol{x}}^{-,i}_{t+1}, \boldsymbol{P}^{-,i}_{t+1}, \boldsymbol{z}_{t+1}, \tilde{\boldsymbol{H}}^{i}_{t+1}, \tilde{\boldsymbol{R}}^{i}_{t+1}\right) \tag{4.15}$$

with

$$\tilde{\boldsymbol{z}}_t = \begin{pmatrix} \boldsymbol{z}^1_t \\ \vdots \\ \boldsymbol{z}^{l_f}_t \end{pmatrix} \quad \tilde{\boldsymbol{H}}^{i}_t = \begin{pmatrix} \boldsymbol{H}^{i,1}_t \\ \vdots \\ \boldsymbol{H}^{i,l_f}_t \end{pmatrix} \quad \tilde{\boldsymbol{R}}^{i}_t = \mathrm{diag}\left[\boldsymbol{R}^{i,1}_t, \cdots, \boldsymbol{R}^{i,l_f}_t\right],$$

Here l_f is the number of involved measurement instruments that should be fused together. A feature of this method, is that it can incorporate measurements from distinct measurement instruments e.g. different laser trackers but also photogrammetric systems or additional sensors attached on the robot's TCP like pressure sensors, etc.

Chapter 5

Kinematic Ground Truth

As the analysis method for kinematic measurements presented so far incorporates a measurement model, it is essential to verify the derived model of a Leica laser tracker taking into account a ground truth.

To test the laser tracker's kinematic properties Peipe [1996]; Loser [2001]; Morse and Welty [2013] proposed observing points on a rotating arm, followed by a best-fit circle to the points. When taking into account figure 2.1, it becomes clear that this procedure focuses solely on the internal synchronization of the subsystems of a laser tracker i.e. the angle encoders and the distance measurement, because only measurements within the measurement space are considered. This is why the procedure cannot be used to generate a ground truth for kinematic laser tracker measurements as proposed in section 2.2.

The most straightforward way of verifying the measurement model would be, if the retro-reflector could be simultaneously measured using an additional instrument with a higher level of accuracy. In principle, this could be achieved by using a multilateration system, consisting of four laser tracers, as explained in more detail in the following section.

However, due to various dynamic restrictions, the laser tracker cannot be tested over its whole range of kinematic performance capabilities, when using a multilateration system. For this reason, another kinematic ground truth was developed to test the laser tracker over a wider kinematic spectrum. The resulting ground truth is made up of a linear rail and a glass scale with a very high level of accuracy. When using a linear rail, no arbitrary trajectories can be chosen in contrast when using the multilateration system, however different motion profiles can be applied. Due to the linear rail solely kinematic issues are taken to account. To focus solely on geometric issues any standard calibration procedure can be applied. This ground truth is explained in more detail in section 5.2.

5.1 Laser Tracer / Multilateration

A laser tracer is an interferometer which measures the distance to a retro-reflector and also tracks this retro-reflector while it is moving in space. It is equipped with a mechanically and thermally decoupled reference reflector for its interferometer, in order to achieve a high level of accuracy. This results in a sub-micron stability while the tracking mechanism is in movement [National Physical Laboratory (NPL), 2009]. Due to the fact, that a laser tracer delivers only the change in distance to a moving retro-reflector, four synchronized laser tracers are used to determine the reflector's 3D position using a technique called multilateration. As a result, a multilateration system, made up of four synchronized laser tracers would be ideally suited to deliver a ground truth for kinematic laser tracker measurements. The reason for distance-only measurement is to eliminate the less accurate angle measurements whose uncertainty has a linearly increasing spatial error as the distance to target increases.

The absolute distances between each laser tracer and the reflector must be established at the beginning of a kinematic experiment as the laser tracers only provide relative changes in the distances. The starting distance between a laser tracer and the reflector is measured using a tape measure to get a rough estimate of the absolute distance. Accordingly, the absolute starting distances must be refined within the analysis method. The analysis method determines the laser tracer 3D positions, the refined offsets of the start distances, also known as dead paths, and the 3D positions of the reflector. As there are no additional scale deviations considered in this analysis approach, the wave length of each laser tracer should be established and calibrated. Furthermore, the meteorology does not need to be factored in because laser tracer distance measurements are directly adjusted with respect to the meteorological condition within the working volume.

Standard Analysis Method

The multilateration analysis can be seen as a free-network adjustment in the Gauss-Markov-model using distance measurements alone. Within the Gauss-Markov adjustment model the unknowns are estimated with maximum probability. This model is also known as a least-squares adjustment or a minimisation using the L2 norm [Luhmann et al., 2013], and the condition for the residuals is:

$$\boldsymbol{v}^{\mathsf{T}}\boldsymbol{P}_G\boldsymbol{v} \rightarrow \min! \tag{5.1}$$

Here, $\boldsymbol{v}$ is the residual vector and $\boldsymbol{P}_G$ is the weight matrix. The functional model of the multilateration analysis can be expressed as

$$d_{i,j} = \sqrt{(X_i - \mathcal{X}_j)^2 + (Y_i - \mathcal{Y}_j)^2 + (Z_i - \mathcal{Z}_j)^2} - o_j. \tag{5.2}$$

Here the 3D position i of the reflector is given by X_i, Y_i, Z_i with $i \in \{1, 2, \ldots, u\}$ and the 3D position of laser tracer j is denoted using $\mathcal{X}_j, \mathcal{Y}_j, \mathcal{Z}_j$ with $j \in \{1, 2, \ldots, n\}$. The

	Tracer 1				Tracer 2				Tracer …				Tracer n				Pos. 1			Pos. 2			Pos. …			Pos. u		
	X	Y	Z	o	X	Y	Z	o	X	Y	Z	o	X	Y	Z	o	X	Y	Z	X	Y	Z	X	Y	Z	X	Y	Z
$d_{1,1}$	■																■											
$d_{1,2}$					■												■											
$d_{1,\dots}$									■								■											
$d_{1,n}$													■				■											
$d_{2,1}$	■																			■								
$d_{2,2}$					■															■								
$d_{2,\dots}$									■											■								
$d_{2,n}$													■							■								
$d_{\dots,1}$	■																						■					
$d_{\dots,2}$					■																		■					
$d_{\dots,\dots}$									■														■					
$d_{\dots,n}$													■										■					
$d_{u,1}$	■																									■		
$d_{u,2}$					■																					■		
$d_{u,\dots}$									■																	■		
$d_{u,n}$													■													■		

Table 5.1: Design matrix structure, the not null elements are depicted with a grey cell.

distance measured between reflector position i and laser tracer j is $d_{i,j}$ and the dead path offset of laser tracer j is o_j. As the functional model in (5.2) is non-linear, the adjustment in the Gauss-Markov-model needs to be iteratively solved, this includes a linearisation of (5.2). This requires the partial derivatives with respect to the unknowns for the design matrix $\boldsymbol{A}_G$ are:

$$\begin{aligned}
\frac{\partial d_{i,j}}{\partial X_i} &= \frac{-\left(\mathcal{X}_j - X_i\right)}{d^R_{i,j}} & \frac{\partial d_{i,j}}{\partial Y_i} &= \frac{-\left(\mathcal{Y}_j - Y_i\right)}{d^R_{i,j}} \\
\frac{\partial d_{i,j}}{\partial Z_i} &= \frac{-\left(\mathcal{Z}_j - Z_i\right)}{d^R_{i,j}} & \frac{\partial d_{i,j}}{\partial \mathcal{X}_j} &= \frac{\left(\mathcal{X}_j - X_i\right)}{d^R_{i,j}} \\
\frac{\partial d_{i,j}}{\partial \mathcal{Y}_j} &= \frac{\left(\mathcal{Y}_j - Y_i\right)}{d^R_{i,j}} & \frac{\partial d_{i,j}}{\partial \mathcal{Z}_j} &= \frac{\left(\mathcal{Z}_j - Z_i\right)}{d^R_{i,j}} \\
\frac{\partial d_{i,j}}{\partial o_j} &= -1
\end{aligned} \tag{5.3}$$

with

$$d^R_{i,j} = \sqrt{\left(X_i - \mathcal{X}_j\right)^2 + \left(Y_i - \mathcal{Y}_j\right)^2 + \left(Z_i - \mathcal{Z}_j\right)^2}$$

The final matrix $\boldsymbol{A}_G$ has a sparse matrix structure which can be seen in table 5.1, where the non-zero elements are depicted by a grey cell. The stochastic model of the distance observations can be derived as being

$$q = u^2_{l.a} + \left(u_{l.b} \cdot d^R_{i,j}\right)^2. \tag{5.4}$$

Here, q is a diagonal element of the covariance matrix $\boldsymbol{Q}_G$. The distance measurement's constant uncertainty element is $u_{l.a}$ and $u_{l.b}$ takes account of the range-dependent element of uncertainty. The covariance matrix is reduced to a diagonal matrix as the measurements of the laser tracer can be considered to be stochastically independent and all correlation coefficients become zero. Determining the unknowns using the Gauss-Markov adjustment model requires the calculation of the inverse matrix of the matrix of normal equations

$$\boldsymbol{N} = \boldsymbol{A}_G^{\intercal} \cdot \boldsymbol{P}_G \cdot \boldsymbol{A}_G. \tag{5.5}$$

Here, $\boldsymbol{P}_G$ is the weight matrix which is the inverse of the covariance matrix. However, calculating the inverse of the matrix of normal equations $\boldsymbol{N}$ is not possible, as the matrix is singular. This is because of the rank defect of the design matrix $\boldsymbol{A}_G$, which means only the shape of the network can be determined, as its position and orientation within a coordinate system have not yet been defined. As already stated in Illner [1985] the rank defect of a 3D free-network adjustment is six, when the scale factor is considered to be fixed.

When introducing approximate coordinates of the reflector positions as datum points into the free-network adjustment, the rank defect is eliminated. In consequence, the free-network adjustment attempts to fit the multilateration coordinates to the approximate coordinates. Accordingly, the approximate coordinates must be sufficiently good to ensure that the iterative process can converge. The fitting to the approximate coordinates defines the requirements, meaning that the translation and the rotation between the approximate coordinates and the coordinates of the multilateration system should be minimal, which yields in the matrix

$$\boldsymbol{B} = \underbrace{\begin{bmatrix} \mathbf{0} \cdots \end{bmatrix}}_{\text{Laser tracer}} \underbrace{\begin{bmatrix} 1 & 0 & 0 & \cdots & 1 & 0 & 0 \\ 0 & 1 & 0 & \cdots & 0 & 1 & 0 \\ 0 & 0 & 1 & \cdots & 0 & 0 & 1 \\ 0 & -\tilde{Z}_i & \tilde{Y}_i & \cdots & 0 & -\tilde{Z}_u & \tilde{Y}_u \\ \tilde{Z}_i & 0 & -\tilde{X}_i & \cdots & \tilde{Z}_u & 0 & -\tilde{X}_u \\ -\tilde{Y}_i & \tilde{X}_i & 0 & \cdots & \tilde{Y}_u & \tilde{X}_u & 0 \end{bmatrix}}_{\text{Multilateration points}} \tag{5.6}$$

according to Illner [1985] and Luhmann et al. [2013]. The matrix $\boldsymbol{B}$ has the dimensions $6 \times (4 \cdot n + 3 \cdot u)$ and $\left(\tilde{X}_i, \tilde{Y}_i, \tilde{Z}_i\right)$ denotes the approximate coordinate of the reflector position i. The translation requirements can be found in the first three rows and the rotation requirements can be seen in the last three rows. The system of normal equations is extended by the requirement matrix $\boldsymbol{B}$ which results in

$$\begin{aligned} \begin{bmatrix} \hat{\boldsymbol{x}}_G \\ \boldsymbol{k} \end{bmatrix} &= \begin{bmatrix} \boldsymbol{A}_G^{\intercal} \boldsymbol{P}_G \boldsymbol{A}_G & \boldsymbol{B}^{\intercal} \\ \boldsymbol{B} & \mathbf{0} \end{bmatrix}^{-1} \cdot \begin{bmatrix} \boldsymbol{A}_G^{\intercal} \boldsymbol{P}_G \boldsymbol{l} \\ \mathbf{0} \end{bmatrix} \\ &= \overline{\boldsymbol{N}}^{-1} \cdot \overline{\boldsymbol{n}}. \end{aligned} \tag{5.7}$$

The vector of reduced observations is $\boldsymbol{l}$ and $\hat{\boldsymbol{x}}_G$ is the vector of unknowns containing the estimated parameters. Furthermore, the vector $\boldsymbol{k}$ contains the Lagrange multipliers. The vector of reduced observations is the observed observations minus the computed observations, which are obtained by using the functional model of equation 5.2 together with the available approximated values of the unknowns.

Refined Analysis Method

According to Niemeier [2008], there are different quantities which provide a quality criteria for geodetic networks, i.e. the overall quality, the global accuracy and the homogeneity and isotropy which are well known in this field. However, the geometrical stiffness of a network was proposed by Schmitt [1997] as an additional criterion. This criterion was introduced to reduce weak forms within the network by strengthening the geometry in general, in order to increase the significance in separating out deformations in monitoring networks. Therefore, the consideration of this criterion is, most notably, to make a reliable assessment of any deformation or difference between the multilateration system and the laser tracker being tested.

As shown in Schmitt [1997], the tendency of a geodetic network to leave its geometry by oscillating around its stable form can be seen in the solution of the special eigenvalue problem

$$(\boldsymbol{N} - \lambda_i \boldsymbol{I})\, \boldsymbol{m}_{v.i} = 0 \tag{5.8}$$

with respect to the normal equation matrix. Here, the i^{th} eigenvector is $\boldsymbol{m}_{v.i}$ and the i^{th} eigenvalue λ_i. This solution can be utilised to illustrate the weak forms of the network by vector-plots using $\boldsymbol{m}_{v.i}\sqrt{\lambda_i}$ as the components in the coordinates. According to Schmitt [1997] the dominant weak form is defined by

$$\boldsymbol{m}_{v.1}\sqrt{\lambda_1} \quad \text{with} \quad \lambda_1 = \max(\lambda_i)\,\forall\, i. \tag{5.9}$$

Consequently, the dominant weak form is governed by the value of the maximal eigenvalue which can be easily found in the eigenvalue spectrum.

The maximal eigenvalue can be reduced by introducing additional restrictions into the adjustment method, by changing the network configuration or by altering the initial covariance matrix, meaning measuring certain network parts with another instrument, as Kaltenbach [1992] showed.

Due to space restrictions of an experiment set-up and the angle of acceptance changing the configuration of the laser tracers is not always possible. In addition, when using a multilateration system, measuring parts of the network with another instrument is not feasible. However, introducing additional geometrical restrictions into the analysis process should be appropriate for most experiment set-ups where the other suggestions cannot be applied.

Further geometrical restrictions can be derived from the affine transformation. This means that, beside the translation and rotation restriction, which have already been

used, there are the scale parameters and the shear factors of the coordinate system axis. A common affine transformation can be expressed as

$$\boldsymbol{x}'_P = \boldsymbol{F}_T \cdot \boldsymbol{x}_P + \boldsymbol{T}, \tag{5.10}$$

according to Welsch et al. [2000]. Here, $\boldsymbol{T}$ is the translation of the point $\boldsymbol{x}_P$ and $\boldsymbol{F}_T$ is the deformation gradient tensor. According to Altenbach [2012], this deformation gradient tensor can be decomposed assuming an infinitesimal deformation into

$$\boldsymbol{F} = \boldsymbol{I}_T + \boldsymbol{H}_T. \tag{5.11}$$

Here $\boldsymbol{I}_T$ is the identity tensor and $\boldsymbol{H}_T$ is the displacement gradient tensor. After a linearisation of the displacement gradient tensor, it can be further decomposed into a symmetric part $\boldsymbol{G}_T$ and an antisymmetric part $\boldsymbol{R}_T$

$$\boldsymbol{H} = \boldsymbol{G}_T + \boldsymbol{R}_T. \tag{5.12}$$

The antisymmetric part $\boldsymbol{R}_T$, represents a linearised rotation tensor for small angles and the symmetric part is a linearised strain tensor. As Altenbach [2012] and Balke [2014] showed, the matrix form of (5.12) can be found by

$$\begin{aligned}
\boldsymbol{H} &= \underbrace{\begin{bmatrix} \varepsilon_{xx} & \varepsilon_{xy} & \varepsilon_{xz} \\ \varepsilon_{xy} & \varepsilon_{yy} & \varepsilon_{yz} \\ \varepsilon_{xz} & \varepsilon_{yz} & \varepsilon_{zz} \end{bmatrix}}_{=\boldsymbol{G}_T} + \underbrace{\begin{bmatrix} 0 & -\omega_{xy} & \omega_{xz} \\ \omega_{xy} & 0 & -\omega_{yz} \\ -\omega_{xz} & \omega_{yz} & 0 \end{bmatrix}}_{=\boldsymbol{R}_T} \\
&= \underbrace{\begin{bmatrix} \varepsilon_{xx} & 0 & 0 \\ 0 & \varepsilon_{yy} & 0 \\ 0 & 0 & \varepsilon_{zz} \end{bmatrix}}_{\text{Scale factors}} + \underbrace{\begin{bmatrix} 0 & \varepsilon_{xy} & \varepsilon_{xz} \\ \varepsilon_{xy} & 0 & \varepsilon_{yz} \\ \varepsilon_{xz} & \varepsilon_{yz} & 0 \end{bmatrix}}_{\text{Shear factors}} \\
&\quad + \underbrace{\begin{bmatrix} 0 & -\omega_{xy} & \omega_{xz} \\ \omega_{xy} & 0 & -\omega_{yz} \\ -\omega_{xz} & \omega_{yz} & 0 \end{bmatrix}}_{\text{Rotation}}.
\end{aligned} \tag{5.13}$$

A new requirement matrix $\boldsymbol{B'}$ can be expressed by using (5.10) and (5.13) together as

$$\boldsymbol{B'} = \begin{bmatrix} \underbrace{\mathbf{0}\cdots}_{\text{Laser tracer}} & \underbrace{\begin{matrix} 1 & 0 & 0 & \cdots & 1 & 0 & 0 \\ 0 & 1 & 0 & \cdots & 0 & 1 & 0 \\ 0 & 0 & 1 & \cdots & 0 & 0 & 1 \\ 0 & -\tilde{Z}_i & \tilde{Y}_i & \cdots & 0 & -\tilde{Z}_u & \tilde{Y}_u \\ \tilde{Z}_i & 0 & -\tilde{X}_i & \cdots & \tilde{Z}_u & 0 & -\tilde{X}_u \\ -\tilde{Y}_i & \tilde{X}_i & 0 & \cdots & \tilde{Y}_u & \tilde{X}_u & 0 \\ 0 & \tilde{Z}_i & \tilde{Y}_i & \cdots & 0 & \tilde{Z}_u & \tilde{Y}_u \\ \tilde{Z}_i & 0 & \tilde{X}_i & \cdots & \tilde{Z}_u & 0 & \tilde{X}_u \\ \tilde{Y}_i & \tilde{X}_i & 0 & \cdots & \tilde{Y}_u & \tilde{X}_u & 0 \\ \tilde{X}_i & 0 & 0 & \cdots & \tilde{X}_u & 0 & 0 \\ 0 & \tilde{Y}_i & 0 & \cdots & 0 & \tilde{Y}_u & 0 \\ 0 & 0 & \tilde{Z}_i & \cdots & 0 & 0 & \tilde{Z}_u \end{matrix}}_{\text{Multilateration points}} \end{bmatrix} \tag{5.14}$$

The matrix $\boldsymbol{B'}$ is $12 \times (4 \cdot n + 3 \cdot u)$ and $\left(\tilde{X}_i, \tilde{Y}_i, \tilde{Z}_i\right)$ denotes the approximate coordinate of the reflector position i. The first six rows are equivalent to matrix $\boldsymbol{B}$ in (5.6). The following three rows represent the three shear factors and the last three rows represent the three scale factors. This matrix is used to replace the matrix $\boldsymbol{B}$ within the extended matrix of normal equations in (5.7), in order to determine the unknown parameters with respect to modified restrictions.

In both cases, the standard analysis method and the refined method, the free-network adjustment is a fitting to the approximate coordinates, which are the laser tracker coordinates, so it is important to make sure that the laser tracker coordinate system contains no errors in a calibration parameter corresponding to one of the transformation parameters.

5.2 Glass Scale / Linear Rail

In the preceding section, the multilateration system was introduced as a possible kinematic ground truth for laser trackers. However, a potential drawback is, that it cannot bring to light all errors as some transformation parameters may correspond to alignment parameters of the laser tracker itself. Therefore, the laser tracker has to be calibrated in advance, using one of the calibration procedures described in Loser and Kyle [1998] or Hughes et al. [2011]. Furthermore, due to the limitation of the laser tracer, the laser tracker cannot be tested over its whole range of kinematic performance capabilities. Because of this, another kind of kinematic ground truth is needed in order to conclusively verify the derived measurement model of a laser tracker.

An alternative kinematic ground truth was set-up consisting of a linear rail and a glass scale. Figure 5.1 shows a sketch of the new ground truth set-up. The principal idea is,

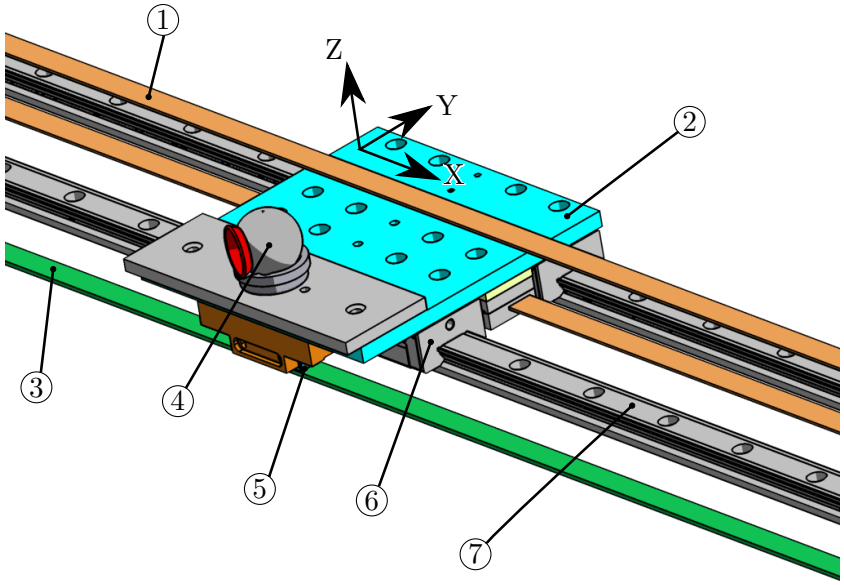

Figure 5.1: Sketch of the kinematic ground truth.

to compare the distance between two retro-reflector ④ positions measured by a laser tracker, against the readings at the glass scale ③. A retro-reflector of a laser tracker is attached to the top of the carriage ⑥, which is mounted on the linear rail ⑦ and also carries the reading head ⑤ of the glass scale. A servo motor moves this carriage along the rail, in conjunction with a programmable servo drive, so that a wide range of motion profiles can be controlled. To perform these movements the carriage is connected via a timing belt ① with the motor. The length of the linear rail is 3 m and the maximum speed of the glass scale reading head is 8 m/s. However, due to some safety reasons the maximum working length is roughly 2.5 m, as some space must be reserved to allow an safe stop triggered by a stop switch.

There are four essential sub-parts which must be borne in mind in order to achieve a high accuracy using this ground truth. The straightness of the linear rail, the accuracy of the glass scale, the eigenfrequency, which might occur during the movement, as well as the synchronization between the glass scale reading and the trigger impulse for the laser tracker.

Linear rail

The linear rail of THK provides a rigidity during motion, within a range lower than 0.5 µm [THK, 2015b] and its specified running parallelism is in the range of ±2.5 µm/m [THK, 2015a]. To achieve a higher rigidity, two parallel rails with two carriages mounted on each rail were used connected with an additional rigid plate of metal ② where the

sensors are attached on. By using this design the effects of the mounting surface errors can also be mitigated [THK, 2015a]. However, after the installation of the rails onto the mounting surface, the accuracy of the straightness needs to be checked.

According to Weck [2013], the straightness of a linear rail can be verified by using an auto-collimator, this technique is also recommended in THK [2015a] for inspection after installation. In this case, the deviation of straightness is measured using an auto-collimator having an accuracy in the range of $\pm 0.1''$. During an auto-collimator measurement the angle differences between cumulative positions along the rail are used to approximate the rail with local tangents. This local tangents are used to determine the deviation of the straightness of the rail as proposed in Weck [2013] using the equations

$$\begin{aligned} dy_i &= \delta l_i \cdot \tan\left(\phi_i - \beta_y\right) \\ dx_i &= \delta l_i \cdot \tan\left(\omega_i - \beta_z\right). \end{aligned} \tag{5.15}$$

Here, δl_i is the differential reading at the glass scale at position i, where ϕ_i is the angle difference measured by the auto-collimator along the Y axis reduced to the first point and ω_i is also an angle difference reduced to the first point but along the Z axis. Furthermore, the mean slope within the local XY plane is β_y and the mean slope within the local XZ plane is β_z. Therefore, the points along the linear rail can be calculated using

$$\boldsymbol{P}_i^{\text{rail}} = \begin{bmatrix} \sum_{i=1}^{n} \delta l_i \\ \sum_{i=1}^{n} dy_i \\ \sum_{i=1}^{n} dz_i \end{bmatrix}. \tag{5.16}$$

However, due to the non-straightness determined using (5.16) there must be a deviation between the distance calculated between two laser tracker points and two glass scale readings. This deviation is dependent on the offset between the optical centre of the retro-reflector and the encoder reading head. The retro-reflector's offset can be taken to account using the following equation

$$\boldsymbol{P}_i^{\text{off}} = \boldsymbol{P}_i^{\text{rail}} + \boldsymbol{R}_Z\left(\phi_i - \beta_y\right) \cdot \boldsymbol{R}_Y\left(\omega_i - \beta_z\right) \cdot \boldsymbol{O}. \tag{5.17}$$

Here, $\boldsymbol{R}_Z$ is the rotation matrix around the Z axis using the angle difference $(\phi_i - \beta_y)$ and $\boldsymbol{R}_Y$ is the rotation matrix around the Y axis using the angle difference $(\omega_i - \beta_z)$. The offset due to the reflector is given by $\boldsymbol{O}$ which results in the offset point $\boldsymbol{P}_i^{\text{off}}$. Using equation 5.17 the deviation between the linear glass scale reading and the length calculated from retro-reflector positions can be determined using

$$d_i = \sum_{i=1}^{n} \delta l_i - \overline{\boldsymbol{P}_i^{\text{off}}\,\boldsymbol{P}_1^{\text{off}}} \tag{5.18}$$

Here, $\overline{\boldsymbol{P}_i^{\text{off}}\,\boldsymbol{P}_1^{\text{off}}}$ is the distance between the retro-reflector at position 1 and at position i. The deviation d_i is a combined result of the retro-reflector offset in conjunction with

the non-straightness of the linear rail. An example of the order of d_i can be found in subsection 6.4. Besides this deviation, the reading of the glass scale is also affected by the non-straightness of the linear rail. An estimate of this deviation can be calculated using

$$d_i^G = h \cdot \tan(\omega_i - \beta_z). \tag{5.19}$$

Where h is the maximum height between the glass scale and the reading head and the resulting deviation due to the non-straightness is d_i^G.

Due to the materials used, the straightness is sensitive to temperature changes, this means that the temperature has to be monitored and if necessary the deviation of the straightness must be determined again at the other temperatures, so that it is considered in the right way within the uncertainty budget. In subsection 6.4 the deviation due to a temperature change of 0.2 °C can be seen.

Glass Scale and Eigenfrequency

The glass scale used is a Heidenhain scale having a specified accuracy in the range of roughly ±1.6 µm/m. Even if, the glass scale had a high accuracy after the manufacturing it is possible that due to the installation on the mounting surface it has lost a degree of its high accuracy. Aside from this, it is also very likely that the glass scale is not completely parallel to the moving axis of the linear rail. In both cases, the readings of the glass scale needs to be checked. The glass scale is checked against a two axis glass scale having a higher accuracy which is specified to ±0.6 µm/m. For this purpose, a two axis glass scale can be placed in parallel, beside the glass scale itself and its two additional reading heads can be attached to the same carriage. The two reading heads are connected to the same electronic analysis unit, so that all readings are synchronized. As this two axis glass scale is not suitable for measurements at high speed, it is not used as the primary glass scale on the granite block.

There are strict requirements for the mounting surface for both parts, the linear rail and the glass scale especially in terms of flatness. Besides this a low temperature coefficient is also needed to preserve the straightness of the linear rail. Therefore, a purpose-built granite block was chosen as a mounting surface. This granite block is mounted on a metal support frame with adjustable joints to level it, while not placing any horizontal forces onto the granite block. Even if, the granite block together with its support frame is supposed to be stable, because of its weight of 1.5 t, it might be that the entire object oscillates at its eigenfrequency. Due to the fact that the laser tracker cannot be placed on the same granite block, any resulting eigenfrequency leads to error. This is why any oscillation of the object must be carefully monitored when the carriage is moving along the rail. For this purpose, the two axis glass scale can be used, if the reading head is decoupled from the granite block or the metal support frame. The readings are synchronized by using the same electronic analysis unit which additionally generates the trigger signal for the laser tracker.

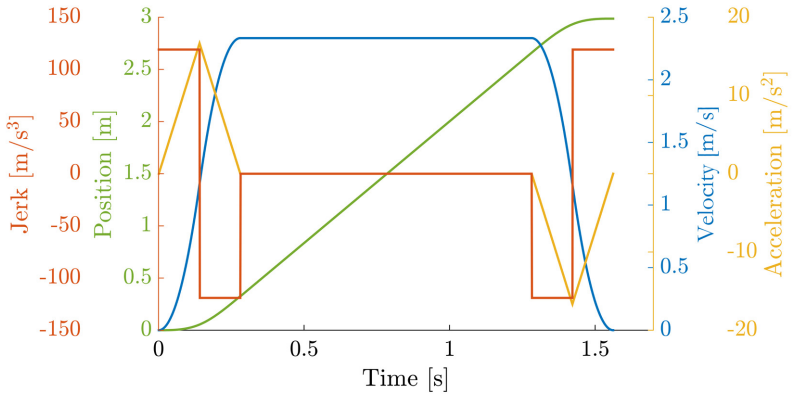

Figure 5.2: S-Ramp Velocity profile

Motion Profiles

The maximum working length is roughly 2.5 m and the maximum speed is 8 m/s. In order to reveal kinematic issues when using a laser tracker, three different kind of motion profiles were implemented into the programmable servo drive. As can be seen in VDI 2143 [2002], there are a lot of different motion profiles, which can be implemented. Alongside this catalogue, other motion profiles can be developed which are more appropriate to fulfil the application's need. In general, these motion profiles can be separated using their velocity, acceleration and jerk profile. Even if, there are some user specified variables, these cannot be chosen arbitrarily, they must be specified with regard to the real object, meaning factoring in the motor, the servo drive, the payload, the linear rail length etc. ...

S-Ramp

The simplest profile for a point to point movement at a constant velocity is the trapezoidal profile. However, when using this profile the jerk is infinite at the points where an acceleration change happens. This may cause high-frequency oscillatory motion and disrupts smooth operation [Gurocak, 2015]. Therefore, the s-ramp profile was implemented to achieve a finite jerk and so smoothing the movement. Unlike to the trapezoidal profile the acceleration is not constant but changes over time. Figure 5.2 shows a s-ramp profile together with its velocity, acceleration and jerk profile. This s-ramp profile consists of

five different phases. The first two and the last two phases are derived from a cubic polynomial

$$s(t) = C_1 t^3 + C_2 t^2 + C_3 t + C_4 \tag{5.20}$$
$$v(t) = 3 C_1 t^2 + 2 C_2 t + C_3 \tag{5.21}$$
$$a(t) = 6 C_1 t + 2 C_2 \tag{5.22}$$
$$r(t) = 6 C_1 \tag{5.23}$$

which are the principal equations of this motion profile. Here, C_1 to C_4 are constants which must be determined with respect to some boundary conditions, as described below. The velocity profile over time is given by $v(t)$, the position profile by $s(t)$, the acceleration profile by $a(t)$ and the jerk profile by $r(t)$.

The phases are divided according to the acceleration profile, which is shown in yellow in figure 5.2. This means, that during the first phase the acceleration is constantly increasing up to half of the specified acceleration time, t_a, where it reaches the specified maximal acceleration for this profile. In the following phase, the acceleration is constantly decreasing from time $\frac{t_a}{2}$ up to time t_a. Within the next phase, the acceleration is constant zero, but the object is moving at a constant velocity, which is its maximum velocity as specified. During phase number four there is constant deceleration, lasting half of the specified acceleration time. At the end of this phase, the maximum deceleration is reached. After this point, there is again acceleration in the last phase lasting half the specified acceleration time as before, and reaching an acceleration of zero at the end as well as a zero velocity.

To calculate the constants, C_1 to C_4 the user must specify the maximum velocity V_m and the acceleration time t_a. However, instead of specifying the acceleration time also the maximum acceleration A_m can be specified, because they can be related to each other using the following equation

$$A_m = \frac{2 V_m}{t_a}. \tag{5.24}$$

Using the conditions specified above leads to the following equations and finally to the required constants C_1^{I} to C_4^{I} for the first phase

$$\begin{aligned}
s(0) = 0 &\xrightarrow{eq.(5.20)} C_4^{\mathrm{I}} = 0 \\
v(0) = 0 &\xrightarrow{eq.(5.21)} C_3^{\mathrm{I}} = 0 \\
a(0) = 0 &\xrightarrow{eq.(5.22)} C_2^{\mathrm{I}} = 0 \\
a\left(\frac{t_a}{2}\right) = A_m &\xrightarrow{eq.(5.22) \wedge C_2^{\mathrm{I}}} C_1^{\mathrm{I}} = \frac{A_m}{3 t_a}.
\end{aligned} \tag{5.25}$$

Here, the equation and the constant above the arrow are used to derive the solution of the given constant. The exponent of a constant C^{I} denotes the phase the constant belongs to.

Using the solutions of the first phase (5.20) to (5.23) as well as (5.25) and applying the conditions on the second phase then the constants for the second phase can be determined as follows,

$$\begin{aligned}
s\left(\frac{t_a}{2}\right) &= \frac{A_m\, t_a^2}{24} & \xrightarrow{eq.(5.20) \wedge C_1^{\mathrm{II}} \wedge C_2^{\mathrm{II}} \wedge C_3^{\mathrm{II}}} & & C_4^{\mathrm{II}} &= \frac{A_m\, t_a^2}{12} \\
v\left(\frac{t_a}{2}\right) &= \frac{A_m\, t_a}{4} & \xrightarrow{eq.(5.21) \wedge C_1^{\mathrm{II}} \wedge C_2^{\mathrm{II}}} & & C_3^{\mathrm{II}} &= -\frac{A_m\, t_a}{2} \\
a\left(t_a\right) &= 0 & \xrightarrow{eq.(5.22) \wedge C_1^{\mathrm{II}}} & & C_2^{\mathrm{II}} &= A_m \\
r\left(\frac{t_a}{2}\right) &= -\frac{2\, A_m}{t_a} & \xrightarrow{eq.(5.23)} & & C_1^{\mathrm{II}} &= -\frac{A_m}{3\, t_a}.
\end{aligned} \tag{5.26}$$

The equations and the constants applied to find the solution of the constants of the second phase, C^{II}, are written above the arrow.

Owing to the fact that within the constant velocity phase the acceleration and the jerk is zero, but the velocity remains constant, the position of the carriage can be calculated as being

$$s\left(t\right) = s(t_a) + V_m\, t. \tag{5.27}$$

Here, $s\left(t\right)$ is the position of the carriage after the acceleration and the duration of the this phase must be specified by the user as well.

Beyond the constant velocity phase, the time variable was rest to zero to derive the constants' of phase four, C^{IV}, which can be found by applying the following conditions

$$\begin{aligned}
s\left(0\right) &= s_{\mathrm{all}} & \xrightarrow{eq.(5.20)} & & C_4^{\mathrm{IV}} &= s_{\mathrm{all}} \\
v\left(0\right) &= V_m & \xrightarrow{eq.(5.21)} & & C_3^{\mathrm{IV}} &= V_m \\
a\left(0\right) &= 0 & \xrightarrow{eq.(5.22)} & & C_2^{\mathrm{IV}} &= 0 \\
a\left(\frac{t_a}{2}\right) &= -A_m & \xrightarrow{eq.(5.22)} & & C_1^{\mathrm{IV}} &= -\frac{A_m}{3\, t_a}.
\end{aligned} \tag{5.28}$$

Here, s_{all} is the position of the movement in total, meaning the end position of the constant velocity phase, which can be calculated using (5.27). For a real movement the results must be adjusted for the time of the constant movement and the first and second phases, as the time variable t was rest to zero to derive the constants in effect for phases three and four.

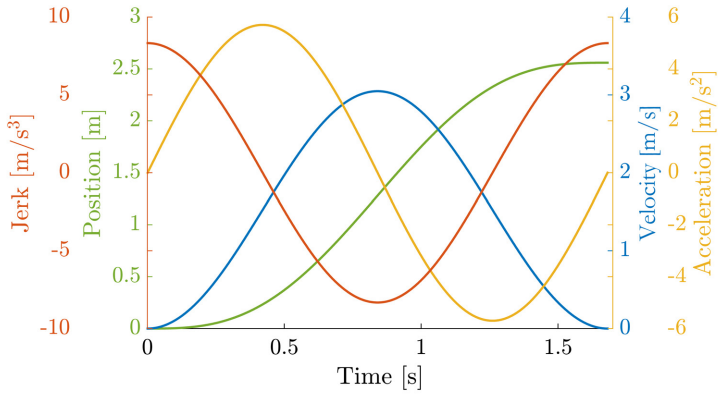

Figure 5.3: $\sin^2$ Velocity profile

Finally, the constants of the last phase, C^{V}, can be determined using the following equations, when taking account of the results of the former phase,

$$
\begin{aligned}
s\left(\frac{t_a}{2}\right) &= \frac{A_m\, t_a^2}{24} && \xrightarrow{eq.(5.20)\wedge C_1^{\mathrm{V}}\wedge C_2^{\mathrm{V}}\wedge C_3^{\mathrm{V}}} && C_4^{\mathrm{V}} = -\frac{A_m\, t_a^2}{12} + s_{\mathrm{all}} \\
v\left(\frac{t_a}{2}\right) &= \frac{A_m\, t_a}{4} && \xrightarrow{eq.(5.21)\wedge C_1^{\mathrm{V}}\wedge C_2^{\mathrm{V}}} && C_3^{\mathrm{V}} = \frac{A_m\, t_a}{2} + V_m \\
a\left(t_a\right) &= 0 && \xrightarrow{eq.(5.22)\wedge C_1^{\mathrm{V}}} && C_2^{\mathrm{V}} = -A_m \\
r\left(\frac{t_a}{2}\right) &= \frac{2\, A_m}{t_a} && \xrightarrow{eq.(5.23)} && C_1^{\mathrm{V}} = \frac{A_m}{3\, t_a}.
\end{aligned}
\tag{5.29}
$$

When using the equations from (5.20) to (5.29) the entire motion profile can be calculated, as shown in figure 5.2, and used to control by the programmable servo drive.

$\sin^2$ Velocity Shape Profile

A profile having a $\sin^2$ shape velocity profile was implemented, to challenge the laser tracker, because the acceleration is continuously changing, which is solely the case during the acceleration and deceleration time when applying the s-ramp profile. In figure 5.3 the profile with its velocity, acceleration and jerk profile is illustrated. Taking into account both figures 5.2 and 5.3 it can seen that the jerk function is limited, but there are jumps within the jerk profile for the s-ramp as well as for the $\sin^2$-shape profile. The motion

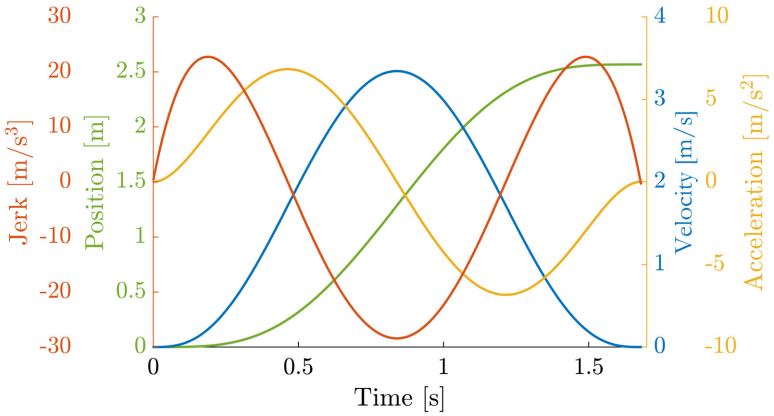

Figure 5.4: Septic polynomial profile

profile can be calculate using the following equations

$$s(t) = \frac{t\, s_{\text{spec}}}{t_{\text{spec}}} - \frac{s_{\text{spec}}}{2\pi} \sin\left(\frac{2\pi\, t}{t_{\text{spec}}}\right) \tag{5.30}$$

$$v(t) = \frac{2\, s_{\text{spec}}}{t_{\text{spec}}} \sin\left(\frac{\pi\, t}{t_{\text{spec}}}\right)^2 \tag{5.31}$$

$$a(t) = \frac{2\,\pi\, s_{\text{spec}}}{t_{\text{spec}}^2} \sin\left(\frac{2\,\pi\, t}{t_{\text{spec}}}\right) \tag{5.32}$$

$$r(t) = \frac{4\,\pi^2\, s_{\text{spec}}}{t_{\text{spec}}^3} \cos\left(\frac{2\,\pi\, t}{t_{\text{spec}}}\right). \tag{5.33}$$

For these derivatives, the equation $\sin^2(x) = \frac{1}{2}(1 - \cos(2\,x))$ was used. Here, s_{spec} is the maximum distance the carriage can travel specified by the user, and t_{spec} specifies the time duration to travel the maximum distance. Taking into account equation (5.31), the maximum velocity can be calculated as being

$$V_m = \frac{2\, s_{\text{spec}}}{t_{\text{spec}}}. \tag{5.34}$$

Septic Polynomial

To test a laser tracker using a profile having a continuous jerk function a polynomial having the degree 7 was implemented, obeying the condition of a zero jerk at the beginning and at the end. Figure 5.4 shows an example of this profile. The principal equations of

this motion profile are

$$s(t) = C_1 t^7 + C_2 t^6 + C_3 t^5 + C_4 t^4 + C_5 t^3 + C_6 t^2 + C_7 t + C_8 \tag{5.35}$$
$$v(t) = 7 C_1 t^6 + 6 C_2 t^5 + 5 C_3 t^4 + 4 C_4 t^3 + 3 C_5 t^2 + 2 C_6 t + C_7 \tag{5.36}$$
$$a(t) = 42 C_1 t^5 + 30 C_2 t^4 + 20 C_3 t^3 + 12 C_4 t^2 + 6 C_5 t + 2 C_6 \tag{5.37}$$
$$r(t) = 210 C_1 t^4 + 120 C_2 t^3 + 60 C_3 t^2 + 24 C_4 t + 6 C_5. \tag{5.38}$$

Here, C_1 to C_8 are constants which need to be determined with respect to the boundary conditions. At the beginning of the movement, it is necessary that the carriage is at its zero starting position, that the velocity is zero at this point as well as the acceleration. Additionally, it is required that the jerk of this profile is zero at the beginning. Taking account of these conditions, the constants C_5 to C_8 can be shown to be

$$\begin{aligned} s(0) = 0 \quad &\xrightarrow{eq.(5.35)} \quad C_8 = 0 \\ v(0) = 0 \quad &\xrightarrow{eq.(5.36)} \quad C_7 = 0 \\ a(0) = 0 \quad &\xrightarrow{eq.(5.37)} \quad C_6 = 0 \\ r(0) = 0 \quad &\xrightarrow{eq.(5.38)} \quad C_5 = 0. \end{aligned} \tag{5.39}$$

The conditions at the end of the movement are that the carriage is at the specified position s_{spec} in a specified time t_{spec} and at this time, the velocity, the acceleration, as well as the jerk must be zero. By using these conditions in conjunction with the solution of C_5 to C_8 and the principal equations (5.35) to (5.38) an equation system can be set up to solve for the constants C_1 to C_8 as follows,

$$\begin{bmatrix} t_{\text{spec}}^7 & t_{\text{spec}}^6 & t_{\text{spec}}^5 & t_{\text{spec}}^4 \\ 7\,t_{\text{spec}}^6 & 6\,t_{\text{spec}}^5 & 5\,t_{\text{spec}}^4 & 4\,t_{\text{spec}}^3 \\ 42\,t_{\text{spec}}^5 & 30\,t_{\text{spec}}^4 & 20\,t_{\text{spec}}^3 & 12\,t_{\text{spec}}^2 \\ 210\,t_{\text{spec}}^4 & 120\,t_{\text{spec}}^3 & 60\,t_{\text{spec}}^2 & 24\,t_{\text{spec}} \end{bmatrix} \begin{bmatrix} C_1 \\ C_2 \\ C_3 \\ C_4 \end{bmatrix} = \begin{bmatrix} s_{\text{spec}} \\ 0 \\ 0 \\ 0 \end{bmatrix} \tag{5.40}$$
$$C_1 = -\frac{20\,s_{\text{spec}}}{t_{\text{spec}}^7} \qquad C_2 = \frac{70\,s_{\text{spec}}}{t_{\text{spec}}^6}$$
$$C_3 = -\frac{84\,s_{\text{spec}}}{t_{\text{spec}}^5} \qquad C_4 = \frac{35\,s_{\text{spec}}}{t_{\text{spec}}^4}.$$

The septic polynomial motion profile, as figure 5.4 shows, can be calculated by using these constants in conjunction with the principal equations (5.35) to (5.38).

Chapter 6

Experiments and Results

In order to verify the derived probabilistic measurement model, two different kinds of kinematic 'ground truths' were used. The first, was the multilateration system, were arbitrary trajectories could be tested, but there were some restrictions in terms of the maximum velocity and acceleration. The second, was verification using the glass scale and linear-rail ground truth, which has far less restrictions on the velocity and acceleration, but does not allow arbitrary trajectories.

In addition, the entire analysis method was tested in different kind of application scenarios in conjunction with an industrial robot. These scenarios included one that incorporated the control information from an industrial robot, but also one where the movement was known in advance as well as one using a more simplified motion model.

6.1 Simplified and Known Movement in Advance

In Ulrich [2013] an industrial 6 axis robot was programmed to move a reflector along a predefined trajectory, at a constant speed of 500 mm/s. The trajectory consisted of the edges of a cube and semicircles on its sides, as can be seen in figure 6.1. Throughout the movement a Leica laser tracker AT901 and Leica laser tracker LTD500 observed the reflector. During this experiment the robot's control information could not be incorporated into the analysis method as described in section 3.2.

By taking into account the trajectory three system models could be considered within a hybrid system estimator. Here, the hybrid system estimator was an IMM filter, as presented in section 3.3 using a constant velocity model, a constant acceleration model and a constant turn model (also known as coordinated turn model). The constant velocity model should represent the major part of the trajectory where the robot was programmed to move at a constant velocity. In order to model the transition from

one cube plane to another, as well as to model the semicircle, the constant turn model was implemented. Furthermore, to consider the acceleration along the trajectory e.g. before and after a transition on another cube plane, the constant acceleration model was integrated. The hybrid system estimator result was compared to the result of a common Kalman filter using the system model constant velocity as an example of s simplified movement analysis. Beside this comparison the result of the IMM was also compared to the result of a RMIMM.

The first model in the hybrid system estimator was the constant velocity model, using the state space vector $\boldsymbol{x} = [x\, y\, z\, \dot{x}\, \dot{y}\, \dot{z}]^\mathsf{T}$. The discrete-time state equation is

$$\boldsymbol{x}_{t+1}^{\mathrm{I}} = \begin{bmatrix} \boldsymbol{I}^{3\times3} & \Delta t\, \boldsymbol{I}^{3\times3} \\ \boldsymbol{0} & \boldsymbol{I}^{3\times3} \end{bmatrix} \boldsymbol{x}_t + \boldsymbol{w}_t^{\mathrm{I}}. \tag{6.1}$$

Here the sampling period is Δt and the discrete-time process noise is $\boldsymbol{w}_t^{\mathrm{I}}$. The covariance matrix is

$$\mathrm{cov}\left(\boldsymbol{w}_t^{\mathrm{I}}\right) = \begin{bmatrix} \frac{1}{3}\Delta t^3\, \boldsymbol{I}^{3\times3} & \frac{1}{2}\Delta t^2\, \boldsymbol{I}^{3\times3} \\ \frac{1}{2}\Delta t^2\, \boldsymbol{I}^{3\times3} & \Delta t\, \boldsymbol{I}^{3\times3} \end{bmatrix} \tilde{q}. \tag{6.2}$$

The constant acceleration model, the second model within the hybrid system estimator, was modelled using the discrete-time state equation

$$\boldsymbol{x}_{t+1}^{\mathrm{II}} = \begin{bmatrix} \boldsymbol{I}^{3\times3} & \Delta t\, \boldsymbol{I}^{3\times3} & \frac{1}{2}\Delta t, \boldsymbol{I}^{3\times3} \\ \boldsymbol{0} & \boldsymbol{I}^{3\times3} & \Delta t\, \boldsymbol{I}^{3\times3} \\ \boldsymbol{0} & \boldsymbol{0} & \boldsymbol{I}^{3\times3} \end{bmatrix} \boldsymbol{x}_t + \boldsymbol{w}_t^{\mathrm{II}}. \tag{6.3}$$

Here $\boldsymbol{x}^{\mathrm{II}} = [x, y, z, \dot{x}, \dot{y}, \dot{z}, \ddot{x}, \ddot{y}, \ddot{z}]^T$ is the sate space vector and the covariance matrix of the discrete-time process noise $\boldsymbol{w}_t^{\mathrm{II}}$ can be expressed as

$$\mathrm{cov}\left(\boldsymbol{w}_t^{\mathrm{II}}\right) = \begin{bmatrix} \frac{1}{20}\Delta t^5\, \boldsymbol{I}^{3\times3} & \frac{1}{8}\Delta t^4\, \boldsymbol{I}^{3\times3} & \frac{1}{6}\Delta t^3\, \boldsymbol{I}^{3\times3} \\ \frac{1}{8}\Delta t^4\, \boldsymbol{I}^{3\times3} & \frac{1}{3}\Delta t^3\, \boldsymbol{I}^{3\times3} & \frac{1}{2}\Delta t^2\, \boldsymbol{I}^{3\times3} \\ \frac{1}{6}\Delta t^3\, \boldsymbol{I}^{3\times3} & \frac{1}{2}\Delta t^2\, \boldsymbol{I}^{3\times3} & \Delta t\, \boldsymbol{I}^{3\times3} \end{bmatrix} \tilde{q}. \tag{6.4}$$

The matrix was derived by discretizing the continuous time model, with additional noise using the inverse Laplace transformation as proposed in Bar-Shalom et al. [2001]; Ulrich [2015].

The third model within the hybrid system estimator filter, was the constant turn model. A planar constant turn in the navigation plane can be described using

$$\dot{\boldsymbol{x}}^{\mathrm{III}}(t) = \begin{bmatrix} \boldsymbol{0} & \boldsymbol{I}^{3\times3} & \boldsymbol{0} \\ \boldsymbol{0} & \boldsymbol{0} & \boldsymbol{I}^{3\times3} \\ \boldsymbol{0} & -\omega^2\, \boldsymbol{I}^{3\times3} & \boldsymbol{0} \end{bmatrix} \boldsymbol{x}(t) + \begin{bmatrix} \boldsymbol{0} \\ \boldsymbol{0} \\ \boldsymbol{I}^{3\times3} \end{bmatrix} \boldsymbol{w}^{\mathrm{III}}(t) \tag{6.5}$$

according to Li and Jilkov [2003]. Here, $\boldsymbol{x}^{\mathrm{III}} = [x, y, z, \dot{x}, \dot{y}, \dot{z}, \ddot{x}, \ddot{y}, \ddot{z}]^T$ is the state vector and $\boldsymbol{w}^{\mathrm{III}}$ is the process noise. The turn rate is ω. A deduction of the discrete time model

and its covariance matrix can be found in Li and Jilkov [2003] and in Ulrich [2015]. Within Ulrich [2013] the state space vector $\boldsymbol{x}^{\mathrm{III}}$ was augmented with the turn rate, as well as the covariance matrix, as proposed in Li and Jilkov [2003].

For all three system models, an appropriate Bayesian filter was needed in an IMM filter. As the constant velocity and the constant acceleration model are linear, a common Kalman filter is ideally suited, if the measurements can be assumed to be normally distributed. Due to the non-linearity of the constant turn model, the said filter, needs to be modelled on an extended Kalman filter, particle filter or unscented Kalman filter. In Ulrich [2013] it was shown, that the laser tracker measurement can be considered as obeying a normal distribution. This was done by applying two different tests, the Anderson-Darling test and the Lilliefors test. In consequence, a common Kalman filter was used for the constant velocity and the constant acceleration model. The constant turn model was implemented within an unscented Kalman filter as it is more convenient to use rather than a particle filter, if the underlying distribution can be approximated as a normal distribution [Ulrich, 2013].

Due to the fact that the variance of a point is dependent on the state vector of the object, which was different for each model in the IMM filter, the covariance matrix $\boldsymbol{\Sigma}_t^i$ needs to be determined for each time instant t. In Ulrich [2013] the Monte Carlo method was used in conjunction with equation (4.14).

In figure 6.1a, the trajectory is displayed together with the speed of the robot. Especially, at the corners it had to slow down and speed up again, everywhere else it maintained a constant speed. For figures 6.1a to 6.2b the graphs are depicted within the laser tracker's coordinate system. The approximated manufacturer's specification of the standard deviations of the laser tracker measurements along this trajectory, are depicted in 6.1b. Here it was assumed that the laser tracker's accuracy is $\pm 20\,\mu\mathrm{m/m}$ as proposed in Ulrich [2013] according to the manufacturer's specification.

As the robot moved at an almost consistent speed, the collected data were also analysed using a common Kalman filter, with a constant velocity model and the manufacturer's specification was used as the measurement model. The resulting standard deviation of this analysis can be seen in figure 6.2a. Additionally, the data were analysed using the IMM filter, with the models as explained above, in conjunction with the augmented measurement model of the laser tracker, as proposed in Ulrich [2013] and explained in section 4.1. The standard deviation determined can be seen in figure 6.2b. In order to compare these methods, the mean standard deviation of all methods was calculated and summarized in table 6.1.

When taking into account figures 6.1b to 6.2b and table 6.1, it can see that the IMM filter, in conjunction with the augmented measurement model, achieves a significantly better uncertainty estimation than either a Kalman filter or the manufacturer's approximation can provide. This is mainly because the actual kinematic behaviour can be better taken into consideration due to the continuous adaptation of the probable system models. Furthermore, the over-shoots of the Kalman filter approach could be avoided as shown

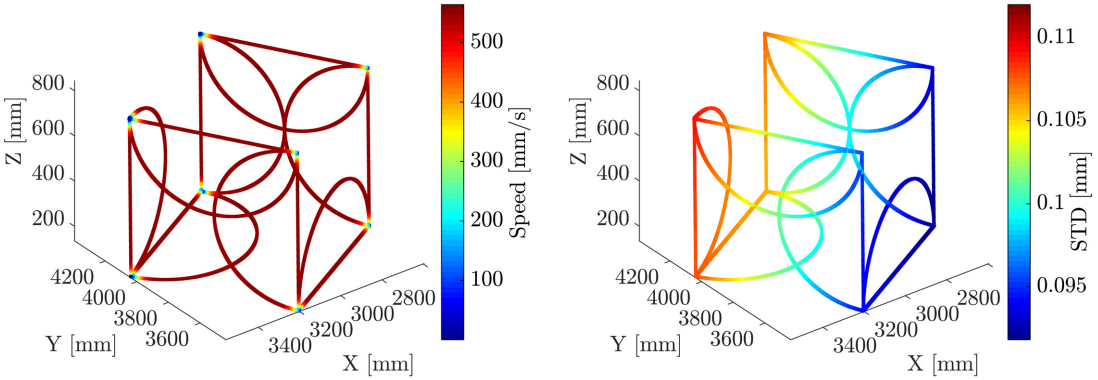

(a) Speed reached for each point.

(b) Specification

Figure 6.1: The speed of the robot along the trajectory together with the specified accuracy of the laser tracker, as presented in Ulrich [2013].

in Ulrich [2013], because it considers more than one system model, as a result the IMM approach is more suitable to complex kinematic trajectories. In Ulrich [2013] a sensor

	IMM	Specific.	KF
Mean standard deviation [mm]	0.024	0.102	0.074

Table 6.1: Comparison between the analysis methods.

fusion between two laser trackers within an IMM filter was also considered, as outlined in section 4.2. The fusion achieved an improvement of roughly 25 %. In addition, an improved version of the IMM filter the RMIMM filter was considered in Ulrich [2013] although no significant deviation between these two versions of a hybrid system estimator was found.

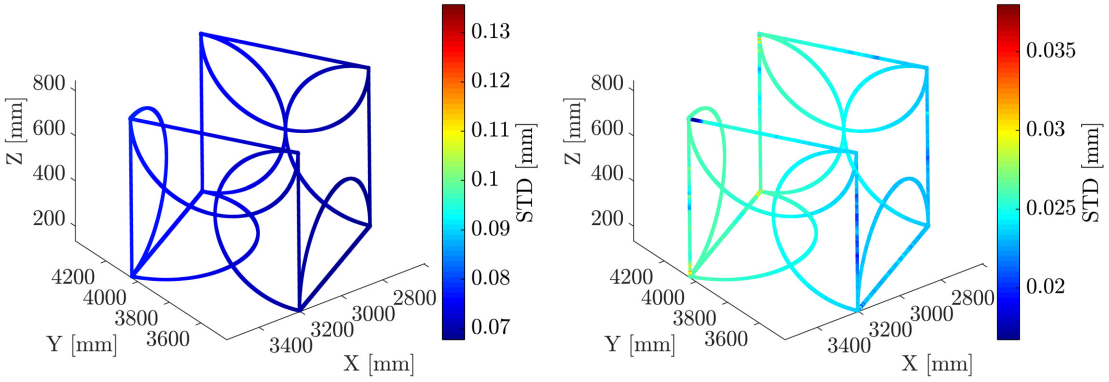

(a) Kalman Filter **(b)** IMM Filter

Figure 6.2: Bayesian filter analysis methods, comparing the hybrid system estimator approach with the Kalman filter approach, as presented in Ulrich [2013].

6.2 Known Movement at any Time

The experiments described within the following two subsections were carried out using an industrial robot a KUKA KR 5 ARC in conjunction with a Leica laser tracker AT901, some experiments were published in Ulrich and Irgenfried [2014]. A corner cube reflector (CCR) was used as a retro-reflector, which was attached to the robot's TCP using a purpose-built adapter. As the laser tracker and the industrial robot measure within their own coordinate frames, the corresponding coordinate frames need to be transformed into each other. The determination of these transformation parameters is also known as hand-eye transformation. To determine these parameters, an initialization trajectory was used, spread all over the designated measuring volume to gain representative parameters. The transformation parameters consisted of a translation vector and a rotation matrix.

The experiments were set up to allow the motion control from an external PC, running a custom developed position control program. A list of trajectory key points was entered to the control program which controls the robot's motion in terms of direction and speed along the key points. This program linearly interpolates the key points and communicates with the robot's controller using KUKA Robot Sensor Interface (RSI) Extensible Markup Language (XML)-based User Datagram Protocol (UDP)-Ethernet communication. Path planning was done by the program in Cartesian coordinate system, whereas the robot control calculates the inverse kinematics. The control program also sent a TTL trigger signal in order to synchronize the robot's motion with the laser tracker.

A model of an industrial robot is generally highly non-linear, especially in dynamic cases, as can be seen in Wiest [2001] and Corke [2011]. However, these calculations were carried out by the robot's controller, which solely delivered the processed data back to the position control program, as described above. In consequence, the system model

could be regarded as being linear, and the robot's covariance matrix was derived from the manufactures specification. Owing to the fact that the analysis took place in the laser tracker's coordinate system, the covariance matrix of the industrial robot had to be adjusted in order to include the hand-eye transformation uncertainty. The final Bayesian filter implemented was a simple Kalman filter, because of the normal distribution and the linearity of the system model. The authors Simon [2006] and Thrun et al. [2005] went into detail about a Kalman filter. In addition to this, alternative equations were discussed in Bierman [2006] to overcome numerical and stabilization issues resulting from the analysis method.

Ulrich [2012] showed that despite the non-linearity of equation (4.14), the laser tracker values can be taken to be normal distributed. This means that the laser tracker value can be represented by its mean and covariance matrix. In consequence, as measurement model of the laser tracker, the Monte Carlo method was used in conjunction with, equation (4.14) in order to determine a covariance matrix, as already proposed in Ulrich [2012, 2013] and explained in subsection 6.1. Because equation (4.14) requires the object velocity, the velocity provided by the robot controller was used.

Incorporating an Industrial Robot's Control Information

Within the Bayesian analysis method the information from the robot together with its covariance matrix were used as the predicted prior PDF. Every 16 ms, a trigger impulse from the robot generated a laser tracker measurement. This information in conjunction with the predicted prior PDF, is used to generate a new measurement covariance matrix, as outlined in subsection 6.1. Furthermore, the desired posterior PDF of the trajectory was calculated using a Kalman filter update step as being

$$[\hat{\boldsymbol{x}}_t, \boldsymbol{P}_t] = \mathrm{KF}_u \left(\hat{\boldsymbol{x}}_t^-, \boldsymbol{P}^-, \boldsymbol{z}_t, \boldsymbol{\Sigma}_t \right). \tag{6.6}$$

The update function is denoted by KF_u, which uses the predicted prior PDF, represented by the predicted state estimate $\hat{x}_t^-$ and the predicted covariance matrix $\boldsymbol{P}^-$, which was made up of the robot's covariance matrix and the transformation covariance as described above. The laser tracker measurement is stored in vector $\boldsymbol{z}_t$ and the covariance matrix determined is $\boldsymbol{\Sigma}_t$. The desired posterior PDF of the CCR's position along the trajectory at time t is represented by the estimated mean $\hat{\boldsymbol{x}}_t$ of the state vector and its covariance matrix $\boldsymbol{P}_t$.

In Ulrich and Irgenfried [2014] two experiments were carried out, one with an additional weight attached to the robot, roughly 3.5 kg, and one without. The control program was configured to reach exactly the key points along the trajectory. Using the robot's repeatability of 40 µm the velocity variance of the system was estimated to 57 µm/s. Additionally, the absolute position variance of the system model was estimated to 322 µm, using some prior knowledge about the robot and including the standard deviation of the transformation parameter.

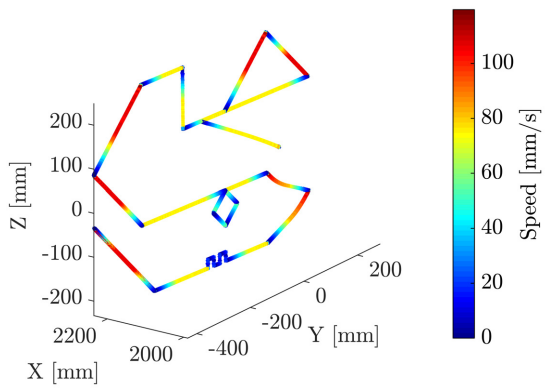

(a) The robot speed along the trajectory displayed in the laser tracker coordinate system as similar presented in Ulrich and Irgenfried [2014].

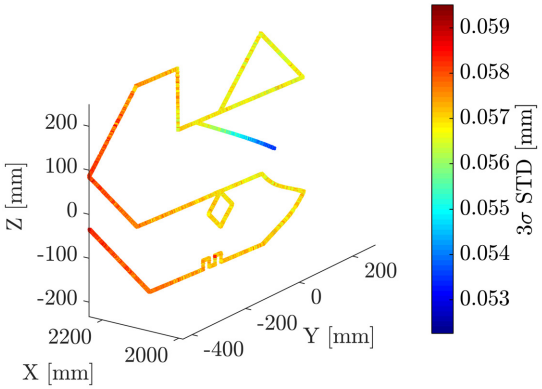

(b) Estimated laser tracker uncertainty using the proposed approach. The 3σ standard deviation is displayed in the laser tracker coordinate system as similar presented in Ulrich and Irgenfried [2014].

Figure 6.3: The estimated laser tracker uncertainty together with the robot speed along the trajectory.

The result of the laser tracker uncertainty analysis is depicted in figure 6.3b which is the result of the experiment without additional weight using the 3σ-interval. In figure 6.3a the robot's speed is depicted. The range dependency in figure 6.3b shows that the speed throughout the experiment was not fast enough so that the kinematic uncertainty effects overlap the range dependence and the alignment errors. But due to the experiment constellation, meaning the trajectory within the working envelope of the robot, no higher speed could be achieved along this trajectory.

As can be seen in Ulrich and Irgenfried [2014] there were outliers at the beginning of every movement section along the trajectory. These outliers were related to jerks at the beginning of each new motion segment caused by the extremely straightforward path planning approach. This approach were only made up of a linear interpolation with equidistant segments between the key points, together with the maximum acceleration. From looking at the results, the only difference between the experiment with additional weight and the one without appears to be that the range of the outliers were significantly damped down as can be seen with more details in Ulrich and Irgenfried [2014]. These outliers are comparable to the one in figure 6.4a of another experiment, which are further investigated in the following subsection.

Assessing Deviations using a Ground Truth

In difference to the experiment in the last subsection, in this experiment the multilateration system of the PTB was also used, which is explained in detail in section 5.1. The

multilateration system was used to generate a ground truth, specifically in order to verify the derived laser tracker measurement model. Another difference to the experiment in the last subsection is that the key points along the trajectory were only approximate. The trajectory of this experiment can be seen in figure 6.10a and the mean speed along this trajectory was 100 mm/s.

A trigger impulse was issued every 4 ms by the robot which synchronized the laser tracker and laser tracer measurements. The robot data were first transformed into the laser tracker coordinate system then a predicted prior PDF was determined using the system model and its covariance matrix, as described above. This prior PDF was then used together with the laser tracker data to determine a new measurement covariance matrix, as outlined in subsection 6.1 at the beginning of this chapter or explained in more detail in Ulrich and Irgenfried [2014]. Furthermore, the desired posterior PDF of the trajectory was calculated using a Kalman filter update step as shown in equation (6.6).

Additionally, an outlier detection step was performed, according to Thrun et al. [2005], which is a test against a threshold γ as follows

$$(\boldsymbol{z} - \hat{\boldsymbol{z}})^{\intercal}\ \hat{\boldsymbol{S}}^{-1}\ (\boldsymbol{z} - \hat{\boldsymbol{z}}) \leq \gamma, \tag{6.7}$$

where the threshold γ is taken from the inverse χ^2 cumulative distribution at a certain significance level and considering the degrees of freedom. Here, the measurement predicted is denoted using $\hat{\boldsymbol{z}}$. Furthermore, the innovation covariance matrix is $\hat{\boldsymbol{S}}$ which is made up of the predicted covariance matrix $\boldsymbol{P}^{-}$, the measurement covariance matrix $\boldsymbol{\Sigma}$ and the measurement matrix $\boldsymbol{H}$. The innovation covariance matrix can be determined by

$$\boldsymbol{S} = \boldsymbol{H}\boldsymbol{P}^{-}\boldsymbol{H}^{\intercal} + \boldsymbol{\Sigma}. \tag{6.8}$$

The deviations between the laser tracker and the robot are depicted in figure 6.4a, as well as the outliers detected by the test proposed in equation (6.7). These outliers are related to jerks at the beginning of each new motion segment caused by a very basic path planning approach, using linear interpolation with equidistant segments between the key points and applying the maximum possible acceleration at the beginning of each motion segment. A ramp function at the beginning would mitigate or avoid theses jerks currently observable. At the base line, only 3.5 % of the points were detected as outliers when the significance level was set to 0.01. Alongside applying a ramp function to take into account these outliers in the analysis method, a more complex probability system model of the robot could also be applied which would change every time step with respect to the current system state vector. This model requires a much deeper insight into the control system to take into account the current dynamic robot model, which considers at least the friction force, the gravity loading, the joint-space inertia matrix and the Coriolis and centripetal coupling matrix as listed in section 3.2.

However, the mean deviation between the robot's path and laser tracker's ones is 290 µm, which is roughly equal to the expected absolute position uncertainty of this robot. Some

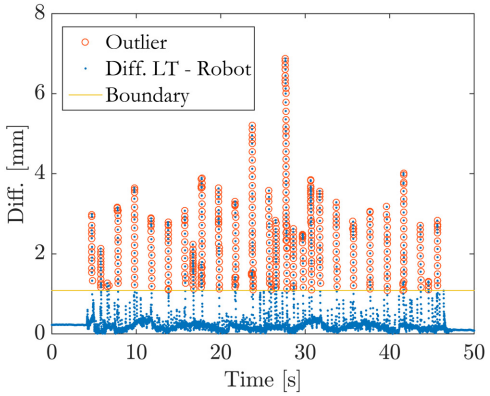

(a) Deviation between the robot and the laser tracker as well as the detected outliers.

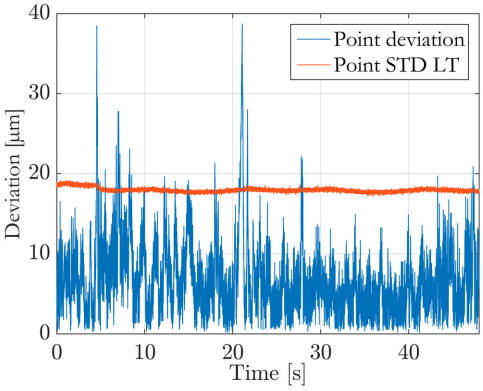

(b) Deviation between the laser tracker and the multilateration system as well as the estimated uncertainty of the laser tracker using the new proposed approach

Figure 6.4: Deviation between robot and laser tracker and deviation between laser tracker and multilateration system.

bigger deviations between robot and laser tracker should be visible if the maximum payload limit is exceeded or if robot manipulator is in an outstretched position.

To verify the results of the proposed analysis method for a laser tracker, a comparison against a ground truth was carried out. The ground truth was generated by the multilateration system of the PTB consisting of four laser tracer. The maximal standard deviation along the trajectory in this experiment was 2 µm, calculated by the refined analysis method. Accordingly, it can be seen as a ground truth for kinematic laser tracker measurements. In figure 6.4b the deviation between the laser tracker and the multilateration is depicted. Furthermore, the estimated standard deviation of the kinematic laser tracker measurement calculated by the proposed approach can be seen. These deviations exceed the standard deviation only in 2.4 % of all measurements, the proposed method can therefore be taken as working reliably. This additionally underpins the fact that the outliers in figure 6.4a were caused by the robot control and the unsophisticated probability model.

6.3 Laser Tracer / Multilateration

The multilateration system of the PTB was used in conjunction with a Leica laser tracker AT901 to observe the trajectory of a corner cube reflector attached to a TCP of a six axis industrial robot. During the experiment, the robot moved the reflector along trajectories which were predefined. Additionally, the robot produced a trigger signal in order to synchronise the robot encoder readings and the measurements of the laser tracker as well

as the measurements of the multilateration system. In this experiment a corner cube air path reflector was used and the roll angle was fixed in order to mitigate additional uncertainties which can be caused by the reflector, as explained in detail in section 4.1. To overcome the limited acceptance angle of this reflector type, the reflector was pointed back by the robot to a stable point in space when it was moved along the trajectories.

Multilateration Ground Truth

In both cases presented in section 5.1 specifically equation (5.6) and (5.14), the standard analysis and the refined analysis, all unknown points of the observed trajectory were used to define the datum.

Due to some restrictions to the robot's axis and the configuration of the laser tracers, all trajectories had to be approximately located in a plane. In addition, in order to achieve a better numerical stability, the TCP were moved along an initialization trajectory in a cube shape at the beginning of the experiment. Niemeier [2008] and Luhmann et al. [2013] showed that the confidence ellipse semi-axis point towards the centroid of the points defining the coordinate system. For this reason only the trajectory points were used in the analysis method as datum points. Not using all of the points as datum points is also known as partial trace minimization.

The points along the trajectory do not have observations between each other, there are only observations between the laser tracer and the points on the trajectory. This means the underlying geometrical network structure is equivalent, even if only a representative portion of points is used to do a weak from analysis. In consequence, the following results were obtained by using full matrix operations, despite the sparsity of the matrix of the system of normal equations. The trajectory was made up of four loops along the ellipse shape which can be seen depicted in orange together with the initialisation cube in blue in figure 6.10b. The coordinate system is the laser tracker coordinate system.Throughout the experiment the average speed of the industrial robot's TCP was 100 mm/s. For this analysis, the standard deviation within the stochastic model's parameter of (5.4) were set to $u_{l.a} = 0.1\,\mu m$ and $u_{l.b} = 0.1\,\mu m/m$.

Standard Analysis Method

By applying the standard analysis method as described above, the deviations between the laser tracker coordinates and the coordinates determined using the multilateration system show a clear systematic pattern along the whole trajectory as can be seen in figure 6.5a. The deviations are within a $\pm 20\,\mu m$ range which is still in accordance with the specification of the laser tracker. Figure 6.5b displays the standard deviation of each component of the 3D multilateration points, which can be regarded as too large to serve as a ground truth. Furthermore, the standard deviation of the laser tracers' positions and dead paths can be considered as being too large which can be seen in table 6.2.

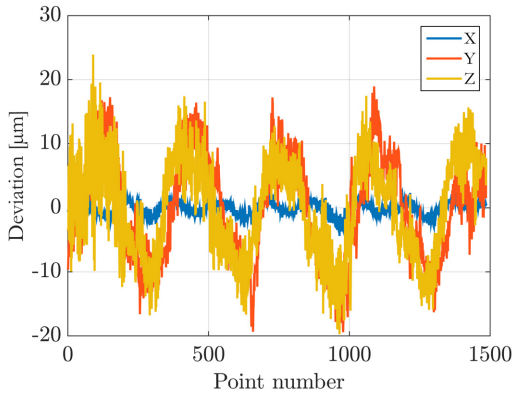

(a) Deviation between the laser tracker coordinates and the multilateration coordinates.

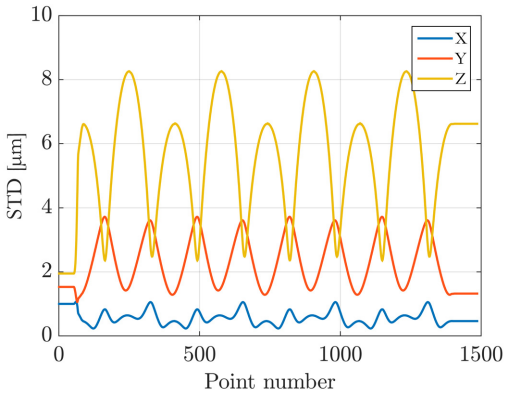

(b) Standard deviation determined for each component of the multilateration coordinates.

Figure 6.5: Results by using the standard method.

	Standard Method					Refined Method				
	Laser tracer position STD [µm]			Dead path STD [µm]		Laser tracer position STD [µm]			Dead path STD [µm]	
Laser tracer	X	Y	Z	1	2	X	Y	Z	1	2
1	96.2	9.0	49.2	98.6	103.9	2.3	0.2	0.7	3.8	2.3
2	78.2	24.4	29.3	77.7	84.1	1.7	0.5	0.4	3.6	1.8
3	78.9	19.9	21.7	74.8	82.0	2.0	0.4	0.3	3.7	2.0
4	49.4	0.8	4.6	39.5	48.4	1.1	0.1	0.1	3.2	1.0

Table 6.2: Standard deviation (STD) of the four laser tracers' position and dead paths' using the standard method and refined method.

As mentioned in 5.1, it is important to know if the network is in its major weak form when assessing coordinate deviations in order to conclusively separate real from unreal deviations. A network follows its major weak form when the residuals at the points, which are defining the datum of the coordinate system, show the same pattern as the eigenvector of the major eigenvalue. When taking into account figure 6.6 a clear and very strong correlation between the major eigenvector and the residual vector can be seen, which means that the network follows its major weak form. This is further supported by looking at the eigenvalue spectrum in figure 6.9a, as there is a dominant major eigenvalue visible for the standard analysis method. Therefore, the deviations of the laser tracker coordinates cannot be taken as being real deviations. Accordingly one cannot assume that there might be systematic error in the laser tracker.

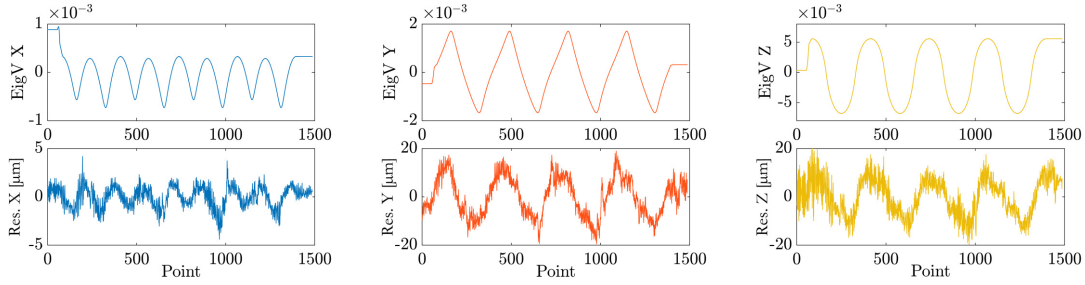

(a) X component **(b)** Y component **(c)** Z component

Figure 6.6: Components of major eigenvector and residual vector of the standard method.

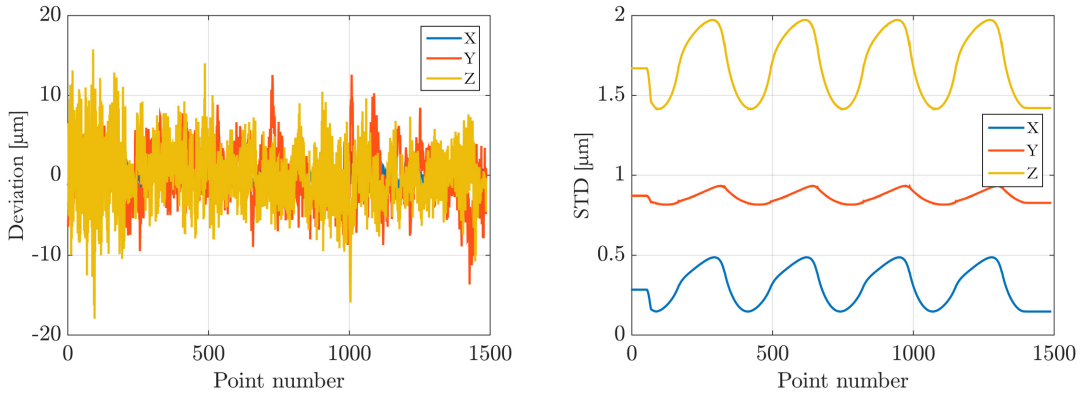

(a) Deviation between the laser tracer coordinates and the multilateration coordinates. The X axis component is mostly covered by the other components

(b) Standard deviation determined for each 3D point component

Figure 6.7: Results by using the refined method.

Refined Analysis Method

When using the multilateration system in conjunction with the refined analysis method, there is no systematic pattern visible within the deviations between the laser tracker coordinates and the coordinates of the multilateration system as can be seen in figure 6.7a. The X axis component is obscured by the other components. In comparison with the standard analysis method, also the range of the deviations decreased to roughly $\pm 10\,\mu m$ with a few peaks up to $\pm 15\,\mu m$. Figure 6.7b illustrates the standard deviation of the 3D points determined which clearly shows a considerable decrease in comparison with the standard deviation of the standard method in figure 6.5b. Furthermore, the standard deviation of the laser tracers' positions dropped significantly, as can be seen in table 6.2 as well as the standard deviation of the laser tracers' dead paths.

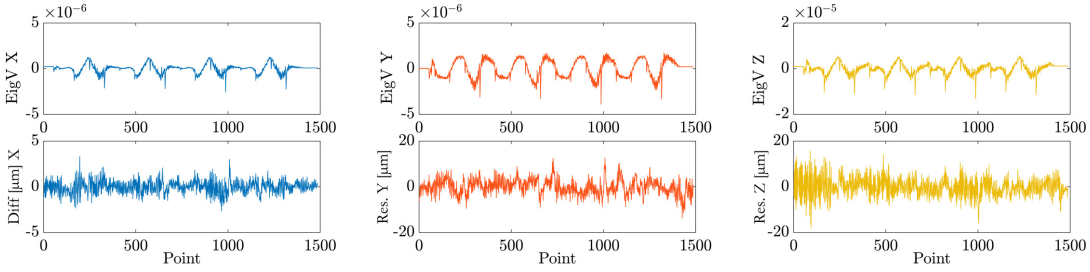

(a) X component **(b)** Y component **(c)** Z component

Figure 6.8: Components of major eigenvector and residual vector of the refined method.

In figure 6.8 the major eigenvector and the residual vector are depicted and there is no correlation visible between them. Consequently, the network does not follow its major weak form implying that the deviation of the laser tracker coordinates can be taken to be real deviations.

Comparison of the Analysis Methods

The eigenvalue spectrum of the standard method together with the refined method are shown in figure 6.9a. Within this figure it can clearly be seen that the refined method attenuated the major eigenvalue appreciably, and therefore the network was not inclined to leave its stable geometry. The eigenvalue spectrum of the refined method also shows a much better network quality overall than the standard analysis method, as can also be seen from the standard deviations of the points, the laser tracer positions and the dead paths.

Distances are comparable between the methods, as both methods determine coordinates in the Euclidean space, and reveal the differences between said methods. The distances between the determined point coordinate and the determined laser tracer positions were used, so there were four distances per CCR point coordinate to compare. The differences between these distances when comparing the two methods are depicted in figure 6.9b. A clear separation into two sections is visible. The first section ranges up to point no 500, which is exactly the points of the initialization cube. Whereas the second section, ranges from point no 501 until the end which are the points of the trajectory. Within these two sections there is only a clear offset between the distances of the different methods. The clear offset of the distances can also be interpreted as being an additional offset to the dead path. The additional offsets fit comfortably into the appropriate standard deviation of the dead paths of the standard analysis method, which is shown in table 6.3. This is a further sign that the systematic deviations in figure 6.5a should not be thought to be caused by the laser tracker, as, with a little adjustment on the dead paths of the laser tracer, the systematic deviations vanish.

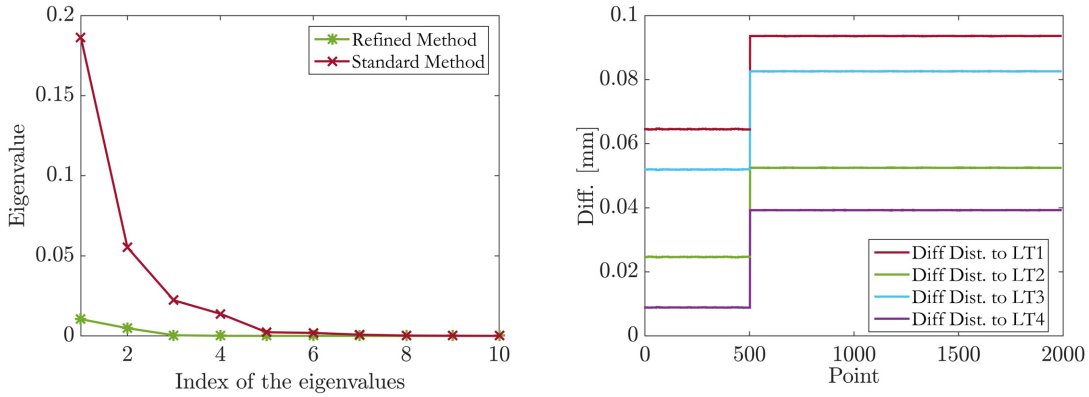

(a) Eigenvalue Spectrum of the standard analysis method and the refined analysis method. Showing the 10 biggest eigenvalues.

(b) Comparison between the distances from a laser tracer to a point on the trajectory determined with the standard method and the refined method.

Figure 6.9: Comparison of the Analysis Methods

Laser Tracer	Section 1		Section 2	
	Offset [µm]	Dead path STD [µm]	Offset [µm]	Dead path STD [µm]
1	65	99	94	104
2	25	78	53	84
3	52	75	83	82
4	9	40	39	48

Table 6.3: Dead path standard deviation (STD) of the standard analysis method confronted with the additional offset.

Kinematic Laser Tracker Measurement Model Verification

The multilateration system and the laser tracker were synchronized using a trigger impulse generated by the industrial robot. Figure 6.10b shows the initialization cube of the multilateration system, as well as one of the trajectories. Another trajectory, which was used to verify the laser tracker measurement model, can be seen in figure 6.10a. These trajectories were chosen due to the inconstant speed changes on each axis to reveal kinematic issues within the laser tracker measurements. Their speed profiles at 100 mm/s can be seen in figure 6.11, where the profile of 6.11b belongs to the ellipse shape and 6.11a belongs to the loop shape. Due to various control constrains of the robot's axis and also the laser tracers, the fastest speed achieved along the trajectories was 200 mm/s.

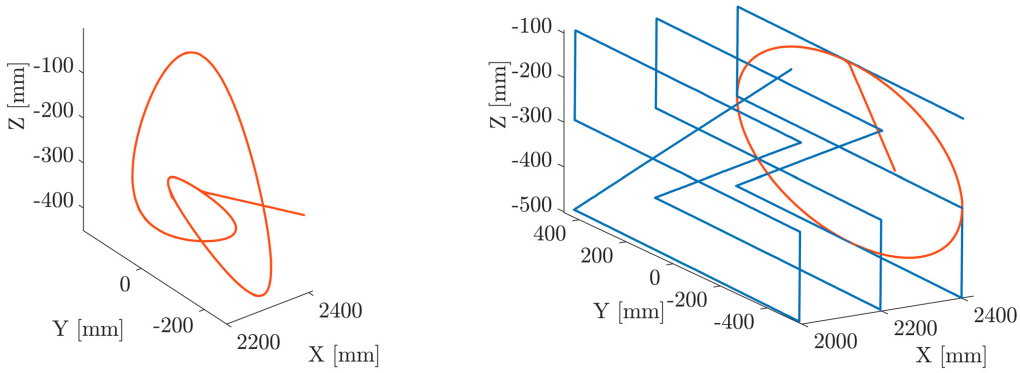

(a) Trajectory loop shape

(b) Trajectory ellipse shape depicted in orange together with the initialization cube depicted in blue.

Figure 6.10: Trajectory shapes

Trajectory	1	2	3	4
Shape	Loop	Loop	Ellipse	Ellipse
Speed [mm/s]	100	200	100	200

Table 6.4: Trajectories overview

As presented above in this section, the standard multilateration analysis method cannot be used with this experiment set-up, therefore the refined method was used to determine the multilateration points.

In order to efficiently solve the equation system in (5.7), direct solving methods for sparse matrix had to be used, as proposed in Schmitt [1973] for geodetic networks or for general problems in Davis [2006]. The maximal dimension was roughly $8 \cdot 10^5 \times 8 \cdot 10^5$ which also includes the observations of the initialization cube at the beginning of the experiment, not only the points of the trajectory. This matrix had a density of roughly 43 ppm, which is the fraction of non-zero elements over the number of elements of the matrix. As the inverse matrix of a sparse matrix is a full matrix, the posterior covariance matrix cannot be calculated entirely. Because this would require a memory of roughly 512 TB, encoding each entry as a double data type just to store the matrix. However, the diagonal entries of the matrix $\boldsymbol{N}^{-1}$, the inverse matrix of equation system in (5.7), can be determined, as Duff et al. [1986] and Erisman and Tinney [1975] showed in general for sparse matrices. In particular, these elements are needed to calculate a 3D point standard deviation of the multilateration points.

Because the initialization cube was not carried out before each experiment, an adjustment with a partial trace minimization was performed, using only the trajectory points as

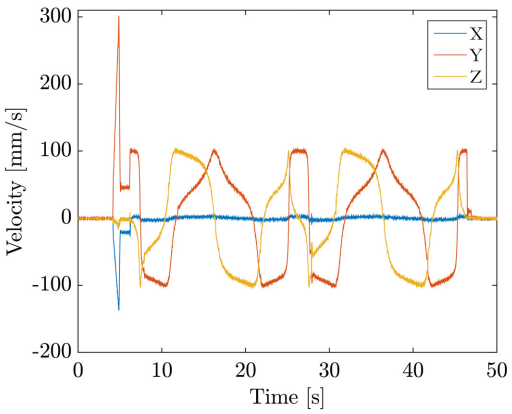

(a) Speed profile of the loop trajectory.

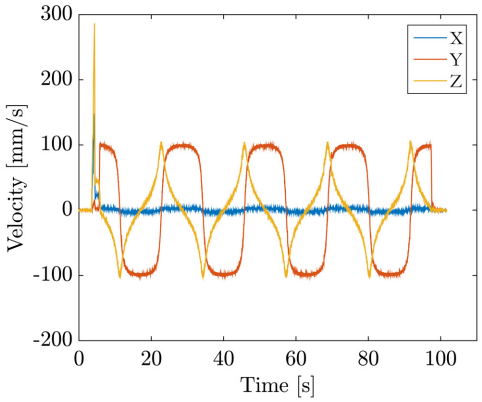

(b) Speed profile of the ellipse trajectory.

Figure 6.11: Speed profiles of the trajectories.

datum points as proposed above in this section. This was to ensure that the initial cube measurement did not influence the covariances of new points in the trajectory adjustment.

The results of the loop trajectory at a speed of 100 mm/s and 200 mm/s are displayed in figure 6.12, using the laser tracker coordinate system.

As the experiments needed to be stopped manually and the robot needed to move to its starting point within the first trajectory, the resulting total point number is not exactly twice as much as within the second trajectory. According to the results of the refined multilateration method the standard deviations never exceeded 2 µm along these trajectories. The laser tracker's standard deviation was estimated using the proposed measurement model, as presented in section 4.1, with respect to the velocity of the object which was derived from the ground truth. When taking into account figure 6.12a and 6.12d it can be seen that the standard deviation of the laser tracker data does not vary significantly. However, within figure 6.12a a slight range dependency is visible in the segment where the robot moves from its starting position to the starting position on the trajectory. Furthermore, in figure 6.12b and 6.12e there is only a negligible small noise increase visible and systematic deviations cannot be found within figure 6.12b nor within 6.12e. Therefore, no additional kinematic effects can be assumed at these speeds. The deviation of each point between the laser tracker and the multilateration system can be seen in figure 6.12c and 6.12f together with the point standard deviation of the laser tracker. Within these figures, the point deviation exceeded the laser tracker's standard deviation in 1.9 % of all points within the first trajectory and in 2.5 % of all points within the second trajectory. Accordingly, no influence factor of the laser tracker measurement model, as described in section 4.1, was underestimated for these two experiments. For both experiments the deviations of the X axis component is significantly smaller than

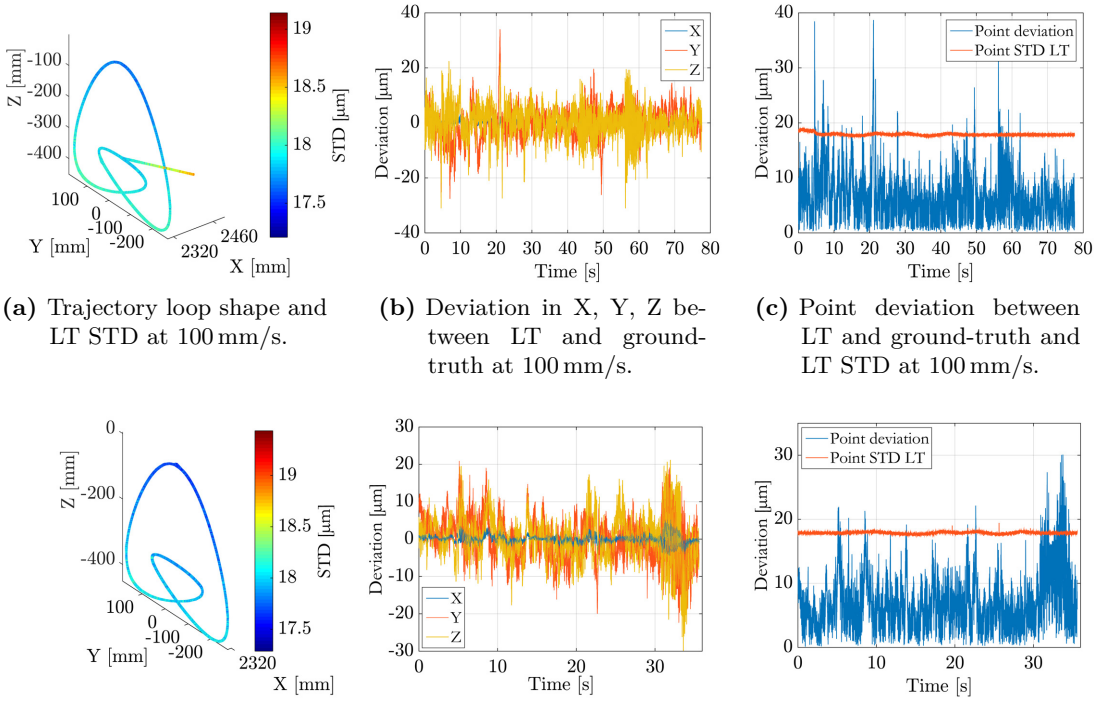

(a) Trajectory loop shape and LT STD at 100 mm/s.

(b) Deviation in X, Y, Z between LT and ground-truth at 100 mm/s.

(c) Point deviation between LT and ground-truth and LT STD at 100 mm/s.

(d) Trajectory loop shape and LT STD at 200 mm/s.

(e) Deviation in X, Y, Z between LT and ground-truth at 200 mm/s.

(f) Point deviation between LT and ground-truth and LT STD at 200 mm/s.

Figure 6.12: The loop trajectory at a speed of 100 mm/s in the first row and at 200 mm/s in the second row. The standard deviation (STD) was calculated using the proposed laser tracker (LT) model. Within figure (b) and (e) the X axis component is obscured by the other, larger components.

the deviations of the other two components. This is caused by the influence of any angle measurement, which is very low, compared with the part of the interferometer measurement, which has a much smaller uncertainty compared to the angle measurement, as described in 5.1.

The results of the ellipse trajectory at a speed of 100 mm/s as well as at a speed of 200 mm/s are displayed in figure 6.13. Owing to the reasons mentioned above, the total point number of the 100 mm/s experiment is not twice as much as the total point number of the 200 mm/s. The refined multilateration analysis method was used to determine the ground truth and the standard deviation never exceeded 2.2 µm. The standard deviation of the laser tracker was calculated, as mentioned previously, and is depicted within the laser tracker coordinate system in figure 6.13. In comparison with figure 6.13d a slight range dependency is visible in figure 6.13a. In spite of this, there is no significant increase in the standard deviation visible in figure 6.13d which might be caused by the higher object speed. Furthermore, there is no systematic deviation visible between the laser

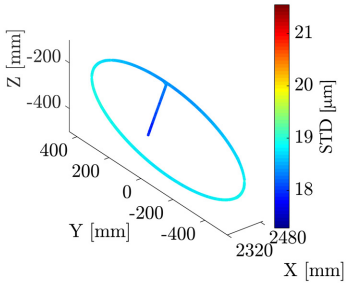

(a) Trajectory shape and LT STD at 100 mm/s.

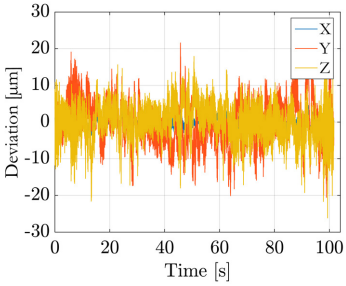

(b) Deviation in X, Y, Z between LT and ground-truth at 100 mm/s.

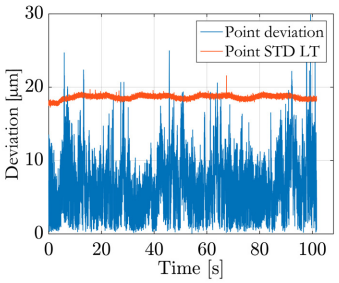

(c) Point deviation between LT and ground-truth and LT STD at 100 mm/s.

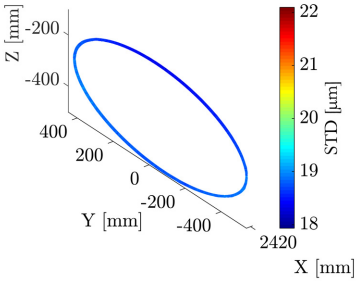

(d) Trajectory shape and LT STD at 200 mm/s.

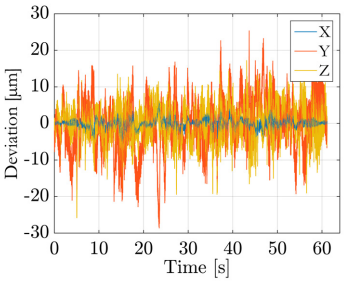

(e) Deviation in X, Y, Z between LT and ground-truth at 200 mm/s.

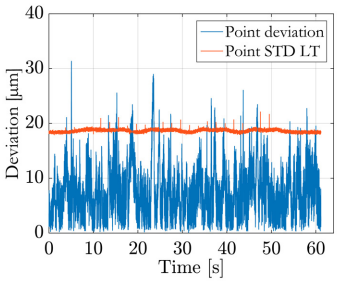

(f) Point deviation between LT and ground-truth and LT STD at 200 mm/s.

Figure 6.13: The ellipse trajectory at a speed of 100 mm/s in the first row and at 200 mm/s in the second row. The standard deviation (STD) was calculated using the proposed laser tracker (LT) model. Within figure (b) and (e) the X axis component is obscured by the other, larger components.

tracker and the multilateration system when taking into account figures 6.13b and 6.13e. However, there is a small increase in the noise level visible within the experiment which was conducted at a higher speed. Figures 6.13c and 6.13f show the point deviation between the laser tracker and the multilateration system as well as the point standard deviation of the laser tracker. Only in 0.6 % of all measurements the point deviation exceeded the point standard deviation of the laser tracker measurements in the third experiment and in the fourth experiment in 2 % of all experiments. This again shows that some influencing factors had been overestimated for the measurement model of the laser tracker, as introduced in section 4.1. The deviations of the X axis component is again significantly smaller than the deviations of the other two components. This is for the same reason as stated above for the other experiment.

To sum up, no significant variation was found when comparing the loop experiments with those of the ellipse, even when using different speed profiles along the trajectories.

6.4 Glass Scale / Linear Rail

To test the probabilistic measurement model of a Leica laser tracker, derived in 4.1, kinematic experiments were conducted using the developed kinematic ground truth, as described in 5.2, in conjunction with a Leica laser tracker AT901. The laser tracker was placed at difference positions and the motion profiles s-ramp, $\sin^2$-velocity profile and the septic polynomial profile were applied. All of the these profiles were used to move the object at different velocities, ranging from 0.23 m/s to 5.1 m/s. Before the kinematic measurements of the laser tracker can be conducted, the linear rail and glass scale also need to be checked in order to make sure that the entire object can be regarded as establishing a ground truth for kinematic laser tracker measurements. This means the uncertainty must be sufficiently low.

Glass Scale / Linear Rail Ground Truth Verification

Before the linear rail can be used in kinematic laser tracker experiments, the sub parts must be verified and the entire uncertainty budget must be determined, in order to make sure that the measurement set-up can be considered to be a kinematic ground truth.

Eigenfrequency and Additional Movement

As mentioned in section 5.2, it is important to know, if the entire reference object makes an additional movement, due to the force applied to move the carriage along the linear rail. This movement can be monitored by using another glass scale as described in the section stated.

Figure 6.14a shows, as an example, the additional movement of the granite block during a run of the septic polynomial motion profile. Beside an additional movement which is proportional to the acceleration profile, a high frequent oscillation is visible. As figure 6.14b illustrates, this high frequent oscillation is at a frequency of roughly 21.5 Hz. This frequency roughly matches the eigenfrequency which can be calculated using

$$f_0 = \frac{\sqrt{\frac{c_S}{m_O}}}{2\,\pi} \tag{6.9}$$

as can be found in Tipler and Mosca [2006]. Here, m_O is the mass of the entire object and can be estimated to 1500 kg and the spring constant is given by c_S. The spring constant can be determined by c_S = force/distance according to Tipler and Mosca [2006]. For this experiment the spring constant was determined to be $c_S = \frac{100\,\mathrm{N}}{3.6\,\mu\mathrm{m}}$. Accordingly, the resulting eigenfrequency is 21.7 Hz. The slight deviation might be caused by the rather inaccurate spring balance to measure the 100 N used to determine the spring constant or the rather rough estimate of the mass of the entire object.

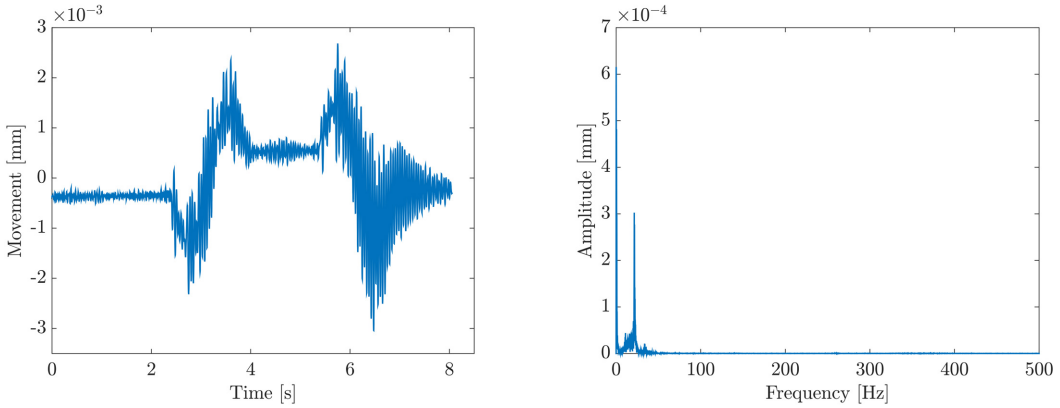

(a) Additional movement due to the applied forces to move the carriage along the linear rail.

(b) Frequency analysis of the entire object, granite block together with the metal support frame.

Figure 6.14: Additional movement of the granite block together with the metal support frame.

In order to reduce the additional movement of the granite block, two short vertical metal posts were installed, at either short side of the granite block. Figure 6.17b shows the granite block together with the two posts. Each of the posts is equipped with a horizontal screw in conjunction with a levelling pad, so that the granite block can be pre-stressed in both movement direction, thereby reducing the additional movement. Furthermore, due to the pre-stressing the spring constant changes and the rigidity of the entire object increases.

The additional movement can be further reduced by decreasing the force which is applied to the granite block. This could be done by uncoupling the motor from the granite block, this means using an additional metal frame exclusive for mounting the motor and the deflection pulley of the timing belt as well. This option would reduce a major part of the applied force on to the granite block and therefore also the additional movement. The remaining force would be the friction of the carriage on the rail which is roughly 20 N but cannot be further reduced.

However, the additional movement needs to be carefully monitored and taken into account when comparing the laser tracker distances against the glass scale readings. As described in detail in section 5.2, this additional movement can be monitored synchronously using the two axis glass scale. This two axis glass scale has a position error of ±270 nm over 1.5 m as reported in the calibration sheet.

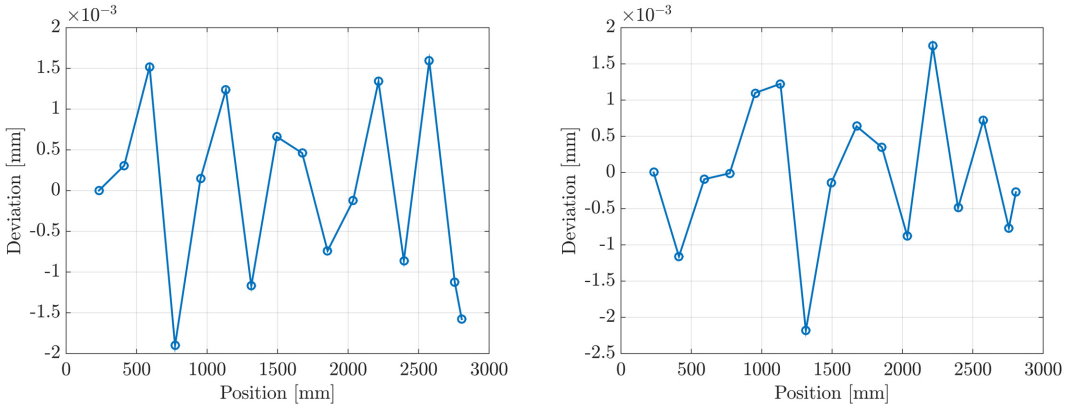

(a) Deviation at the beginning.

(b) Deviation roughly 6 h later, while the temperature has changed 0.2 °C

Figure 6.15: Deviation between the distance calculated between two laser tracker points and two glass scale readings, due to the non-straightness in conjunction with the laser tracker's retro-reflector offset.

Non-straightness

As mentioned in section 5.2, the straightness of the linear rail must be determined, in order to derive the resulting error, when comparing the distance between two positions measured using the glass scale and using the laser tracker measurements. Beside the straightness, the offset between the retro-reflector's optical centre and the reading head of the glass scale are also needed. For the following analysis, this offset was assumed to be $(5, 5, 60)$ mm with respect to a local coordinate system which is placed in the origin of the reading head and having the axis oriented parallel to the coordinate system introduced in section 5.2. Due to physical restriction, this offset cannot be precisely measured, this is why a worst case estimate was chosen.

The straightness was measured using an auto-collimator having an error of $\pm 0.01''$ at a distance of 0.1 m, in accordance with the calibration sheet. By using these auto-collimator measurements, the deviations between the distances calculated between two laser tracker points and the two glass scale readings along the linear rail, can be determined applying (5.18). The distance between the cumulative positions were chosen to be the carriage length, as proposed in Weck [2013]. Figure 6.15b shows the result at the end, after conducting the kinematic laser tracker measurements which took roughly 6 h, and the deviations are in a range of $\pm 2.2\,\mu$m. At the end of the experiments there was an air temperature of 20.7 °C. The deviation at the beginning of the experiments can be seen in figure 6.15a when there was an air temperature of 20.5 °C. As the straightness is sensitive to temperature changes, the difference between the deviation at the beginning and 6 h later could be reduced, if there was a better climate control within the laboratory.

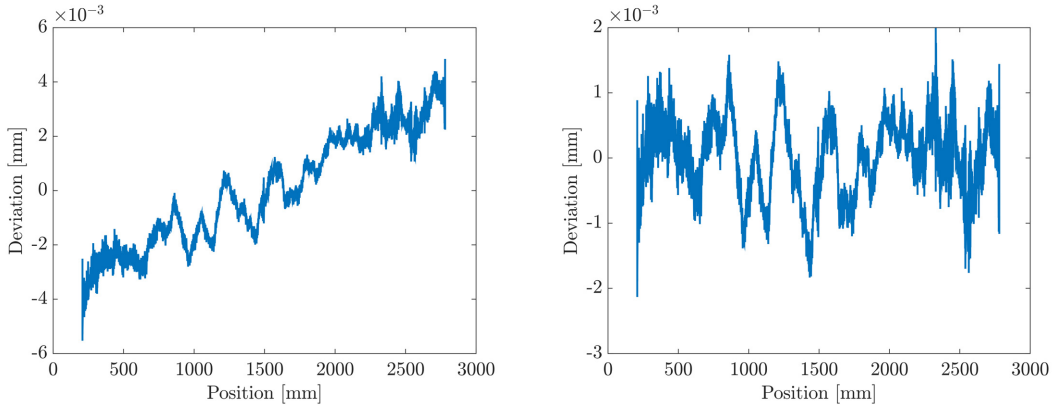

(a) Uncorrected deviation between the glass scale and two axis glass scale.

(b) Corrected deviation between the glass scale and two axis glass scale.

Figure 6.16: Verification of the glass scale.

Because the reading head of the glass scale is also attached to the carriage, the readings are consequently effected by the non-straightness of the linear rail, as described in section 5.2. By using the equation (5.19) the resulting deviation can be calculated to be 0.029 µm a maximum.

Glass Scale

In order to test if the glass scale is parallel to the moving axis and to verify its accuracy a two axis glass scale was used which was also used to monitor the additional movement during kinematic experiments, as mentioned at the beginning of this subsection.

Figure 6.16a shows the uncorrected deviations between the glass scale and the two axis glass scale where a linear trend is visible, which could be the result of non-parallel axis. The deviations compensated for the non-parallelism are illustrated in figure 6.16b and the remaining deviation is roughly ±2.1 µm. Additionally, the glass scale is effected by temperature changes and according to the manufacturer the coefficient of linear expansion is $0 \pm 0.5 \cdot 10^{-6}$ /°C.

All of these influences are summarized in table 6.5. This table can also be used to calculate an overall uncertainty for the glass scale / linear rail ground truth as proposed in Pesch [2003], which is in accordance with GUM. The final uncertainty can be determined as being 4 µm.

Within this table, the maximum additional movement which occurred during all kinematic experiments, is taken into account. This is why the final budget can be considered to be a worst case estimate of the experiments. These experiments are described in more detail in the following subsection. As the measurements can be compensated for any additional

	Range [µm]	Distribution	Factor	
Glass Scale	2.1	rect.	0.58	1.2 µm
Non-straightness	2.2	rect.	0.58	1.3 µm
Transversal Movement	2	rect.	0.58	1.2 µm
Linear expansion	0.1	rect.	0.58	0.1 µm
Skewed Reading	0.029	rect.	0.58	0.0 µm
			k=2	4 µm

Table 6.5: Uncertainty of the glass scale and linear rail ground truth

movement within the movement direction, only the additional transversal movement is considered in table 6.5.

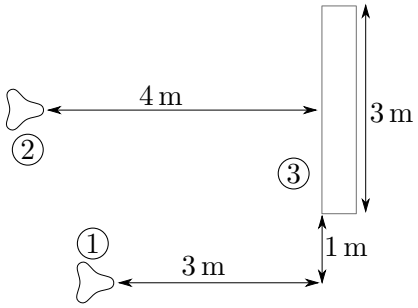

(a) Experiment set-up, laser tracker positions ① and ② around the granite block ③.

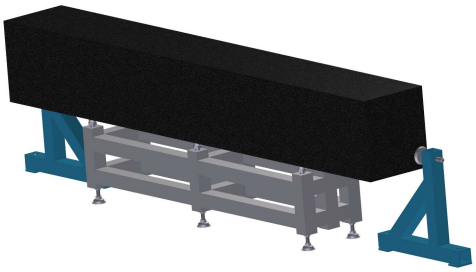

(b) Granite block with metal support frame and the two vertical metal posts.

Figure 6.17: Verification of the glass scale.

Kinematic Laser Tracker Measurement Model Verification

The kinematic experiments to verify the derived probabilistic model of the Leica laser tracker were conducted applying the different motions profiles, s-ramp, $\sin^2$-velocity profile and septic polynomial profile. All of these profiles are explained in section 5.2. These profiles were applied using different user parameters, meaning varying the velocity from slow to fast. Furthermore, the laser tracker was put in different places around the granite block to observe the movement along the linear rail. The configuration of the laser tracker positions and the granite block are illustrated in figure 6.17. One experiment consisted of a motion from one end to the other and after a short break the carriage moved back again to the starting position, while using the same motion profile for each movement. A representative bundle of the experiments, having a velocity ranging from 0.23 m/s to 5.1 m/s, will be discussed in detail in the following.

Unlike the experiments using the multilateration system, neither point coordinates can be compared nor can their uncertainty. Therefore, the proposed model of section 4.1, cannot be verified without further operations. This means, distances between retro-reflector positions along the linear rail had to be calculated as well as their uncertainties, incorporating the positions' uncertainties, determined using the prosed measurement model.

The distances along the rail were calculated from the smallest value to all other positions of the retro-reflector. This means that, the very left position, with respect to position two in figure 6.18, was held fixed while the distance to all the other positions were determined. Due to the fact, that there was a small overshoot, when commanding the carriage to a position, it is most likely that the smallest value along the glass scale is rather at the end of an experiment.

With regard to the equation for calculating the standard deviation of a distance between two Cartesian points, which is

$$\sigma_S = \sqrt{\frac{\left(\sigma_{X\,1}^2 + \sigma_{X\,2}^2\right)\left(X_1 - X_2\right)^2 + \left(\sigma_{Y\,1}^2 + \sigma_{Y\,2}^2\right)\left(Y_1 - Y_2\right)^2 + \left(\sigma_{Z\,1}^2 + \sigma_{Z\,2}^2\right)\left(Z_1 - Z_2\right)^2}{\left(X_1 - X_2\right)^2 + \left(Y_1 - Y_2\right)^2 + \left(Z_1 - Z_2\right)^2}} \tag{6.10}$$

it becomes clear from the denominator why there is a point of discontinuity, if their variance of each coordinate axis is not equal. Here, the standard deviation for each coordinate axis is given by σ and the subscript indicates the axis as well as the point number. The point coordinate is given by $X\,Y\,Z$ in conjunction with a subscript for the point number. As the calculated uncertainties using the proposed measurement model do not have the same variance for each coordinate axis, a discontinuity is most likely.

In order to compare the kinematic measurement model against the manufacturer's approximation, the distance variances along the rail were also calculated using this approximation. According to Ulrich and Irgenfried [2014], the kinematic accuracy of a Leica AT901 can be estimated with (2–4) times less than the static accuracy, which is $\pm 7.5\,\mu\text{m} + 3\,\mu\text{m/m}$ [Leica Geosystems AG, 2009c]. Even if the velocity ranges up to 5.1 m/s the lower bound, factor 2, were only used for the following experiments. Using the manufacturer's approximation the variance cannot be decomposed for individual axis, so no discontinuity can be expected.

There are some restriction which must be taken into account when using the laser tracker. The target velocity perpendicular to laser beam should not exceed 4 m/s at a distance of 2.5 m and the acceleration should not be higher than 2 g.

To test the probabilistic model, the 2σ standard deviation was determined and is illustrated in the figure 6.18. Accordingly, 95.4 % of the deviations between the distances derived from laser tracker measurements and the glass scale readings must be smaller than the 2σ standard deviation. Before the laser tracker distances were compared with the glass scale distances, the distances were compensated for any additional movement in the motion direction, as described above.

In figure 6.18a and 6.18b the result of the motion profile s-ramp with a constant velocity at 0.23 m/s are shown. In the first column, the laser tracker was placed at position 1 and in the second column the laser tracker was placed at position 2. Here, the 2σ standard deviation applying the measurement model is illustrated in red and the standard deviation applying the manufacturer's approximation is shown in yellow. A slight range dependency is visible which can also be expected due to the definition. However, the standard deviation using the measurement model is significantly lower, although it still comfortably includes the deviation between the laser tracker distances and the glass scale distances illustrated in green. The mean standard deviation at the laser tracker position 1 using the manufacturer's approximation is 74 µm, where the mean standard deviation using the measurement model is 38 µm, this is 49 % less. A similar situation can be seen

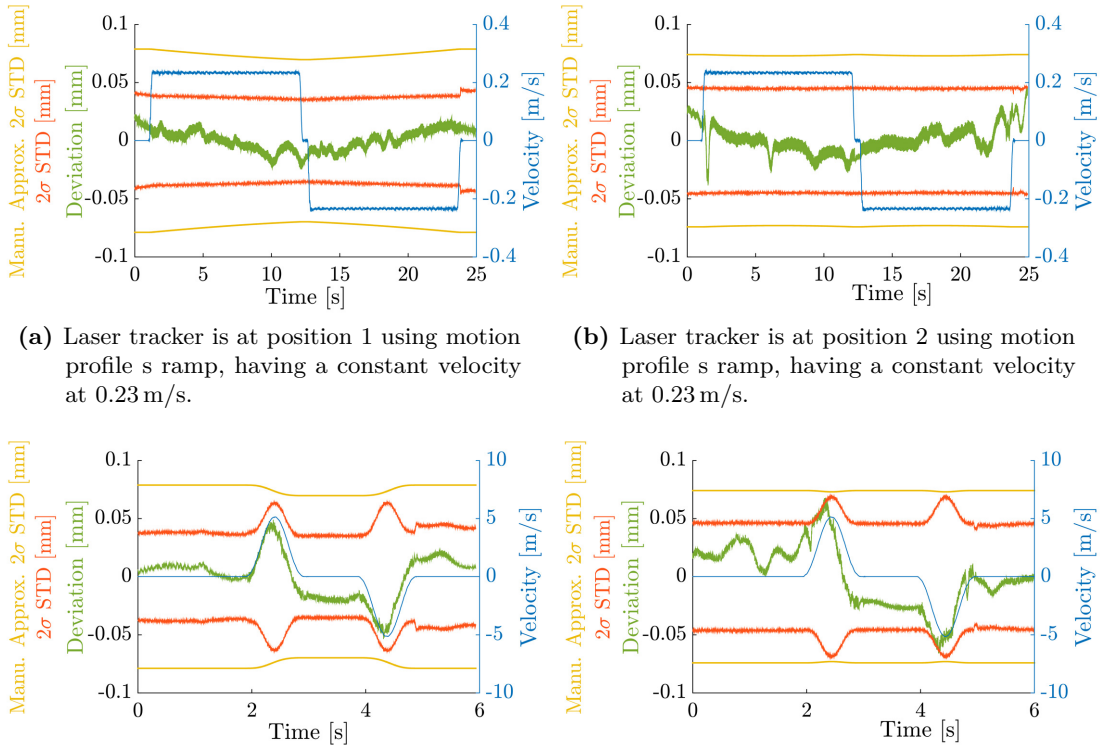

(a) Laser tracker is at position 1 using motion profile s ramp, having a constant velocity at 0.23 m/s.

(b) Laser tracker is at position 2 using motion profile s ramp, having a constant velocity at 0.23 m/s.

(c) Laser tracker is at position 1 using motion profile septic polynomial, having a maximum velocity at 5.1 m/s.

(d) Laser tracker is at position 2 using motion profile septic polynomial, having a maximum velocity at 5.1 m/s.

Figure 6.18: The results of the experiments using a s-ramp motion profile in the first row and a septic polynomial motion profile in the second row, while the laser tracker is at position 1 and 3.

at position 2, however the standard deviation using the measurement model is only 39 % less.

Figure 6.18c and 6.18d show the results of the septic polynomial motion profile, having a maximum velocity at 5.1 m/s. As can be seen, the standard deviation using the measurement model still includes the most deviations, but at position 2 1.4 % of measurements not. However, 1.4 % still obeys to the 2σ standard deviation.

Furthermore, there is a kinematic effect visible, which is not covered by geometric influences. But it is in a first order approximation proportional to the velocity of the object. It can also be seen that this effect is represented in the standard deviation using the measurement model. Additionally, the deviation is no longer proportional to the velocity, when the object is decelerating from a high velocity, especially during fast experiments. During this state the deviation decreases at a higher rate than expected, which leads to an overestimation.

When taking into account the standard deviation of the manufacturer's approximation, it becomes clear that, it is not sufficient to consider the true kinematic behaviour of the object being tracked. This can also be deduced from the fact that it is only range dependent, however particularly in figure 6.18c it can be seen that this leads to false assumptions, where the standard deviation decreases, it should increase to reflect the truth. The same behaviour can be found in the results at position 3 in figure 6.18d, but much weaker, there are two small dents visible near time 2 s and 4 s within the graph.

With regard to the results of position 1 compared to the results of position 2 it can be seen that the deviation varies more at station 2. The angle measurement part at position 2 may provide a plausible explanation, as it is significantly higher and therefore increases the uncertainty. It is comparable to the results of the multilateration measurements in section 6.3. However, in figure 6.18c and 6.18d it can be seen that this fact is considered within the standard deviation using the measurement model, as the standard deviation is higher in 6.18d for the same stable point at the beginning than it is in 6.18c.

To sum up, during all of the experiments, not only those presented here, the measurement model could be verified, if the kinematic conditions of the laser tracker, as mentioned above, were fulfilled.

Chapter 7

Conclusion

Within large volume metrology, laser trackers have been widely used to measure kinematic tasks such as the movement of an industrial robot and the tracking of a hand-held surface scanner. Notwithstanding these kinematic applications, most research has solely focused on the uncertainty of static measurements. Accordingly, only very rough estimates have been available, concerning the kinematic uncertainty.

With regard to potential applications, an approach capable of real-time was developed to determine uncertainties of kinematic measurements. It was shown that these uncertainties can be estimated in accordance to GUM using a Bayesian filter. As the kinematic behaviour of the object plays an important role, the system model description must be chosen with regard to the application and its requirements. Therefore, these descriptions can range from a very high approximation level to a very low approximation level, where additional information from the control system of moving object are integrated. To determine the uncertainty for simple movement, a common linear Kalman filter can be applied. However, if there is a complex movement a hybrid system model filter can be used to include more than one system model description as it is done for example by a Kalman filter. The internal models of a hybrid system filter must roughly match the observed process. This is why the choice of the system model within a hybrid system filter might be a difficult one, due to the low uncertainty achievable using LVM instruments. Aside from that a Bayesian filter can also be utilized to include additional information e.g. from a control system of an industrial robot. In this way all issues arising from the approximation of the movement can be mitigated.

In addition to the system model, there is the measurement model, which is also needed within a Bayesian filter. The measurement model was developed by augmenting the geometric model with a kinematic part as well as a meteorological part to entirely represent the measurement. As this model is state dependent, meaning it depends on

the object's current position and current kinematic, e.g. the velocity, it needs to be recalculated each time step.

To verify the derived probabilistic measurement model two new different kinds of kinematic ground truth were introduced. This is because prior methods have focused on the internal synchronization of the subsystems of a laser tracker i.e. the angle encoders and the distance measurement rather than on the object's trajectory.

The first one was made up of the PTB's multilateration system. Due to the restricted space and the acceptance angle, the standard analysis method was prone to error, which could be revealed using weak network analysis. Therefore, the analysis method was refined, so that the multilateration system provided a ground truth for kinematic laser tracker measurements. This was accomplished by introducing a new requirement matrix into the free-network adjustment, so that the geometry could be strengthened in general. This new requirement matrix can also be applied to any other free-network adjustment, where the standard approaches for strengthening the geometry cannot be applied. However, only a very small part of the laser tracker's capacity in terms of the velocity and acceleration could be tested. In general it can be said that the weak form analysis should always be part of a multilateration analysis to properly assess the deformation between the reference system and the machine being tested.

The second one consisted of a linear rail in conjunction with a glass scale. This is why no arbitrary trajectories can be chosen in contrast when using the multilateration system, however different motion profiles can be applied. The result is that the derived probabilistic model could be verified up to a maximum velocity of roughly 5 m/s using the linear rail and up to a maximum velocity at roughly 200 mm/s using the multilateration system. Furthermore, if the delay time is relatively short and the movement is rather slow, the results reveal that the alignment errors and the environmental conditions are more important than additional kinematic influences. As mentioned above, the uncertainty is state dependent and this is why it is hard to give a rule of thumb for which velocity or acceleration the kinematic influences play a significant role within the uncertainty of laser tracker measurements. However, overall it can be said that the proposed method in conjunction with the augmented measurement model reduced the uncertainty of the trajectory significantly and delivers a much more authentic uncertainty representation than the manufacturer's approximation, mainly due to the inclusion of the object's kinematic behaviour.

The proposed method can be applied to assess the deviation of a robot's trajectory in a reliable way in real-time and so has the potential to be used for correcting robots during their movement. Furthermore, it can be distinguished between points along the trajectory where the laser tracker measurement provides a useful contribution and points where not. Beside the real-time correction, the method could be also applied for real-time monitoring applications.

In order to grant the robot's information more reliability in this proposed method, its uncertainty must be reduced. A certain level could be reduced by implementing a more

authentic probabilistic model. But this requires a deeper insight to take into account the six axis industrial robot's dynamic model, consisting of the friction force, gravity loading, the joint-space inertia as well as the Coriolis and centripetal effects. However, particularly when observing robot's having a parallel kinematic, the proposed method should lead to a significant improvement in terms of assessing path deviations: As these kinds of robots may have a significantly better accuracy than six axis industrial robots, e.g. small hexapods, it is even more important to have an authentic uncertainty of the laser tracker trajectory to make an assessment of the path deviation.

Future work at the linear rail and glass scale ground truth should focus on minimizing the additional movement and eigenfrequency which occur during several high speed experiments. As these effects are related to the applied external force, it is clear that this must be reduced. The reduction could be achieved by uncoupling the motor from the granite block, this means using an additional metal frame exclusive for mounting the motor and the deflection pulley of the timing belt as well.

Even if the linear rail and glass scale ground truth has only one moving axis, six degrees of freedom (6DoF) equipment for laser trackers could be also tested by comparing the 3D distance in the same way as proposed for a 3D point. Furthermore, free-from surface scanning is either be done by moving a retro-reflector over the surface or by moving a line scanner over the surface. However, both methods there are meander movements with characteristic acceleration and deceleration parts in it, which could be adapted to create appropriate motion profiles. In order to identify whether or not there are some specific uncertainties which are originated just by the movement method. As the measurement model presented only includes 3D point measurements, this model should be augmented to include also the additional sensors, which are used during 6DoF measurements.

Bibliography

Holm Altenbach. *Kontinuumsmechanik : Einführung in die materialunabhängigen und materialabhängigen Gleichungen*. Springer, Berlin, Heidelberg, 2. aufl. 2012 edition, 2012. ISBN 978-3-642-24119-2.

Matthias Althoff. *Reachability Analysis and its Application to the Safety Assessment of Autonomous Cars*. PhD thesis, Technische Universität München, 2010.

API Automated Precision Inc. *API PRODUCT SPECIFICATIONS RADIAN*. API Automated Precision Inc., 2011.

API Automated Precision Inc. *OMINTRAC2*. API Automated Precision Inc., 2013.

ASME B89.4.19. Performance evaluation of laser-based spherical coordinate measurement systems. Standard, The American Society of Mechanical Engineers, 2006.

Herbert Balke. *Einführung in die Technische Mechanik : Festigkeitslehre*. Springer-Lehrbuch. Springer Vieweg, Berlin, Heidelberg, 3., aktualisierte aufl. 2014 edition, 2014. ISBN 978-364-24098-1-3.

Yaakov Bar-Shalom, X. Rong Li, and Thiagalingam Kirubarajan. *Estimation with Applications to Tracking and Navigation : [Theory, Algorithms and Software]*. A Wiley-Interscience publication. Wiley, New York, 2001. ISBN 0-471-41655-X.

G.J. Bierman. *Factorization Methods for Discrete Sequential Estimation*. Dover Books on Mathematics Series. Dover Publications, 2006.

K P Birch and M J Downs. Correction to the Updated Edlén Equation for the Refractive Index of Air. *Metrologia*, 31(4):315, 1994. URL `http://stacks.iop.org/0026-1394/31/i=4/a=006`.

Samuel Blackman and Robert Popoli. *Design and Analysis of Modern Tracking Systems*. Artech House radar library. Artech House, Boston [u.a.], 1999. ISBN 1-58053-006-0 ; 978-1-58053-006-4. Includes bibliographical references and index.

Fritz K. Brunner. *Geodetic Refraction: Effects of Electromagnetic Wave Propagation Through the Atmosphere*, chapter Modelling of Atmospheric Effects on Terrestrial Geodetic Measurements, pages 143–162. Springer Berlin Heidelberg, Berlin, Heidelberg,

1984. ISBN 978-3-642-45583-4. doi: 10.1007/978-3-642-45583-4_7. URL http://dx.doi.org/10.1007/978-3-642-45583-4_7.

Huimin Chen, T. Kirubarajan, and Y. Bar-Shalom. Performance limits of track-to-track fusion versus centralized estimation: theory and application [sensor fusion]. *Aerospace and Electronic Systems, IEEE Transactions on*, 39(2):386 – 400, april 2003. ISSN 0018-9251.

Peter I. Corke. *Robotics, Vision and Control : Fundamental Algorithms in MATLAB*. Springer Tracts in Advanced Robotics ; 73. Springer, Berlin, 2011. ISBN 978-3-642-20143-1 ; 3-642-20143-1.

John J. Craig. *Introduction to robotics : mechanics and control*. Pearson/Prentice Hall, Upper Saddle River, NJ, 3. ed., internat. ed. edition, 2005. ISBN 0-13-123629-6 ; 0-201-54361-3.

P. J. Crothers, P. L. Freeman, I. Dressler, K. Nilsson, A. Robertsson, W. Zulauf, B. Felber, R. Loser, K. Siercks, and T. Brogardh. Characterization of the Tau Parallel Kinematic Machine for Aerospace application. *SAE International Journal of Aerospace*, 2(1): 205–213, 2010. doi: 10.4271/2009-01-3222. URL http://saeaero.saejournals.org/content/2/1/205.abstract.

Timothy A. Davis. *Direct Methods for Sparse Linear Systems*. Society for Industrial and Applied Mathematics, 2006. doi: 10.1137/1.9780898718881. URL http://epubs.siam.org/doi/abs/10.1137/1.9780898718881.

Fritz Deumlich. *Surveying instruments*. de Gruyter, Berlin, 1982. ISBN 3-11-007765-5.

Iain S. Duff, Albert M. Erisman, and John Ker Reid. *Direct Methods for Sparse Matrices*. Monographs on numerical analysis. Clarendon, Oxford, 1986. ISBN 0-19-853408-6.

EN ISO 9283. Industrieroboter Leistungskenngrößen und zugehörige Prüfmethoden. Norm, Verein Deutscher Ingenieure, 1998.

A. M. Erisman and W. F. Tinney. On computing certain elements of the inverse of a sparse matrix. *Commun. ACM*, 18(3):177–179, March 1975. ISSN 0001-0782. doi: 10.1145/360680.360704. URL http://doi.acm.org/10.1145/360680.360704.

Cornelia Eschelbach. Störanfälligkeit geodätischer Präzisionsmessungen durch lokale Temperaturschwankungen. In Fritz K. [Hrsg.] Brunner, editor, *Ingenieurvermessung 07 : Beiträge zum 15. Internationalen Ingenieurvermessungskurs Graz 2007*, Heidelberg, 2007. Wichmann. ISBN 978-3-87907-448-8; 3-87907-448-8.

FARO Technologies Inc. *Laser Tracker ION*. FARO Technologies Inc., 2010.

FARO Technologies Inc. *Laser Tracker Vantage Technische Spezifikationen*. FARO Technologies Inc., 2012.

Karl Foppe, Volker Schwieger, and Rudolf Staiger. Grundlagen kinematischer Mess- und Auswertetechniken. In *Kinematische Messmethoden Vermessung in Bewegung*, pages 3–18, 2004.

H. Gurocak. *Industrial Motion Control: Motor Selection, Drives, Controller Tuning, Applications*. Wiley, 2015. ISBN 9781118403204.

Maria Hennes. *Entwicklung eines Meßsystems zur Ermittlung von Turbulenzparametern der Atmosphäre für Anwendungen in der Geodäsie*. PhD thesis, Zugl.: Bonn, Univ., Diss., 1994, München, 1995.

Hexagon Metrology. *LEICA ABSOLUTE TRACKER AT960*. Hexagon Metrology, 2015.

Peter H. Huang. New equations for water vapor pressure in the temperature range -100 °C to 100 °C for use with the 1997 nist/asme steam tables. In *Papers and abstracts from the third international symposium on humidity and moisture*, pages 69–76, 1998.

Ben Hughes, Alistair Forbes, Andrew Lewis, Wenjuan Sun, Dan Veal, and Karim Nasr. Laser tracker error determination using a network measurement. *Measurement Science and Technology*, 22(4):045103, 2011.

I. Hwang, H. Balakrishnan, and C. Tomlin. State estimation for hybrid systems: applications to aircraft tracking. *Control Theory and Applications, IEE Proceedings* -, 153 (5):556–566, September 2006.

Ingrid Illner. *Datumsfestlegung in freien Netzen*. PhD thesis, Universität Karlsruhe (TH), München, 1985. Zugl.: Karlsruhe, Univ., Diss., 1984.

Hubert Kaltenbach. *Optimierung geodätischer Netze mit spektralen Zielfunktionen*. PhD thesis, Universität Karlsruhe (TH), München, 1992. Zugl.: Karlsruhe, Univ., Diss., 1992.

Henrik Kihlman, Raimund Loser, Andrew Cooke, Albin Sunnanbo, and Konrad Von Arb. Metrology-integrated Industrial Robots - Calibration, Implementation and Testing. In *Proceedings of the 35th International Symposium on Robotics (ISR)*, Paris, France, 2004. 35th ISR International Symposium on Robotics, 23-26 March, Paris, France.

KUKA. *KUKA KR 5 arc User Manual*. KUKA Robot Group, Augsburg Germany, ba kr 5 arc de edition, March 2011.

Leica Geosystems AG. *emScon 3.5 Programmers Manual Tracker Programming Interface*. Leica Geosystems AG, Leica Geosystems AG Metrology Division Mönchmattweg 5 5035 Unterentfelden Switzerland, 3.5 edition, August 2009a.

Leica Geosystems AG. *AbsoluteTracker*. Leica, Geosystems AG, Mönchmattweg 5 CH-5035 Unterentfelden (Switzerland), 2.0.0 edition, 2009b.

Leica Geosystems AG. *PCMM System Specifications Leica Absolute Tracker and Leica T-Products*. Leica, Geosystems AG, Mönchmattweg 5 CH-5035 Unterentfelden (Switzerland), 2009c.

X.R. Li and V.P. Jilkov. Survey of maneuvering target tracking. Part I. Dynamic models. *Aerospace and Electronic Systems, IEEE Transactions on*, 39(4):1333–1364, Oct 2003. ISSN 0018-9251. doi: 10.1109/TAES.2003.1261132.

Ignacio Lira and Wolfgang Wöger. Comparison between the conventional and bayesian approaches to evaluate measurement data. *Metrologia*, 43(4):S249, 2006. URL `http://stacks.iop.org/0026-1394/43/i=4/a=S12`.

Raimund Loser. *Weiterentwicklung eines absoluten, hochpräzisen und trackingfähigen Distanzmessers für industrielle Anwendungen*. Mitteilungen. Institut für Geodäsie und Photogrammetrie an der Eidgenössischen Technischen Hochschule Zürich. Inst. für Geodäsie und Photogrammetrie, 2001. ISBN 9783906467351.

Raimund Loser. Kinematische Messmethoden im industriellen Nahbereich. In *Kinematische Messmethoden Vermessung in Bewegung*, pages 233–243, 2004.

Raimund Loser and Stephen Kyle. Alignment and field check procedures for the Leica Laser Tracker LTD 500. In *Boeing Large Scale Optical Seminar*, Seattle, United States, 1998.

Thomas Luhmann, Stuart Robson, Stephen Kyle, and Jan Boehm. *Close-range Photogrammetry and 3D Imaging*. De Gruyter textbook. De Gruyter, 2013. ISBN 9783110302691.

Albert Markendorf. The influence of the tooling ball reflector on the accuracy of laser tracker measurements: Theory and practical tests. Technical report, Leica Geosystems AG, 2000.

Harvey B. Mitchell. *Multi-sensor Data Fusion: An Introduction*. Springer Verlag, Berlin, 2007. ISBN 978-3-540-71463-7.

Edward Morse and Victoria Welty. Evaluation of dynamic measurements with laser trackers. Coordinate Metrology Society Conference (CMSC), 2013.

Christian Munzinger, Jürgen Fleischer, and Gregor Stengel. Flying cutting of spatially curved extrusion profiles. In *Flexible Manufacture of Lightweight Frame Structures, 2006*, volume 10 of *Advanced Materials Research*, pages 35–42. Trans Tech Publications, 3 2006. doi: 10.4028/www.scientific.net/AMR.10.35.

B Muralikrishnan, D Sawyer, C Blackburn, S Phillips, B Borchardt, and W T Estler. ASME B89.4.19 Performance Evaluation Tests and Geometric Misalignments in Laser Trackers. *Journal Of Research Of The National Institute Of Standards And Technology*, 114(1):21–35, 2009.

National Physical Laboratory (NPL). Engineering precisely. Newsletter, Spring 2009.

B. T. Neyer. Velocity Interferometer System For Any Reflector (VISAR). *Proc. SPIE*, 0648:301–315, 1986. doi: 10.1117/12.964543. URL `http://dx.doi.org/10.1117/12.964543`.

Wolfgang Niemeier. *Ausgleichungsrechnung : statistische Auswertemethoden*. De Gruyter Lehrbuch. de Gruyter, Berlin [u.a.], 2., überarb. und erw. aufl. edition, 2008. ISBN 978-3-11-019055-7.

W. Pauli. Vorteile eines kippbaren Reflektors bei der elektrooptischen Streckenmessung. *Vermessungstechnik*, 11:412 – 415, 1969.

Jürgen Peipe. High Resolution Data Acquisition to Observe Moving Objects. In Karl Kraus and Peter Waldhäusl, editors, *Close Range Techniques and Machine Vision*, volume XVIII, pages 471–474. ISPRS, July 1996.

Bernd Pesch. *Bestimmung der Messunsicherheit nach GUM : Messunsicherheitseinflüsse, Messunsicherheitsanalyse und -budgets, Verteilungen, Sensitivitätskoeffizienten und Gewichtsfaktoren, Korrelation, Ergebnisse darstellen, Optimierungspotentiale, Beispiele, ausführliches Glossar*. Grundlagen der Metrologie. Norderstedt : Books on Demand, Norderstedt, 2003. ISBN 3-8330-1039-8.

Broschüre: PI Hexapoden. Physik Instrumente (PI) GmbH & Co. KG, Auf der Römerstr. 1 76228 Karlsruhe/Palmbach (Germany), 2012.

Branko Ristic, Sanjeev Arulampalam, and Neil Gordon. *Beyond the Kalman Filter : Particle Filters for Tracking Applications*. Artech House radar library. Artech House, Boston, Mass. [u.a.], 2004. ISBN 1-58053-631-X ; 978-1-58053-631-8.

X. Rong Li. Multiple-model estimation with variable structure: some theoretical considerations. In *Decision and Control, 1994., Proceedings of the 33rd IEEE Conference on*, volume 2, pages 1199–1204 vol.2, Dec 1994. doi: 10.1109/CDC.1994.411169.

X. Rong Li. Engineer's Guide to Variable-Structure Multiple-Model Estimation for Tracking. In Yaakov Bar-Shalom and W. D. Blair, editors, *Multitarget-Multisensor Tracking: Applications and Advances*, volume III, pages 499–567. Artech House, 2000.

X. Rong Li and Vesselin P. Jilkov. Survey of Maneuvering Target Tarcking, Part I: Dynamic Models. *IEEE Transactions On Aerospace And Electronic Systems*, 5428(4): 1333–1364, 2003.

X. Rong Li and Youmin Zhang. Multiple-model estimation with variable structure. v. likely-model set algorithm. *Aerospace and Electronic Systems, IEEE Transactions on*, 36(2):448–466, Apr 2000. ISSN 0018-9251. doi: 10.1109/7.845222.

Günter Schmitt. *Speichertechnische und numerische Probleme bei der Auflösung großer geodätischer Normalgleichungssysteme*. PhD thesis, Universität Karlsruhe (TH), 1973.

Günter Schmitt. Spectral Analysis and Optimization of two Dimensional Networks. *Geomatics Research Australasia*, 67:47–64, 1997.

Dan Simon. *Optimal state estimation : Kalman, H. [infinity] and nonlinear approaches*. Wiley-Interscience, Hoboken, NJ, 2006. ISBN 0-471-70858-5 ; 978-0-471-70858-2.

J. A. Sousa and A. Forbes. The gum, bayesian inference and forward and inverse uncertainty evaluation. In *2ª Conferência Nacional da SPMet - Metrologia e Inovação*, 2007.

Jack A. Stone and Jay H. Zimmerman. Index of refraction of air. http://emtoolbox.nist.gov/Wavelength/Documentation.asp, December 2011. URL `http://emtoolbox.nist.gov/Wavelength/Documentation.asp`.

THK Hauptkatalog. THK CO., LTD., HEAD OFFICE 3-11-6, NISHI-GOTANDA, SHINAGAWA-KU, TOKYO 141-8503 JAPAN, 2015a.

THK Caged Ball LM Guide. THK CO., LTD., HEAD OFFICE 3-11-6, NISHI-GOTANDA, SHINAGAWA-KU, TOKYO 141-8503 JAPAN, 2015b.

Sebastian Thrun, Wolfram Burgard, and Dieter Fox. *Probabilistic robotics*. Intelligent robotics and autonomous agents. MIT Press, Cambridge, Mass., 2005. ISBN 0-262-20162-3 ; 978-0-262-20162-9.

Paul Allen Tipler and Gene Mosca. *Physik für Wissenschaftler und Ingenieure*, volume [Hauptbd.]:. Spektrum Akad. Verl., Heidelberg, 2. dt. aufl., rev. nachdr. / hrsg. von dietrich pelte edition, 2006. ISBN 978-3-8274-1164-8; 3-8274-1164-5.

Thomas Ulrich. Uncertainty Estimation for Kinematic Laser Tracker Measurements. In *International Conference on Indoor Positioning and Indoor Navigation (IPIN), 2012 International Conference on*, pages 1 –10, November 2012. doi: 10.1109/IPIN.2012.6418910.

Thomas Ulrich. Uncertainty estimation and multi sensor fusion for kinematic laser tracker measurements. *Metrologia*, 50(4):307–317, 2013. URL `http://stacks.iop.org/0026-1394/50/i=4/a=307`.

Thomas Ulrich. Uncertainty modelling of real-time observation of a moving object: photogrammetric measurements. *Metrologia*, 52(2):201–213, 2015. URL `http://stacks.iop.org/0026-1394/52/i=2/a=201`.

Thomas Ulrich and Stephan Irgenfried. Uncertainty Estimation for Kinematic Laser Tracker Measurements Incorporating the Control Information of an Industrial Robot. In *International Conference on Indoor Positioning and Indoor Navigation (IPIN), 2014 International Conference on*, pages 68 –76, October 2014. doi: 10.1109/IPIN.2014.7275469.

VDI 2143. Bewegungsgesetze für Kurvengetriebe Theoretische Grundlagen (Motion rules for cam mechanisms Theoretical Fundamentals). VDI-Richtlinie, Verein Deutscher Ingenieure, 2002.

M. Weck. *Werkzeugmaschinen Fertigungssysteme: Messtechnische Untersuchung und Beurteilung*. VDI-Buch. Springer Berlin Heidelberg, 2013. ISBN 9783662109267.

Walter Welsch, Otto Heunecke, and Heiner Kuhlmann, editors. *Handbuch Ingenieurgeodäsie*, volume (ausw): Auswertung geodätischer Überwachungsmessungen. Wichmann, Heidelberg, 2000. ISBN 3-87907-295-7.

Ulrich Wiest. *Kinematische Kalibrierung von Industrierobotern*. PhD thesis, Universität Karlsruhe (TH), Aachen, 2001. Zugl.: Karlsruhe, Univ., Diss., 2001.

Lin Yongbing, Zhang Guoxiong, and Li Zhen. An improved cat's-eye retroreflector used in a laser tracking interferometer system. *Measurement Science and Technology*, 14 (6):N36, 2003. URL `http://stacks.iop.org/0957-0233/14/i=6/a=404`.

Duan Zhansheng and X. Rong Li. Optimal distributed estimation fusion with transformed data. In *Information Fusion, 2008 11th International Conference on*, pages 1 –7, Cologne, Germany, July 2008.

Walter Zuercher, Raimund Loser, and Stephen A. Kyle. Improved reflector for interferometric tracking in three dimensions. *Optical Engineering*, 34(9):2740–2743, 1995. doi: 10.1117/12.205679. URL `http://dx.doi.org/10.1117/12.205679`.

Acronyms and Abbreviations

6DoF six degrees of freedom.

ADM absolute distance meter.

CCR corner cube reflector.

GUM Guide to the Expression of Uncertainty in Measurement.

IAG International Association of Geodesy.

IFM interferometer.

IMM Interacting Multiple Model.

LMS likely-model set.

LVM large volume metrology.

PDF probability density function.

PSD position sensitive device.

PTB Physikalisch-Technische Bundesanstalt.

RMIMM Residual-Mean Interacting Multiple Model.

RSI Robot Sensor Interface.

TCP tool centre point.

UDP User Datagram Protocol.

VISAR velocity interferometer system for any reflector.

XML Extensible Markup Language.

Appendix A

Papers

Uncertainty modelling of real-time observation of a moving object: photogrammetric measurements

Thomas Ulrich

This is an author-created, un-copyedited version of an article accepted for publication in Metrologia. Neither the International Bureau of Weights and Measures nor IOP Publishing Ltd is responsible for any error or omissions in this version of the manuscript or any version derived from it. The version of Record is available online at http://stacks.iop.org/0026-1394/52/i=2/a=201.

Abstract

Photogrametric systems are widely used in the field of industrial metrology to measure kinematic tasks such as tracking robot movements. In order to assess spatiotemporal deviations of a kinematic movement, it is crucial to have a reliable uncertainty of the kinematic measurements. Common methods to evaluate the uncertainty in kinematic measurements include approximations specified by the manufactures, various analytical adjustment methods and Kalman filters.

Here a hybrid system estimator in conjunction with a kinematic measurement model is applied. This method can be applied to processes which include various types of kinematic behaviour, constant velocity, variable acceleration or variable turn rates. Additionally, it is been shown that the approach is in accordance with GUM (Guide to the Expression of Uncertainty in Measurement). The approach is compared to the Kalman filter using simulated data to achieve an overall error calculation. Furthermore, the new approach is used for the analysis of a rotating system as this system has both a constant and a variable turn rate.

As the new approach reduces overshoots it is more appropriate to analysing kinematic processes than the Kalman filter. In comparison with the manufacturer's approximations, the new approach takes account of kinematic behaviour, with an improved description of the real measurement process. Therefore, this approach is well-suited to the analysis of kinematic processes with unknown changes in kinematic behaviour.

Photogrammetric System; Kinematic measurement; Hybrid system estimator IMM; Uncertainty estimation; Bayesian filtering

1 Introduction

In recent years photogrammetric systems have been widely used for kinematic measurements. These have included crash tests, structure analysis and motion capture e.g. for movies or games. However, they can also be used in LVM (Large Volume Metrology) to measure the tool centre point of an industrial robot during its movement and can therefore be utilised for real time process monitoring or to provide online correction. It is particularly important to have a reliable uncertainty of the kinematic measurement for the last two tasks. This permits an explicit assessment of the deviations between the trajectory observed by the photogrammetric system and the one provided by the robot control system.

There are different analysis methods for different kinematic applications including time series analysis for pattern recognition suggested by [1]. The author of [2] suggests an adjustment method in a post-processing analysis step which was previously used by [3] in order to compare the kinematic performance of a stereo photogrammetric system against a Leica Laser Tracker. A Kalman filter was suggested by the author of [4] but with the limitation that the probabilistic system model of the kinematic process must be known and all error terms must have a Gaussian distribution. To overcome these limitations [5] applied a real-time hybrid system filter for kinematic laser tracker measurements. The approach proposed in this paper is also based on a hybrid filter. Here the focus on the system models describing the real kinematic process more precisely, as well as on the measurement model of a stereo photogrammetric system to include kinematic effects. Furthermore, it is

demonstrated that the hybrid system model is in accordance with GUM (Guide to the Expression of Uncertainty in Measurement).

1.1 Photogrammetric system

The photogrammetric system used in this experiment is the MoveInspect HF from AICON, which works with retro-reflective targets. A sketch of the system can be seen in figure 2. This system consists of two cameras which are mounted on a bar to facilitate a stable exterior calibration during the measurement. Exterior calibration describes the position and orientation of one camera relative to the other. In order to use the system, it must be calibrated before the measurement takes place. This procedure determines the exterior calibration parameters, as well as the interior calibration parameters. It describes the imaging process of a 3D point onto an image plane, including the distortion parameters of the lenses used. More details relating the calibration parameters to kinematic effects are discussed in section 4.4. The syncbox synchronizes both cameras and can be triggered using an external impulse e.g. generated by an industrial robot. Within the syncbox these two cameras are triggered in cascade. This results in an additional error source for kinematic measurements which is explained in more detail in 4.4. The photogrammetric system can capture images up to 1000 Hz. After capturing an image in grey values, the image processing is done on a FPGA (Field Programmable Gate Array) to achieve a high frequency in 2D image points in order to cope with fast kinematic movements of an object [6]. In this image processing, the edges of the retro-reflective targets are extracted using a Sobel operator from the grey value image resulting in regions of interest, details on the Sobel operator can be found in [7]. To calculate the 2D point coordinates of the imaged targets, the centroid method is applied to the selected regions of interest. This is a weighted mean of the pixel coordinates. Using these 2D point coordinates and the calibration parameters, the AICON software, running on an external laptop, calculates the corresponding 3D target coordinates.

2 Measurement Uncertainty

If the measurement result of a photogrammetric system is associated with a statement of uncertainty expressing the reliability of that result, then it is possible to make an explicit assessment of the spatiotemporal deviations between a planned trajectory and the one observed by the photogrammetric system. The *Guide to the Expression of Uncertainty in Measurement* (GUM) provides a framework, which is widely accepted, to evaluate uncertainties [8, 9].

Within GUM the uncertainty of a quantity ζ can be expressed as a probability density function (PDF) $p(\zeta)$. Uncertainty evaluation can, in general, be divided into two cases, the forward-uncertainty evaluation and the inverse-uncertainty evaluation [10].

To determine the uncertainty for multivariate input-output models, the forward-uncertainty evaluation can be utilized. Given a function of multiple variables, $\eta = f(\boldsymbol{\zeta})$, where $\boldsymbol{\zeta}$ is the vector of those variables, then the required PDF is $p(\eta)$. This uncertainty can be determined by applying the law of propagation of uncertainty (LPU) or using the Monte Carlo method (MCM). To apply these methods, all input quantities $\boldsymbol{\zeta}$ must be known, together with an associated probability distribution. The advantages of the MCM are that it does not use approximations in the distributions of the input or output quantities nor does it use linearization [8, 10].

The inverse uncertainty evaluation can be associated with model parameter fitting. Here, the desired parameter β is only indirectly, related to the measured quantities ζ by a function $f(\beta)$. To deduce a density of β, with respect to the observed information ζ the Bayesian paradigm can be utilized. This posterior density $p(\beta|\zeta)$ includes the information about parameter β of the function, based on the observed quantities ζ and any prior information [8]. For example, the inverse uncertainty evaluation can be applied to the uncertainty determination of the circle parameters radius and centre from photogrammetric measurements or laser tracker measurements, as these quantities cannot be measured directly. The posterior density $p(\beta|\zeta)$ can be determined using the Bayes theorem

$$p(\beta|\zeta) = \frac{p(\zeta|\beta)\, p(\beta)}{p(\zeta)}. \tag{1}$$

Here, $p(\zeta|\beta)$ is the likelihood function and $p(\beta)$ is the prior density. The prior density comprises of information about the parameter β available prior to the observations ζ, or from other independent sources. In general, the Markov-Chain-Monte-Carlo (MCMC) approach can be applied to determine the posterior density $p(\beta|\zeta)$. There are a number of algorithms for

the MCMC approach e.g. the Metropolis-Hastings independence chain algorithm. To make an inference about the parameter β, the posterior density can be used directly, as it represents the state of knowledge with respect to the observed measurement ζ [8].

According to [11], the Bayesian statistic is well-suited to determining a measurement uncertainty if systematic influences can be inferred, but cannot be directly measured. It is therefore preferable to conventional statistics for the analysis of kinematic uncertainties as e.g. the velocity causes a systematic effect which cannot be measured directly with a photogrammetric system. This is explained in more detail below. The difference between the conventional statistic and the Bayesian statistic with regard to GUM is presented in [11, 12].

2.1 Kinematic Measurement

As the authors of [1] pointed out, the term 'kinematic measurement' can be construed in different ways. However, in this paper the term kinematic measurement is regarded as the spatiotemporal measurement of a moving object, so the result can be related to other measurements through a common time axis as depicted in figure 1. There are a number of analysis methods for these kinds of measurements for different applications. However, these methods are often not capable of real-time calculation or the kinematic characteristic such as acceleration or velocity must be known exactly in advance [5].

The main focus of the proposed method is on the real-time observation and analysis of the moving object's trajectory. In order to achieve a higher flexibility, the trajectory should be assumed to be unknown in advance and arbitrary.

Normally, the observed measurements of a moving object must be transformed into the object space for purpose of analysis. In the case of a kinematic measurement, it is not only the spatial transformation which must be considered but also the alignment of the time axis, as these axes may have different zero points, scales or drifts. The relationship between the object space and the measurement space can be seen in figure 1. Here two time axes, for example one belonging to a robot and one to the measurement system, are aligned using a synchronization impulse. The common time axis can also be generated using a frequency counter. In figure 1, a point in time is denoted by t where the superscript indicates the number of the point and the subscript indicates m for the measurement space, o for the object space. No subscript is used for the common time axis. On each time axis k denotes the same specific interval, to highlight the possible differences between these axes. A rotation matrix R and translation vector T are used to define a geometric transformation. Assuming that the rotation and the translation between the object space and the measurement space are known, the kinematic measurement of an object moving along a straight line at a constant velocity can be expressed as follows

$$\boldsymbol{x} = \boldsymbol{z}\left(\boldsymbol{V}\right) + \boldsymbol{V} \cdot dt. \tag{2}$$

Here dt is the time offset between the time axes of the object and the measurement systems. The results of the vector function $\boldsymbol{z}$, with respect to the velocity $\boldsymbol{V}$, are the measurements. These have been already transformed into the object space using known spatial transformation parameters. The result of the kinematic measurement with respect to the velocity $\boldsymbol{V}$ and the offset between the time axes is denoted by the vector $\boldsymbol{x}$. Equation (2) shows that the determination of a kinematic measurement uncertainty should be treated as an inverse uncertainty evaluation. The process parameter V must be taken into consideration, but cannot be measured directly by a photogrammetric system (see next paragraph). As a result, knowledge of the kinematic process governing the object movement is a significant contributor to the posterior density of the kinematic result $\boldsymbol{x}$. Equation (2) is illustrated in section 4.4 using the shutter-time of the photogrammetric system.

A straightforward approach to deduce the velocity in real-time makes use of the most recent measurement and the measurement one time step earlier this results in the following equation

$$V = \frac{(x_2 - x_1)}{\Delta t}. \tag{3}$$

Here Δt is the time interval between the two measurements x_1 and x_2. The standard deviation of the velocity can be calculated using the LPU as follows

$$\sigma_V = \sqrt{2 \cdot \left(\frac{\sigma_x}{\Delta t}\right)^2 + \left(\frac{(x_1 - x_2) \cdot \sigma_{\Delta t}}{\Delta t^2}\right)^2}. \tag{4}$$

Where the standard deviation of the measurements are $\sigma_{x_1} = \sigma_{x_2} = \sigma_x$. The standard deviation of the time interval between the two measurements is denoted by $\sigma_{\Delta t}$. If the timestamps of the two measurements are perfect the the standard deviation $\sigma_{\Delta t}$

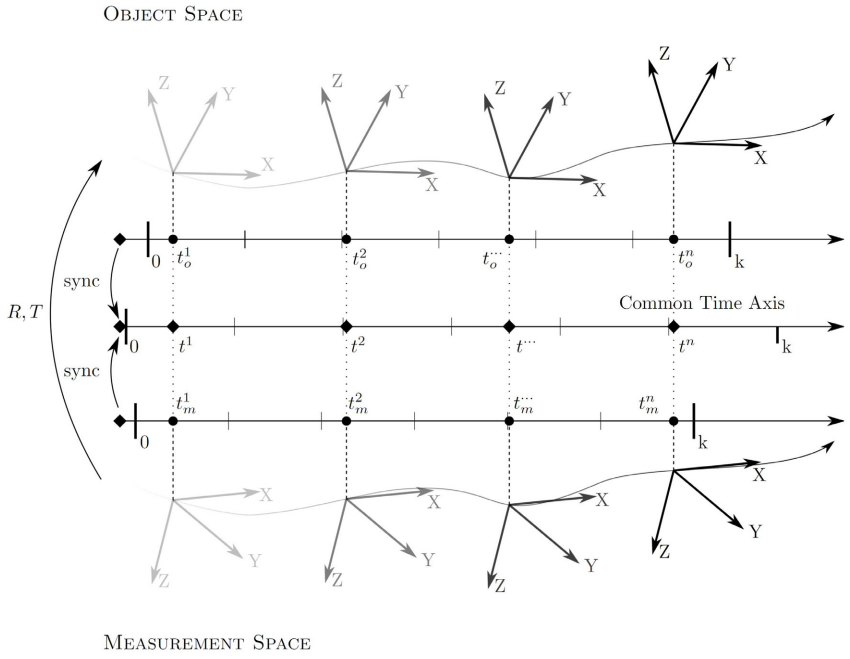

Figure 1: Object space and measurement space

reduces to zero and the standard error of the velocity is given by:

$$\sigma_V = \sqrt{2} \cdot \left(\frac{\sigma_x}{\Delta t} \right). \tag{5}$$

With this equation it is clearly visible that the velocity deduced using the last equation can be considered as too inaccurate for use in the LVM, as any uncertainty deduced would be directly proportional to the measurement frequency used.

In the LVM, the measurement systems commonly use frequencies higher than 1 Hz, and therefore result in an increasing variance compared with the standard deviation of the actual measurement σ_x. Therefore, this method is inappropriate to deduce the velocity in order to incorporate it into the estimate of a kinematic uncertainty of x. Furthermore in reality most movements of an object are much more complex than a straight line with constant velocity.

In summary, the kinematic uncertainty estimation can be considered as an inverse uncertainty evaluation which depends on additional process information, e.g. the velocity of the object being tracked and measured. This information cannot be directly measured by any common measurement system in the LVM, e.g. a photogrammetric system or a laser tracker. Nor, with a sufficiently good variance, can these be deduced from the measurements, as pointed out above. Furthermore this information is not sufficient to describe the whole movement.

As stated above, a kinematic measurement is dependent on the object's kinematics. This means that the description of such a measurement should involve the kinematic process. A very common approach to achieve this is called state-space representation. Within this approach the state of the observed object is stored in a state vector, which is made up of all relevant information to describe the object's state. In the case of a kinematic 3D measurement, this information may be the position, velocity and acceleration, depending on the object's movement. The state space equations of a non-linear stochastic discrete-time state space model are

$$\boldsymbol{x}_{t+1} = f_t\left(\boldsymbol{x}_t, \boldsymbol{u}_t, w_t\right) \tag{6}$$

$$\boldsymbol{z}_t = h_t\left(\boldsymbol{x}_t, v_t\right) \tag{7}$$

Here f is the system model function with its system process noise w, the control input u and the state vector $\boldsymbol{x}$. The measurement model function h includes its measurement noise v. The state-space approach

focuses on the state vector which is under investigation and can be analysed using Bayesian filters.

3 Bayesian filtering

A Bayesian filter is an optimal non-linear state estimator which determines the conditional PDF of the state vector $\boldsymbol{x}(t)$ given all information at time t. This is made up of the information about the prior state of the system, the control inputs and the available measurements. Therefore a Bayesian filter perfectly matches the requirements postulated by GUM and is ideally suited to calculate a kinematic uncertainty.

The required conditional state PDF at time t is $P(x_t|I_t)$ with the available information set I at time t. This information set consists of

$$I_t = \{\boldsymbol{z}_{1:t}, \boldsymbol{u}_{1:t-1}\}. \tag{8}$$

Here $\boldsymbol{z}_{1:t}$ are all measurements up to time t and $\boldsymbol{u}_{1:t-1}$ are all control inputs up to time $t-1$ [13]. Using [13, 14], the conditional density of $\boldsymbol{x}_{t+1}$ at time $t+1$ can be written using Bayes' formula as

$$\begin{aligned} p(\boldsymbol{x}_{t+1}|I_{t+1}) &= p(\boldsymbol{x}_{t+1}|\boldsymbol{z}_{1:t+1}, \boldsymbol{u}_{1:t}) \\ &= p(\boldsymbol{x}_{t+1}|\boldsymbol{z}_{1:t}, \boldsymbol{z}_{t+1}, \boldsymbol{u}_{1:t}) \\ &= \frac{p(\boldsymbol{z}_{t+1}|\boldsymbol{x}_{t+1}, \boldsymbol{z}_{1:t}, \boldsymbol{u}_{1:t})\; p(\boldsymbol{x}_{t+1}|\boldsymbol{z}_{1:t}, \boldsymbol{u}_{1:t})}{c} \\ &= \frac{p(\boldsymbol{z}_{t+1}|\boldsymbol{x}_{t+1}, I_t, \boldsymbol{u}_t)\; p(\boldsymbol{x}_{t+1}|I_t, \boldsymbol{u}_t)}{c} \end{aligned} \tag{9}$$

Here c is the normalisation constant as $c = p(\boldsymbol{z}_{t+1}|I_t, \boldsymbol{u}_t)$. Considering independent process and measurement noise sequences, and taking the state vector as a Markov process, it can be shown that

$$p(\boldsymbol{x}_{t+1}|I_{t+1}) = \frac{1}{c}\, p(\boldsymbol{z}_{t+1}|\boldsymbol{x}_{t+1})\; p(\boldsymbol{x}_{t+1}|I_t, \boldsymbol{u}_t) \tag{10}$$

which is known as the state update equation of a Bayesian filter [14, 13]. For the following analysis method it is imported to mention, that state-dependent process and measurement noise are allowed [13]. The requirement of a Markov process assumes that the state at $\boldsymbol{x}_t$ is complete and the evolution of future states is not influenced by variable prior to $\boldsymbol{x}_t$[14]. In order to calculate the PDF prediction $p(\boldsymbol{x}_{t+1}|I_t, \boldsymbol{u}_t)$ needed in equation (10) the Chapman-Kolmogorov equation

$$p(\boldsymbol{x}_{t+1}|I_t, \boldsymbol{u}_t) = \int p(\boldsymbol{x}_{t+1}|\boldsymbol{x}_t, \boldsymbol{u}_t)\; p(\boldsymbol{x}_t|I_t)\, d\boldsymbol{x}_t \tag{11}$$

can be utilized [13]. According to [13] equation (10) yields the minimum mean-square error of the current state which can expressed as

$$\hat{\boldsymbol{x}}_{t+1}^{\mathrm{MMSE}} = E[\boldsymbol{x}_{t+1}|I_{t+1}] = \int \boldsymbol{x}_{t+1}\, p(\boldsymbol{x}_{t+1}|I_{t+1})\, d\boldsymbol{x}_{t+1}. \tag{12}$$

Equation (10) together with (11) make a Bayesian filter which consists of two steps. The first step is the prediction step, see equation (11), in which a prior PDF is calculated using a system model, in general equation (6). A system model describes the evolution of the system over time. The second step is called the state update step, which calculates the required PDF see equation (10) and (7). To perform this step a measurement model is needed which relates the noisy measurements to the state. To apply a Bayesian filter it is necessary that the system model, as well as the measurement model, are available in a deterministic form and in a probabilistic form.

3.1 System model

In general Bayesian filtering for kinematic uncertainty estimation can be subdivided into two major categories. These are filtering with a known system model and filtering with an unknown system model.

The first case, filtering with a known system model, is found by tracking and measuring the tool centre point of an industrial robot. This is synchronized with the measurement system so that the control information of the robot can be used in conjunction with data of the measurement system.

The second case, filtering with an unknown system model, occurs if the measurement system cannot be synchronized with the robot's data. This case is similar to the situation where a human operator moves the object being tracked and measured.

A traditional Bayesian filter is the Kalman filter. However, when estimating the continuous state of a moving object, without using synchronized process data, it does not perform very well, because of the unknown control inputs and insufficient knowledge of the system. The usual approach is to include the model inaccuracies into the process noise, which results in a reduction of the state accuracy. This leads to a hybrid estimation problem in which the continuous state of the object and the discrete model is estimated [15]. In this paper, the continuous dynamic of the hybrid system is modelled by difference equations

and the discrete-state dynamic is modelled using a finite Markov chain. As shown in [5] a hybrid system estimator can be utilised for kinematic laser tracker measurements which can be adapted as pointed out below.

In contrast to equation (6) and (7) a discrete-time stochastic hybrid system can be expressed as

$$\boldsymbol{x}_{t+1} = f_t^i\left(\boldsymbol{x}_t, w_t^i\right) \tag{13}$$

$$\boldsymbol{z}_t = h_t^i\left(\boldsymbol{x}_t, v_t^i\right). \tag{14}$$

Here f^i is the system model function of model i in conjunction with its process noise w^i. The measurement model function of model i is denoted with h^i and its measurement noise v^i. An Interacting Multiple Model (IMM), used in this paper, is a hybrid system estimator which approximates the required posterior density $p\left(\boldsymbol{x}_t|\boldsymbol{z}_t\right)$ by a weighted sum of Gaussian density functions as

$$p\left(\boldsymbol{x}_t|\boldsymbol{z}_t\right) \approx \sum_{i=1}^{r} w_t^i \mathcal{N}\left(\boldsymbol{x}_t^i; \hat{\boldsymbol{x}}_t^i, P_t^i\right) \tag{15}$$

$$\text{with} \qquad \sum_{i=1}^{r} w_t^i = 1, \tag{16}$$

where w_t^i are weights and $\hat{\boldsymbol{x}}_t^i$ denotes the model-conditioned state estimate with its covariance $\boldsymbol{P}_t^i$ [16]. To avoid an IMM filter with an increasing number of mixture components, only the most probable components are used and merged together to form one state estimate [16]. Within an IMM filter these components are the most probable system models representing the object's kinematic behaviour e.g. a constant acceleration with a certain noise level.

As stated above, the discrete-state dynamic is modelled using a finite Markov chain. The evolution of a model i is governed by the finite Markov chain. The exponent i denotes the model whose evolution is governed by the Markov chain as

$$\mu_{t+1} = \Pi\, \mu_t. \tag{17}$$

The count of discrete models within the Markov chain is r. Thus the transition probability matrix is of the dimension $\Pi = \{\pi_{ij}\} \in \mathbb{R}^{r\times r}$ and the model probabilities are denoted with μ. The final hybrid state estimate of an IMM filter can be written as

$$\hat{\boldsymbol{x}}_{t+1} = \sum_{i=1}^{r} \hat{\boldsymbol{x}}_{t+1}^i p\left(m_{t+1}^i|\boldsymbol{z}_{1:t+1}\right). \tag{18}$$

Here $p\left(m_{t+1}^i|\boldsymbol{z}_{1:t+1}\right)$ are the weights, compare with equation (16), which are the model probabilities. The model-conditioned state estimate of x_{t+1} is

$$\hat{\boldsymbol{x}}_{t+1}^i = \int \boldsymbol{x}_{t+1}\, p\left(\boldsymbol{x}_{t+1}|\boldsymbol{z}_{t+1}, m_i^{t+1}\right) d\boldsymbol{x}_{t+1}, \tag{19}$$

under the condition that the model at time $t+1$ is m_{t+1}^i using the estimator of model i according to [15]. As the IMM filter is here a host of different Kalman filters, each of them modelling another kinematic behaviour, the model-conditioned state estimator is simply a Kalman filter. This can be directly compared with equation (12) which is the optimal state estimator with respect to the minimum mean-square error of a common Bayesian filter.

An IMM filter can be subdivided into three major steps:

- interaction / mixing,
- filter,
- state estimate and covariance combination.

The following derivation is based on [5, 13, 15].

Interaction/mixing step

Within the first step, new initial states and covariances are calculated to be used in each Kalman filter. This is done by weighting the Kalman filter outputs, the state and the covariance, with the mixing probability as follows

$$\hat{\boldsymbol{x}}_t^{0j} = \sum_{i=1}^{r} \hat{\boldsymbol{x}}_t^i\, \mu_{t|t}^{ij} \qquad j = 1, \ldots, r \tag{20}$$

$$P_t^{0j} = \sum_{i=1}^{r} \left\{ P_t^i + \left[\hat{x}_t^i - \hat{x}_t^{0j}\right] \times \left[\hat{x}_t^i - \hat{x}_t^{0j}\right] \right\} \mu_{t|t}^{ij} \qquad j = 1, \ldots, r \tag{21}$$

here $\hat{\boldsymbol{x}}_i^t$ is the state estimate and P_i^t is the covariance result of Kalman filter i after the measurement update at time t. The conditional probability, that the system made the transition from model i to j at time $t+1$ is denoted by $\mu_{t|t}^{ij}$ and can be calculated using

$$\mu_{t|t}^{ij} = \frac{1}{\bar{c}_j}\pi_{ij}\mu_t^i$$

$$\bar{c}_j = \sum_{i=1}^{r} \pi_{ij}\mu_t^i. \tag{22}$$

Here c_j is the normalization constant and μ_t^i is model probability of model i at time t.

Filter step

The second step includes the filtering with the Kalman filter of each model. The prediction and update step can be expressed briefly for a linear system as

$$\left[\hat{\boldsymbol{x}}_{t+1}^{-,i}, P_{t+1}^{-,i}\right] = \mathrm{KF}_p\left(\hat{\boldsymbol{x}}_t^{0j}, P_t^{0j}, A_t^i, Q_t^i\right) \tag{23}$$

$$\left[\hat{\boldsymbol{x}}_{t+1}^{i}, P_{t+1}^{i}\right] = \mathrm{KF}_u\left(\hat{\boldsymbol{x}}_{t+1}^{-,i}, P_{t+1}^{-,i}, \boldsymbol{z}_{t+1}, H_{t+1}^i, R_{t+1}^i\right). \tag{24}$$

Here KF_p is the prediction step of a Kalman filter and KF_u is the update step. The transition matrix is denoted by A and Q is the covariance matrix of the system which are derived from the system model m^i. H represents the measurement matrix and R is the covariance matrix of the measurement model.

In addition, the model probability for each model is needed within an IMM filter. The model probability is determined as

$$\mu_{t+1}^j = \frac{1}{c}\Lambda_{t+1}^j \overline{c}_j \qquad j = 1, \ldots, r \tag{25}$$

and the normalization constant c can be calculated as

$$c = \sum_{j=1}^{r} \Lambda_{t+1}^j \overline{c}_j. \tag{26}$$

The required likelihood for each model can be calculated as

$$\Lambda_{t+1}^j = \mathcal{N}\left(\boldsymbol{d}_{t+1}; 0, S_{t+1}^j\right). \tag{27}$$

Here, the residuals of the measurement $t+1$ of the model m^j are $\boldsymbol{d}_{t+1}$ and S_{t+1}^j is the innovation covariance matrix in the KF update step of model m^j.

State estimate and covariance combination

The goal of this step is to calculate the combined state estimate and covariance over all filter results of each Kalman filter. This can be done according to equation (16) as a weighted sum as

$$\begin{aligned}\hat{\boldsymbol{x}}_{t+1} &= \sum_{j=1}^{r} \mu_{t+1}^j \hat{\boldsymbol{x}}_{t+1}^j \\ P_{t+1} &= \sum_{j=1}^{r} \mu_{t+1}^j \left\{ P_{t+1}^j + \left[\hat{\boldsymbol{x}}_{t+1}^j - \hat{\boldsymbol{x}}_{t+1}\right] \right. \\ &\quad \left. \cdot \left[\hat{\boldsymbol{x}}_{t+1}^j - \hat{\boldsymbol{x}}_{t+1}\right]^T \right\}. \end{aligned} \tag{28}$$

3.2 Measurement model

As stated, in order to apply a Bayesian filter a probabilistic measurement model is also needed. According to [5] the variance of a 3D point can be expressed in a first-order approximation as follows

$$\begin{aligned}\sigma_{x_k}^2 &= \sigma_x^2 + t_s^2\sigma_{V_x}^2 + V_x^2\sigma_{t_s}^2 \\ \sigma_{y_k}^2 &= \sigma_y^2 + t_s^2\sigma_{V_y}^2 + V_y^2\sigma_{t_s}^2 \\ \sigma_{z_k}^2 &= \sigma_z^2 + t_s^2\sigma_{V_z}^2 + V_z^2\sigma_{t_s}^2 \end{aligned} \tag{29}$$

. Here t_s denotes the synchronization error between the measurement system and the common time axis and σ_{t_s} its standard deviation. The velocity is represented by V with its standard deviation σ_V for each axis x, y, z. This assumes there is a zero or negligible time delay between the two cameras and that the object moves with constant velocity.

4 Experiment

In order to test the performance of a hybrid filter against a common Kalman filter a simulation was carried out before the analysis of the experiment.

4.1 Simulation

The simulation included tracking an object on a trajectory consisting of a segment with a constant velocity and a segment with a constant turn rate. Within this simulation the measurement system was assumed to be a stereo photogrammetric system and the movement simulated was conducted in a plane perpendicular to the viewing axis of the measurement system. A common Kalman filter was set up, which included a constant velocity model described by

$$\dot{\boldsymbol{x}}(t) = \begin{bmatrix} 0 & I^{3\times3} \\ 0 & 0 \end{bmatrix} \boldsymbol{x}(t) + \begin{bmatrix} 0 \\ I^{3\times3} \end{bmatrix} \boldsymbol{w}(t) \tag{30}$$

according to [13]. Here the state vector is $\boldsymbol{x} = [x, y, z, \dot{x}, \dot{y}, \dot{z}]$ and $\boldsymbol{w}$ denotes the process noise.

The hybrid system filter was made up of the Kalman filter described above and additionally of an unscented Kalman filter including the constant turn model as described in section 4.3.1. Here, the state vector is $\boldsymbol{x} = [x, y, z, \dot{x}, \dot{y}, \dot{z}, \ddot{x}, \ddot{y}, \ddot{z}]$ which shows that an IMM filter can also cope with models having different dimensions.

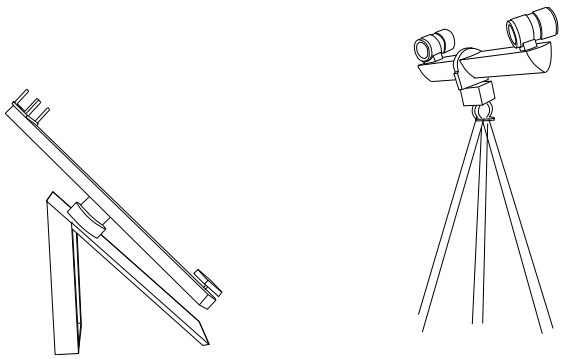

Figure 2: Sketch of the experiment set-up, showing the configuration of the rotation system and the stereo photogrammetric system.

4.2 Experiment Set-up

The experimental setup is shown in figure 2 and comprises a rotating component and the MoveInspect stereo photogrammetric system from AICON. To observe the rotation of the arm there are photogrammetric targets attached to the arm at different heights, four on small rods at the end of the arm and eight on the arm itself. To balance the additional weight of these rods a counter weight is attached to the other end of the arm.The rotation plane is tilted by about 45° from the horizontal plane and an air bearing is used to achieve a very precise and stable circle during the kinematic movement. To cover most of the image sensor the photogrammetric system is also tilted and placed 1.5 m away from the rotating system. As the arm is 1 m long, the resulting radius should be roughly 0.5 m. The observation of the kinematic process begins in the speed-up phase of the arm and continues until it has reached the desired angular velocity.

4.3 System model

In the experimental setup above it can be inferred that at least two major kinematic behaviours occur during the experiment and these should be modelled separately. The speeding-up phase can be expressed by the variable turn model, in which the object is assumed to change its angular velocity during each time step. Additionally, the imperfect balancing of the rotating arm and the rudimentary motor drive must lead to some angular velocity variations on the circle which are also addressed using this model. After the speed-up phase, one can assume that the object remains at a nearly constant angular velocity which can be modelled by a planar constant turn model.

As the photogrammetric system delivers coordinates at discrete times but the object movement is described in a continuous time state, the object state equations must be transformed to the corresponding discrete time equations. Alternatively, the object movement can be directly modelled using discrete time equations. This results in slightly different process noise covariance matrices which are easier to interpret [13]. Thus, both methods model different process approximations, where the latter assumes a piecewise constant noise and the former a continuous-time noise. The difference can be shown using the example of a constantly moving object in one dimension with the state $\boldsymbol{x} = [x,\, \dot{x}]$. This results, according to [13], in the following two covariance matrices

$$Q_c = \begin{bmatrix} 1/3\Delta t^3 & 1/2\Delta t^2 \\ 1/2\Delta t^2 & \Delta t \end{bmatrix} \tilde{q}$$
$$Q_d = \begin{bmatrix} 1/4\Delta t^4 & 1/2\Delta t^3 \\ 1/2\Delta t^3 & \Delta t^2 \end{bmatrix} \sigma_v^2. \qquad (31)$$

Here, $\tilde{q}$ denotes the power spectral density of the process noise, Δt the sampling period and σ_v^2 the process variance. The covariance matrix Q_c is obtained from the continuous state by using the inverse Laplace transformation and the matrix Q_d is obtained by multiplying the process noise by the vector gain $\Gamma = \left[1/2\Delta t^2, \Delta t\right]^T$ [13]. If one assumes the same magnitude of acceleration modelled in the process noise $\tilde{q}$ and σ_v then the position variance of Q_d is smaller

$$Q_c^{1,1} = 1/3\,\Delta t^4 \sigma_v^2 \;>\; 1/4\,\Delta t^4 \sigma_v^2 = Q_d^{1,1}. \qquad (32)$$

However, to describe the process of the experiment, the following models are deduced by discretisation of a continuous time model with additional noise and using the inverse Laplace transformation as proposed in [13]. This seems to be more appropriate to describe the experiment's kinematics.

4.3.1 Constant turn model

According to [17] a planar constant turn, in the so called navigation plan, can be described using

$$\dot{\boldsymbol{x}}(t) = \begin{bmatrix} 0 & I^{3\times3} & 0 \\ 0 & 0 & I^{3\times3} \\ 0 & -\omega^2 I^{3\times3} & 0 \end{bmatrix} \boldsymbol{x}(t) + \begin{bmatrix} 0 \\ 0 \\ I^{3\times3} \end{bmatrix} \boldsymbol{w}(t). \tag{33}$$

Here, the state vector is $\boldsymbol{x} = [x, y, z, \dot{x}, \dot{y}, \dot{z}, \ddot{x}, \ddot{y}, \ddot{z}]^T$ and $\boldsymbol{w}$ is the process noise. Assuming, that the angular velocity vector Ω is perpendicular to the velocity vector $\boldsymbol{v}$, the acceleration vector is $\boldsymbol{a}$ and the angular acceleration is zeros, then the turn rate ω is given by

$$\omega = |\Omega| = \frac{|\boldsymbol{v} \times \boldsymbol{a}|}{v^2}. \tag{34}$$

Using the Laplace transform in conjunction with equation (33) results in the following discrete time model

$$\boldsymbol{x}_{t+1} = \begin{bmatrix} I^{3\times3} & \frac{\sin(\omega\,\Delta t)}{\omega} I^{3\times3} & \frac{1-\cos(\omega\Delta t)}{\omega^2} I^{3\times3} \\ 0 & \cos(\omega\,\Delta t)\; I^{3\times3} & \frac{\sin(\omega\,\Delta t)}{\omega} I^{3\times3} \\ 0 & -\omega\,\sin(\omega\,\Delta t)\; I^{3\times3} & \cos(\omega\,\Delta t)\; I^{3\times3} \end{bmatrix} \cdot \boldsymbol{x}_t + \boldsymbol{w}_t, \tag{35}$$

with the covariance matrix

$$cov(\boldsymbol{w}_t) = \begin{bmatrix} a' I^{3\times3} & b' I^{3\times3} & c' I^{3\times3} \\ b' I^{3\times3} & d' I^{3\times3} & e' I^{3\times3} \\ c' I^{3\times3} & e' I^{3\times3} & f' I^{3\times3} \end{bmatrix} \tilde{q}$$

$$a' = \frac{(\sin(2\,\omega\,\Delta t) - 8\,\sin(\omega\,\Delta t) + 6\,\omega\,\Delta t)}{4\,\omega^5}$$

$$b' = \frac{2\,\sin\left(\frac{\omega\,\Delta t}{2}\right)^4}{\omega^4}$$

$$c' = \frac{-\sin(2\,\omega\,\Delta t) + 4\,\sin(\omega\,\Delta t) - 2\,\omega\,\Delta t}{4\,\omega^3}$$

$$d' = \frac{-\sin(2\,\omega\,\Delta t) + 2\,\omega\,\Delta t}{4\,\omega^3}$$

$$e' = \frac{\sin(\omega\,\Delta t)^2}{2\,\omega^2}$$

$$f' = \frac{\sin(2\,\omega\,\Delta t) + 2\,\omega\,\Delta t}{4\,\omega}.$$

Here, $\tilde{q}$ represents the power spectral density of the process noise and Δt is the sampling period. As can be seen in equation (35), the turn rate is needed. This can be calculated using equation (34) from the estimates of the velocity and the acceleration within each time step.

4.3.2 Variable turn model

A planar variable turn model with the state vector $\boldsymbol{x} = [x, y, z, \dot{x}, \dot{y}, \dot{z}, \ddot{x}, \ddot{y}, \ddot{z}]^T$ can be described by

$$\dot{\boldsymbol{x}}(t) = \begin{bmatrix} 0 & I^{3\times3} & 0 \\ 0 & 0 & I^{3\times3} \\ 0 & -(\omega_c^2 + \alpha^2)\; I^{3\times3} & -2\,\alpha\, I^{3\times3} \end{bmatrix} \boldsymbol{x}(t) + \begin{bmatrix} 0 \\ 0 \\ I^{3\times3} \end{bmatrix} \boldsymbol{w}(t). \tag{36}$$

according to [17]. Here $\omega_c = \alpha^2 + \omega^2$ and $w(t)$ the white noise. As for the constant turn model the angular velocity vector must be perpendicular to the velocity vector and the turn rate ω can be calculated with equation (34). According to [17] the damping coefficient α can be determined from the acceleration and the velocity with

$$\alpha = -\frac{\boldsymbol{v} \cdot \boldsymbol{a}}{v^2}. \tag{37}$$

Using the Laplace transform, the corresponding discrete time model can be found as

$$\boldsymbol{x}_{t+1} = \begin{bmatrix} I^{3\times3} & a' I^{3\times3} & b' I^{3\times3} \\ 0 & c' I^{3\times3} & d' I^{3\times3} \\ 0 & e' I^{3\times3} & f' I^{3\times3} \end{bmatrix} \boldsymbol{x}_t + \boldsymbol{w}_t,$$

$$a' = \left(2\alpha\omega_c - \mathrm{e}^{-\alpha\,t'}\left(2\alpha\omega_c c_0 + \left(\alpha^2 - \omega_c^2\right) s_0\right)\right) / (\omega_c\, a_0)$$

$$b' = \left(\omega_c - \mathrm{e}^{-\alpha\,t'}\left(\omega_c c_0 + \alpha s_0\right)\right) / (\omega_c a_0)$$

$$c' = \mathrm{e}^{-\alpha\,t'}\left(\omega_c c_0 + \alpha s_0\right) / \omega_c$$

$$d' = \mathrm{e}^{-\alpha\,t'} s_0 / \omega_c$$

$$e' = -\,\mathrm{e}^{-\alpha\,t'} a_0 s_0 / \omega_c$$

$$f' = \mathrm{e}^{-\alpha\,t'}\left(\omega_c c_0 - \alpha s_0\right) / \omega_c \tag{38}$$

with the covariance matrix

$$cov(\boldsymbol{w}_t) = \begin{bmatrix} a' I^{3\times3} & b' I^{3\times3} & c' I^{3\times3} \\ b' I^{3\times3} & d' I^{3\times3} & e' I^{3\times3} \\ c' I^{3\times3} & e' I^{3\times3} & f' I^{3\times3} \end{bmatrix} \tilde{q}$$

$$a' = \mathrm{e}^{-2\alpha\,t'}\left(\alpha\left(c_1\left(\alpha^2 - 3\omega_c^2\right) - s_1\left(3\alpha^2 - \omega_c^2\right) + 16\alpha\omega_c^2 \mathrm{e}^{\alpha\,t'} c_0 + 8\omega_c \mathrm{e}^{\alpha\,t'} s_0\left(\alpha + \omega_c\right)\left(\alpha - \omega_c\right)\right) - a_0^2 + \omega_c^2 \mathrm{e}^{2\alpha\,t'}\left(\omega_c^2 - 11\alpha^2 + 4\alpha\, t' a_0\right)\right) / \left(4\alpha\omega_c^2 a_0^3\right)$$

$$b' = \mathrm{e}^{-2\alpha t'}\left(\omega_c c_0 - \omega_c \mathrm{e}^{\alpha t'} + \alpha s_0\right)^2 / \left(2\omega_c^2 a_0^2\right)$$

$$c' = -\,\mathrm{e}^{-2\alpha t'}\left(\alpha\left(\alpha - c_1 + s_1\right) + \omega_c^2 \mathrm{e}^{2\alpha t'} -\right.$$

$$\omega_c^2 - 4\alpha\omega_c e^{\alpha t'} s_0\Big) / \Big(4\alpha\omega_c^2 a_0\Big)$$

$$d' = \frac{-e^{-2\alpha t'}\left(\alpha\left(\alpha - c_1 + s_1\right) - \omega_c^2 e^{2\alpha t'} + \omega_c^2\right)}{4\alpha\omega_c^2 a_0}$$

$$e' = e^{-2\alpha t'} s_0^2 / \left(2\omega_c^2\right)$$

$$f' = \frac{e^{-2\alpha t'}\left(\alpha\left(-\alpha + c_1 + s_1\right) + \omega_c^2 e^{2\alpha t'} - \omega_c^2\right)}{4\alpha\omega_c^2}$$

using the auxiliary variables

$$\begin{aligned} c_0 &= \cos\left(\omega_c t'\right) & s_0 &= \sin\left(\omega_c t'\right) \\ c_1 &= \alpha\cos\left(2\omega_c t'\right) & s_1 &= \omega_c \sin\left(2\omega_c t'\right) \\ a_0 &= \alpha^2 + \omega_c^2 & t' &= \Delta t. \end{aligned}$$

The power spectral density of the process noise is denoted by $\tilde{q}$ and the sampling period by Δt. Equation (34) is used to calculate the turning rate and equation (37) the damping coefficient, in conjunction with the estimates of the velocity and the acceleration.

4.4 Measurement model

The 3D point determination method used is stereo triangulation. As there are some uncertainties in the calibration of the photogrammetric system, as well as in the determination of the image coordinates $\tilde{m}$, the two rays are skew and do not intersect exactly in 3D space. The ray constellation for 3D point and two camera images can be seen in figure 3. Because of this imperfect intersection, the 3D determination method minimizes the length of vector $\boldsymbol{s}$ and uses the midpoint of the vector as an approximation of the 3D point, which is denoted by M in figure 3. Based on this 3D location method, the projection of the 3D point onto the image plane is briefly given by [18] as follows

$$s\tilde{m}_i = P_i\tilde{M} \tag{39}$$

$$\text{with} \quad P_i = A_i P_N D_i \quad D_i = \begin{bmatrix} R_i & t_i \\ 0_3 & 1 \end{bmatrix} \quad 0_3 = [0,0,0]$$

$$P_N = \begin{bmatrix} 1 & 0 & 0 & 0 \\ 0 & 1 & 0 & 0 \\ 0 & 0 & 1 & 0 \end{bmatrix}$$

Here $\tilde{m}_i = (u, v, 1)^T$ is the homogeneous image coordinate of the camera i and the corresponding homogeneous world coordinate is $\tilde{M} = (X, Y, Z, 1)^T$. The exterior orientation of the camera is expressed using the rotation $R_i^{3\times3}$ and translation $t_i^{3\times1}$ with respect to a common world coordinate frame. The interior camera calibration is collected in matrix $A_i^{3\times3}$ consisting of the principal point and the focal length [18]. Using equation (39) for two images of the same 3D point results in two equations. These equations can be used to reconstruct the 3D point using either the homogeneous or the inhomogeneous method [18]. 3D point projection is also affected by distortion caused by the lens and sensor in the camera. During the calibration of the photogrammetric system the radial symmetrical, asymmetrical and tangential distortion as well as the affinity and non-orthogonality of each camera are determined. For the sake of simplicity in equation (39) the assumption was made that the image coordinates had already been corrected for these effects according to the method described in [19]. The vector $\boldsymbol{s}$ can be seen as a quality criterion [20, 7]. This is used in the AICON system to deduce a standard deviation for each 3D point determination. As the two cameras of the photogrammetric system are cascaded, there must be an internal synchronization error between camera one and camera two influencing vector $\boldsymbol{s}$, depending on the whole kinematic behaviour of the object e.g. direction and velocity. Thus, the standard deviation is also affected and therefore a Bayesian filter can be used, assuming the PDF is a Gaussian distribution.

In addition, the shutter-time can also produce errors during kinematic measurements as the camera needs some integration time for a precise determination of a point's centroid. Therefore, any movement during this integration time must lead to a deviation of the point coordinate which is dependent on the shutter-time as well as the velocity and direction. Given that the planed trajectory is a circle, the centroid of a retro-reflecting target tends to drift towards the centre of the circle as shown in figure 4. Assuming, to a first order-approximation, a circle on the image plane, then the centroid's coordinates on a circle segment can be calculated as

$$\begin{aligned} x_c &= \frac{R}{\tau}\sin(\tau) \\ y_c &= \frac{R}{\tau}\left(1 - \cos(\tau)\right) \end{aligned} \tag{40}$$

according to [21] using the curve integral. Here, R is the radius and τ denotes the angle travelled throughout the shutter-time. Furthermore it is assumed that there is no light density variation during the shutter-

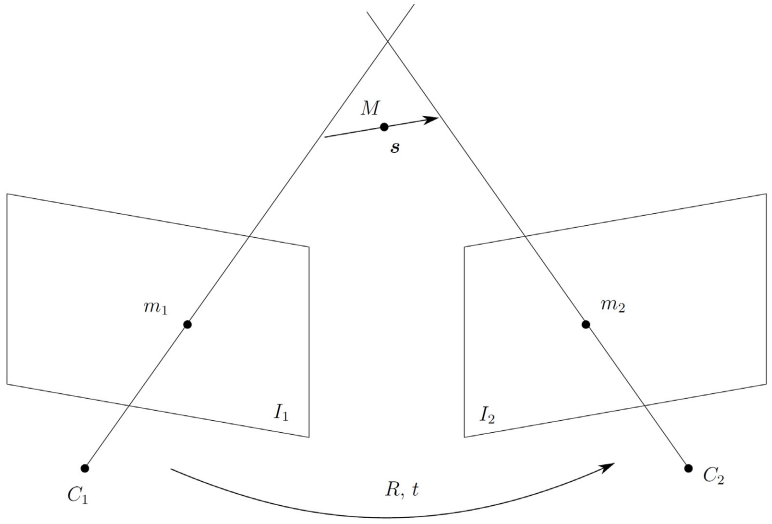

Figure 3: Stereo triangulation according to [18]. The rays are skew to each other, due to the imperfect image point measurement m_i and the uncertainties in the calibration parameter.

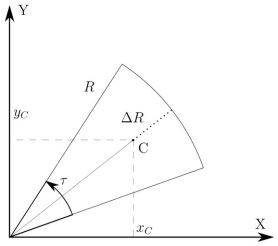

Figure 4: Centroid tends to drift towards the centre of the circle, because of the shutter-time and the velocity.

time.

4.5 Implementing within an IMM filter

In order to implement the proposed system models from the last section, an appropriate Bayesian filter type must be chosen. As both models are non-linear, they cannot be implemented using a common Kalman filter. Because the measurement model is assumed to have a Gaussian distribution they are ideally suited to be implemented in an unscented Kalman filter. Because of the Gaussian distribution the unscented Kalman filter is more suitable and not the particle filter as described in [14].

The implementation of a IMM filter can be simplified as it is known that only one photogrammetric system observed the experiment and that this measurement system is the same for both filters. Further simplification can be made as the state vector in each system model has the same dimension and the same elements. Therefore the equation (24) can be simplified to

$$\left[\hat{\boldsymbol{x}}^i_{t+1}, P^i_{t+1}\right] = \mathrm{KF}_u\left(\hat{\boldsymbol{x}}^{-,i}_{t+1}, P^{-,i}_{t+1}, \boldsymbol{z}_{t+1}, H_{t+1}, R_{t+1}\right). \tag{41}$$

A more detailed description of the Kalman filter and the required equations can be found in [13, 14, 22]. To overcome numerical issues within these common equations a variant of factorization methods can be found in [23].

5 Results

In order to analyse the rotating system, the attached photogrammetric targets were cropped together within one virtual 6 degree-of-freedom (DoF) probe, thus resulting in higher 3D point accuracy than using just one target. The virtual point of the 6 DoF probe was calculated using a function within the AICON software. Figure 5 shows a sketch of the 6DoF probe and virtual target point. Where the

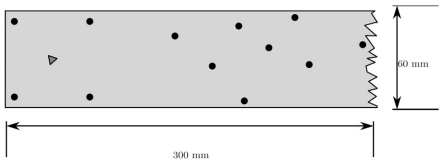

Figure 5: Sketch of the virutual probe. Photogrammetric targets, shown as circles on the probe, are used to calculate a virtual target point shown as a triangle.

virtual point is depicted by a grey triangle and the photogrammetric targets as a circle. As the AICON software does not provide a standard deviation for this virtual point one had to be deduced. The deduction was made using the standard deviations provided by the real photogrammetric targets and the mean standard deviation for the virtual tip point was set to 40 µm for the analysis with the proposed IMM filter.

The results of the analysis with the proposed IMM filter, can be seen in figure 6, where each figure shows one coordinate component with its 3σ standard deviation interval scaled by a factor of 200. In these figures one can slightly see the speeding up phase of the arm at the beginning which results in the expected shortening of the wave length of sine signal in each coordinate component. The mean standard deviation was estimate at 69 µm. It can also be seen that the standard deviation increases at the maximum and the minimum of sine curve. During this experiment, the photogrammetric system was operated at a frequency of 200 Hz. According to equation (5), this would lead to a standard deviation of $11.3\,\mathrm{mm\,s^{-1}}$ for the velocity. However, the mean standard deviation of the velocity using the IMM filter results in $0.9\,\mathrm{mm\,s^{-1}}$ which clearly shows the advantage of the Bayesian approach.

Using equation (40) the error due to the shutter time is the difference between the observed radius and real radius R_r

$$\Delta R = \sqrt{x_c^2 + y_c^2} - R_r. \tag{42}$$

With a shutter-time of 50 µs, a radius of 0.5 m and a velocity of $0.5\,\mathrm{m\,s^{-1}}$ the error due to the shutter time is $\Delta R = -5 \times 10^{-11}\,\mathrm{m}$, which is negligibly small. Thus, comparing with figure 4 the shutter-time causes an offset in the angle α travelled. This can also be interpreted as an offset to the time stamp on the common time axis in this experiment.

In order to check the performance of the IMM filter in comparison with the common Kalman Filter, an object with a constant velocity was simulated. The trajectory of this simulation included a straight line segment at the beginning and ends up in a circle segment with a radius of 0.3 m within the XY-plane, as can be seen in figure 7. During this simulation, the object reached a mean speed of $1.2\,\mathrm{m\,s^{-1}}$ and the two models, the constant velocity and the constant turn as introduced in section 4.1, were applied.

The simulation was carried out once with a common Kalman filter using the constant velocity model and once with the IMM filter. Within the IMM filter, a constant velocity model in conjunction with a common Kalman filter was used, and additionally an unscented Kalman filter with a constant turn model. The results of the simulation are depicted in figure 8. Within these figures, the Kalman filter estimation error is drawn as a dotted line and the estimation error of an IMM filter depicted as a dashed line. To confirm that the determined PDF of an IMM filter includes all uncertainties, the 3σ standard deviation is plotted as a solid line. Thus, 99.7 % of the estimation errors must lie between the two solid lines. Despite employing the Kalman filter, this can be easily verified for the IMM filter for all coordinate components. One can clearly see that the Kalman filter crosses this boundary during the second trajectory segment along the circle and generates systematic deviations. These deviations are only visible in the X and Y components as this is the plane of the curve. The errors are roughly the same as those of the IMM filter during the first segment moving along the straight line with a constant speed. Yet it can also be seen that the estimated standard deviation of the IMM filter increases slightly throughout the constant turn segment of the trajectory, which is a non-linear model. As pointed out in section 3.1, this result of the common Kalman filter was anticipated.

6 Conclusion

It was shown that a kinematic uncertainty can be estimated in accordance to GUM, in real time and using Bayesian filters, in order to include the kinematic behaviour of the object which plays an important role in these uncertainties. To overcome the limitations of

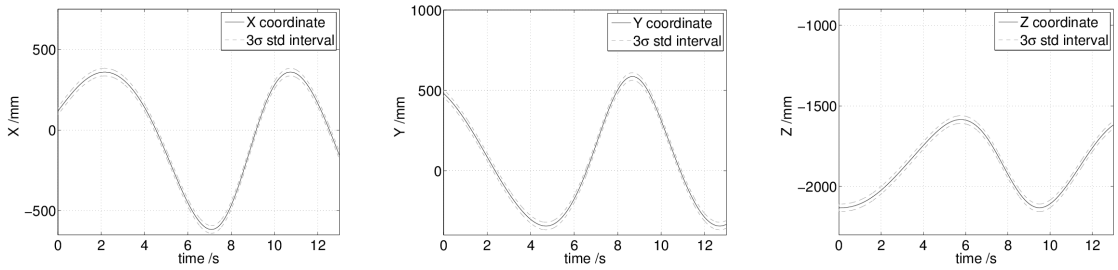

(a) X Coordinate (b) Y Coordinate (c) Z Coordinate

Figure 6: The estimate X, Y, Z coordinates used the proposed IMM filter with their 3σ interval scaled with 200.

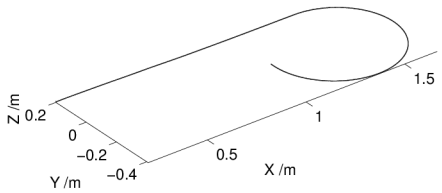

Figure 7: Simulated trajectory.

a common Kalman filter, a hybrid system filter was proposed which could adapt itself to the current kinematic behaviour of the object. Within the Bayesian filters a more natural description of the system models, reflecting the kinematic behaviour of the object, was achieved by deducing them from a continuous description of the kinematics. This results in system models having less influence on the position estimate than the system models deduced from a discrete description. From the simulation above, it can be seen that an IMM filter outperforms a common Kalman filter and fulfils the requirements of GUM.

The experiment with a rotation system in conjunction with a photogrammetric system showed that the hybrid filter can estimate a path uncertainty with respect to the uncertainty of the photogrammetric system. Furthermore, it was shown that the velocity can be estimated more accurately than when using a straightforward approach and thus supports a more reliable kinematic uncertainty estimation in real time.

The results therefore show that the IMM filter is a reasonable way to estimate the kinematic uncertainty of a process embodying different kinds of kinematic behaviours. However the limitation of this approach is very clear, the internal system models of the IMM filter must roughly fit the observed process. With regards to the low uncertainties achievable by LVM instrumentation, this might make the choice of system model difficult. The real-time measurement of industrial robots might benefit from this approach due to their high repeatability.

7 Outlook

As the system models used in a Bayesian filter are just models of the real movement, and the measurement model is a simplification, it would be necessary to test the whole analysis approach against a kinematic reference, in order to best identify missing kinematic influences or incorrect modelling. To widen the range of possible applications, the decision of the kinematic models should be carried out by the method instead of requiring knowledge of the process in advance. Applications like free-from surface scanning, where a person carries a scanner with markers, would also need to be observed in real time and could, in turn, benefit from this analysis method.

Acknowledgement

My heartfelt thanks to the team at the NPL for their generosity and kindness during my stay in London. Gratefully thanks to AICON for the gracious loan of their equipment. My sincere thanks to GRACE for their kind and continued support.

KIT acknowledges financial support under Joint Research Project IND53 of the European Metrology Research Programme (EMRP). The EMRP is jointly

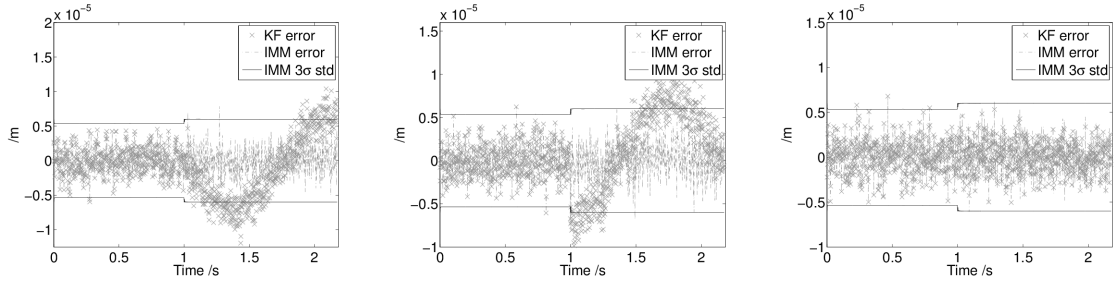

(a) X Estimation Error (b) Y Estimation Error (c) Z Estimation Error

Figure 8: The estimation error in X,Y,Z of the common Kalman filter approach and the IMM filter as proposed in section 4.1

.

funded by the EMRP participating countries within EURAMET and the European Union.

References

[1] Karl Foppe, Volker Schwieger, and Rudolf Staiger. Grundlagen kinematischer Mess- und Auswertetechniken. In *Kinematische Messmethoden Vermessung in Bewegung*, pages 3–18, 2004.

[2] R. Loser. *Weiterentwicklung eines absoluten, hochpräzisen und trackingfähigen Distanzmessers für industrielle Anwendungen*. Mitteilungen. Institut für Geodäsie und Photogrammetrie an der Eidgenössischen Technischen Hochschule Zürich. Inst. für Geodäsie und Photogrammetrie, 2001.

[3] Jürgen Peipe. High Resolution Data Acquisition to Observe Moving Objects. In *Close Range Techniques and Machine Vision*, volume XVIII. ISPRS, July 1996.

[4] Heiner Kuhlmann. Mathematische Modellbildung zu kinematischen Prozessen. In *Kinematische Messmethoden Vermessung in Bewegung*, pages 19–33, 2004.

[5] Thomas Ulrich. Uncertainty estimation and multi sensor fusion for kinematic laser tracker measurements. *Metrologia*, 50(4):307, 2013.

[6] Georg Wiora, Pavel Babrou, and Reinhard Männer. Real time high speed measurement of photogrammetric targets. In CarlEdward Rasmussen, HeinrichH. Bülthoff, Bernhard Schölkopf, and MartinA. Giese, editors, *Pattern Recognition*, volume 3175 of *Lecture Notes in Computer Science*, pages 562–569. Springer Berlin Heidelberg, 2004.

[7] T. Luhmann, S. Robson, S. Kyle, and J. Boehm. *Close-range Photogrammetry and 3D Imaging*. De Gruyter textbook. De Gruyter, 2013.

[8] A.B. Forbes. Approaches to evaluating measurement uncertainty. *International Journal of Metrology and Quality Engineering*, 3:71–77, 2012.

[9] Maurice G Cox and Bernd R L Siebert. The use of a monte carlo method for evaluating uncertainty and expanded uncertainty. *Metrologia*, 43(4):S178, 2006.

[10] J. A. Sousa and A. Forbes. The GUM, bayesian inference and forward and inverse uncertainty evaluation. In *2ª Conferência Nacional da SPMet - Metrologia e Inovação*, 2007.

[11] Ignacio Lira and Wolfgang Wöger. Comparison between the conventional and bayesian approaches to evaluate measurement data. *Metrologia*, 43(4):S249, 2006.

[12] Ignacio Lira. *Evaluating the measurement uncertainty : fundamentals and practical guidance*. Series in measurement science and technology. IOP, Inst. of Physicis Publ., Bristol [u.a.], 2002.

[13] Yaakov Bar-Shalom, X. Rong Li, and Thiagalingam Kirubarajan. *Estimation with applications to tracking and navigation : [theory, algorithms and software]*. A Wiley-Interscience publication. Wiley, New York, 2001.

[14] Sebastian Thrun, Wolfram Burgard, and Dieter Fox. *Probabilistic robotics*. Intelligent robotics and autonomous agents. MIT Press, Cambridge, Mass., 2005.

[15] I. Hwang, H. Balakrishnan, and C. Tomlin. State estimation for hybrid systems: applications to aircraft tracking. *Control Theory and Applications, IEE Proceedings* -, 153(5):556–566, Sep 2006.

[16] Branko Ristic, Sanjeev Arulampalam, and Neil Gordon. *Beyond the Kalman filter : particle filters for tracking applications*. Artech House radar library. Artech House, Boston, Mass. [u.a.], 2004.

[17] X.R. Li and V.P. Jilkov. Survey of maneuvering target tracking. Part I. Dynamic models. *Aerospace and Electronic Systems, IEEE Transactions on*, 39(4):1333–1364, Oct 2003.

[18] Oliver Schreer. *Stereoanalyse und Bildsynthese : mit 6 Tabellen*. Springer, Berlin, 2005.

[19] Robert Godding. *Handbook of machine vision*, chapter Camera Calibration, pages 333–360. WILEY-VCH, 2006.

[20] Keith B. [Hrsg.] Atkinson, editor. *Close range photogrammetry and machine vision*. Whittles, Caithness, 1996.

[21] Gerhard Merziger and Thomas Wirth. *Repetitorium der höheren Mathematik*. Binomi, Springe, 4. aufl., [nachdr.] edition, 2002.

[22] Dan Simon. *Optimal state estimation : Kalman, H. [infinity] and nonlinear approaches*. Wiley-Interscience, Hoboken, NJ, 2006.

[23] G.J. Bierman. *Factorization Methods for Discrete Sequential Estimation*. Dover Books on Mathematics Series. Dover Publications, 2006.

Uncertainty Estimation and Multi Sensor Fusion for Kinematic Laser Tracker Measurements

Thomas Ulrich

This is an author-created, un-copyedited version of an article accepted for publication in Metrologia. Neither the International Bureau of Weights and Measures nor IOP Publishing Ltd is responsible for any error or omissions in this version of the manuscript or any version derived from it. The version of Record is available online at http://stacks.iop.org/0026-1394/50/i=4/a=307.

Abstract

Laser trackers are widely used to measure kinematic tasks such as tracking robot movements.

Common methods to evaluate the uncertainty in the kinematic measurement include approximations specified by the manufacturers, various analytical adjustment methods and the Kalman filter. In this paper a new, real-time technique is proposed, which estimates the 4D-path (3D-position + time) uncertainty of an arbitrary path in space. Here a hybrid system estimator is applied in conjunction with the kinematic measurement model. This method can be applied to processes, which include various types of kinematic behaviour, constant velocity, variable acceleration or variable turn rates. The new approach is compared with the Kalman filter and a manufacturer's approximations. The comparison was made using data obtained by tracking an industrial robot's tool centre point (TCP) with a Leica laser tracker AT901 and a Leica laser tracker LTD500. It shows that the new approach is more appropriate to analysing kinematic processes than the Kalman filter, as it reduces overshoots and decreases the estimated variance. In comparison with the manufacturer's approximations, the new approach takes account of kinematic behaviour with an improved description of the real measurement process and a reduction in estimated variance. This approach is therefore well-suited to the analysis of kinematic processes with unknown changes in kinematic behaviour as well as the fusion among laser trackers.

1 Introduction

Laser trackers have been widely and successfully used to calibrate industrial robots for many years. The most common calibration method is the static technique, which means that the robot moves from point to point, pausing at each to enable calibration measurements to be made. On the other hand, during a kinematic technique (often loosely called "dynamic robot calibration") the robot does not pause at calibration points to save a lot of time. But to apply a kinematic calibration method, the kinematic uncertainty of the measuring process as well as the dynamic model of the robot have to be known and the measurement uncertainty must be lower than the absolute accuracy of the robot.

In addition to robot calibration, there is another important class of application which can benefit from this knowledge. This is free-form surface scanning in which a laser line scanner is kinematically tracked as it is moved over a surface to be measured. Both applications lead to the question: What is the uncertainty in a trajectory measured kinematically by laser trackers?

The laser tracker itself is a measurement device, which follows with its laser beam a moving reflector and measures its 3D position in spherical coordinates. The distance to the reflector is measured by interferometer (IFM) or absolute distance meter (ADM) and two optical angle encoders measure the direction to the reflector. The retro-reflector returns the outgoing laser beam back to the tracker where part of the return beam is directed onto a position sensing device (PSD). Any lateral movement of the reflector generates an offset signal at the PSD, which is used in a control loop to automatically point the laser beam back to the centre of the reflector and to improve the angle encoder readings. In a first approximation, Cartesian values of a laser tracker 3D point can be calculated from the distance and angle measurements

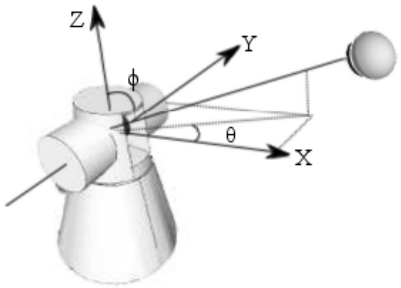

Figure 1: Common laser tracker.

as follows,

$$\begin{aligned} x &= d * cos(\theta) * sin(\phi) \\ y &= d * sin(\theta) * sin(\phi) \\ z &= d * cos(\phi), \end{aligned} \tag{1}$$

where θ denotes the yaw angle, ϕ the pitch angle and d the distance (compare with figure 1). The angle and distance parameters in (1) are not raw measurement values from the encoders but are modified to account for other design parameters in the laser tracker. Some current laser tracker designs are shown in figure 3.

An industrial robot was used to move a cat's-eye retro-reflector along a predefined 3D trajectory in order to obtain experimental data, including different kinematic characteristics such as different velocities or accelerations. This data was then used to investigate the kinematic uncertainty of a Leica Laser Tracker AT901. The fused uncertainty between the two Leica Laser Trackers, AT901 and LTD500, was also considered, as it can be expected, that the fused uncertainty is lower for the same trajectory. During the experiment, laser tracker measurements were triggered by an external source. The internal control loop of the laser tracker under test operates at a constant frequency of 3000 Hz. As a part of this loop, the PSD outputs, the angle encoders readings and the distances are stored with an associated timestamp. These timestamps are generated at a frequency of 1 MHz and therefore have a resolution of 1 µs. They are used to interpolate measurements to match the timing of the external trigger impulse so that the latter does not interrupt the normal measuring process of the laser tracker. The final 3D point values, which are sent to an application, are therefore based on interpolated elements [1],[2].

The objective is to calculate the kinematic uncertainty of the 3D trajectory of the industrial robot measured by a Leica Laser Tracker AT901. The 3D coordinate for this type of laser tracker can be computed by (32) according to the laser displacements and angle encoder readings. Due to the laser tracker design type, the laser displacements and the angle encoder readings are under the prescribed uncertainties as formulated in (29) which have to be taken in account to calculate a over-all uncertainty of the laser tracker measurements. To apply a Bayesian filter the target position must be described in a system model (see section 4.1 Development of the System Model). Finally a hybrid system estimator is used as a Bayesian filter to calculate and to improve the kinematic uncertainty of the trajectory.

2 Kinematic Measurement

The term "kinematic measurement" can be interpreted in different ways, as shown in [3]. In this paper, a kinematic laser tracker measurement is considered as a spatiotemporal measurement of a moving reflector, hence the result can be linked via the common time axis with other measurements.

There are a number of existing methods for different applications which can be used to analyse such kinematic measurements. For example, [4] suggests adjustment method in a post-processing analysis step and [5] suggests a Kalman Filter as a real time method, but with some restrictions. Amongst other issues, the probabilistic system model of the kinematic process must be known and all error terms must have a Gaussian distribution. To detect periodic patterns, a time series analysis was suggested by [3]. Bayesian inference was also used in the field of coordinate measuring machines, for a small measurement volume to estimate the output probability density function (pdf), in order to describe the resulting measurement uncertainty for non-linear dynamic processes [6]. In this approach, the assumption has been made that the target movement can be modelled locally by a polynomial of some degree. The estimated uncertainty is therefore dependent on the degree of the polynomial and on the given measurement frequency. However, none of these suggested techniques is suitable to describe the 4D path uncertainty of large volume laser tracker measurements of an arbitrary path in a real-time application, which may have

different kinematic characteristics, such as different velocities, different accelerations, and variable turn rates. Hence, the aforementioned techniques can not be utilized to estimate the 4D uncertainty of an arbitrary path for the fused combination between laser trackers.

In order to improve the analysis of laser tracker data it is possible to utilise the state-space approach to modelling dynamic systems. Here a dynamic system is one that changes its state over time. The state-space approach focuses on the state vector of the system which is under investigation. The state vector is made up of all relevant descriptive information of the system, such as the position and the velocity. In the case of a spatial tracking problem, the information is related to the kinematic characteristics of the moving reflector. The reflector, together with the laser tracker, can therefore be seen as a dynamic system, which can be analysed with Bayesian filters. If the kinematic characteristic of the path is not known in advance, this problem can be considered as a state estimation problem of a hybrid system. In the case of a hybrid system, the estimation of the combination of the continuous state vector as well as that of the discrete model is required. The discrete model reflects kinematic characteristics. For example if the reflector moves at a constant velocity or on a curve, or if it is accelerating, this characteristic is clearly reflected in the state vector of the model. Hybrid systems have been extensively studied in the field of air traffic control [7],[8],[9],[10], autonomous vehicles and driving assistance systems [11].

In this paper the analysis is based on Bayesian filtering and a hybrid system estimator to both estimate kinematic uncertainty and to improve it. The analysed task is the kinematic measurement of industrial robot and this analysis is compared with the aforementioned alternative methods, additional the sensor fusion between the two laser trackers is considered.

3 Bayesian Filtering

The kinematic laser tracker measurement of a moving reflector can be viewed as a dynamic system. To analyse a dynamic system with the Bayesian filter approach, two models are required:

- A system model that describes the evolution of the system over time.
- A measurement model relating the noisy data measurements to the state.

If these models are available in a probabilistic form, the state space formulation is ideally suited to the application of Bayesian filters [12].

A Bayes filter calculates a posterior distribution, the probability distribution over the state vector $\boldsymbol{x}_t$ at time t based on all past measurements $\boldsymbol{z}_{1:t}$ and on all past control inputs of the system model $\boldsymbol{u}_{1:t}$, examples for these parameters can be found in section 4. In general a Bayes filter consists of a prediction step and an update step. The prediction step at time t calculates a prior pdf using a system model and requires the pdf $p\left(\boldsymbol{x}_{t-1}|\boldsymbol{z}_{1:t-1}\right)$. As described in [13] the prior pdf can be calculated by,

$$p\left(\boldsymbol{x}_t|\boldsymbol{z}_{1:t-1},\boldsymbol{u}_{1:t}\right)=\int p\left(\boldsymbol{x}_t|\boldsymbol{x}_{t-1},\boldsymbol{u}_t\right) p\left(\boldsymbol{x}_{t-1}|\boldsymbol{z}_{1:t-1},\boldsymbol{u}_{1:t-1}\right)dx_{t-1} \quad (2)$$

The update step calculates the required posterior as follows,

$$p\left(\boldsymbol{x}_t|\boldsymbol{z}_{1:t},\boldsymbol{u}_{1:t}\right)=\frac{p\left(\boldsymbol{z}_t|\boldsymbol{x}_t\right)p\left(\boldsymbol{x}_t|\boldsymbol{z}_{1:t-1},\boldsymbol{u}_{1:t}\right)}{p\left(\boldsymbol{z}_t|\boldsymbol{z}_{1:t-1},\boldsymbol{u}_{1:t}\right)} \quad (3)$$

Within the update step, the current measurements $\boldsymbol{z}_t$ modify the prior pdf depending on the likelihood function, which is defined by the measurement model. For the derivation of the Bayes filter the assumption is made that the state $\boldsymbol{x}_t$ is a first-order Markov chain. The variance of the resulting pdf after the update step can be seen as an kinematic uncertainty since it includes all influences of the measuring process, as well as the system process. Therefore the determination of the kinematic uncertainty is conform to the "Guide to the Expression of Uncertainty in Measurement"[14].

To sum up, a standard kinematic laser tracker measurement can be seen as a tracking problem in which the system model is not known and must be estimated. Due to the fact that the dynamic system model of the kinematic process is often not accurately known in advance, the analysis method should take several system models into account in order to calculate the best estimation. For example, a very often used system model is the constant velocity model, thereby it is assumed, that the tracking target moves with a constant velocity. In order to consider more than one dynamic system model the hybrid system estimator approach can be utilized.

3.1 System Model

A Kalman filter is a traditional Bayesian filter but does not perform very well when estimating the continuous state of a reflector, because it is likely that the model on which the filter is based, does not accurately represent the current behaviour of the reflector at all times. Due to the unknown inputs $\boldsymbol{u}_{1:t}$ of the tracking system for the analysis, the usual approach is to include the model inaccuracies into the process noise, which reduces the accuracy of the state.

Estimation of both the continuous state and the discrete model leads to a so-called hybrid estimation problem [7]. The hybrid systems used in this paper model the continuous dynamic by difference equations and the discrete-state dynamics by a finite Markov chain.

A discrete-time stochastic hybrid system can be expressed as follows,

$$\begin{aligned} \boldsymbol{x}_{t+1} &= f_t^i\left(\boldsymbol{x}_t, \boldsymbol{u}_t, w_t^i\right) \\ \boldsymbol{z}_t &= h_t^i\left(\boldsymbol{x}_t, v_t^i\right), \end{aligned} \tag{4}$$

where f^i is the system model function of model i with its system process noise w, and where h^i is the measurement model function of model i with its measurement noise v. The model i is governed by the finite Markov-chain

$$\mu_{t+1} = \Pi\, \mu_t, \tag{5}$$

where $\Pi = \{\pi_{ij}\} \in \mathbb{R}^{r\times r}$ is the transition probability matrix, $\mu_t \in \mathbb{R}^r$ is the model probability, and r the count of models. The state estimate can be expressed as

$$\hat{\boldsymbol{x}}_{t+1} = \sum_{i=1}^{r} \hat{\boldsymbol{x}}_{t+1}^i p\left(m_{t+1}^i | \boldsymbol{z}_{1:t+1}\right), \tag{6}$$

where $\hat{\boldsymbol{x}}_{t+1}^i = \int x_{t+1} p\left(x_{t+1}|\boldsymbol{z}_{1:t+1}, m_{t+1}^i\right) \mathrm{d}x_{t+1}$ is the state estimate of the state $\boldsymbol{x}_{t+1}$ given the conditional probability, the model at time $t+1$ is m_{t+1}^i and is computed by the state estimator matched to model i, based on [7]. Hence, the estimator in (6) can be seen as a weighted sum with the weights $p\left(m_{t+1}^i|\boldsymbol{z}_{1:t+1}\right)$, which are the model probability μ_{t+1}^i of the model i at time t_{t+1}.

The Interacting Multiple Model (IMM) filter is a widely used hybrid system estimator due to its excellent performance in comparison with other hybrid system estimators [7]. It approximates a set of possible system models and calculates a combination over all implemented models [9]. Possible models of reflector manoeuvres can therefore be defined in advance, depending on the expected kinematic process. In an IMM filter, the implemented models can also have state vectors with different dimensions. The authors of [7] have proposed an improvement to the IMM filter called Residual-Mean Interacting Multiple Model (RMIMM). They have shown that the model estimation delay of a RMIMM filter is slightly better than the one of an IMM filter. The main difference between the IMM and the RMIMM can be assessed by a specific calculation of the weights for (6), in order to reduce the false model estimation. This is achieved by increasing the difference between the likelihood of the correct model and the others.

The combination of the different models are combined according to a general Markov model, for the transition between the states. An IMM / RMIMM filter consists of a bank of r parallel Bayesian filters and a transition matrix, which defines the transition probability between the states of each model [8]. These filters are usually made up of a range of system models, which are deployed by different Bayesian filters like a Kalman– or Particle Filter [9], [15]. Three major steps are carried out in an IMM / RMIMM filter:

- Interaction/Mixing
- Filter
- Estimate and Covariance Combination

The following description of these three steps is loosely based on the derivation of [9]. For a simplified description the Kalman filter is used as an example of a Bayesian filter.

3.1.1 Interaction/Mixing Step

The first step is the interaction/mixing step. Here, calculations of the mixed inputs for each model are made. Assuming a Kalman filter, the mixed inputs are the means and the covariances for each filter that can be calculated as

$$\begin{aligned} \hat{\boldsymbol{x}}_{t-1}^{0j} &= \sum_{i=1}^{r} \mu_{t-1}^{i|j} \hat{\boldsymbol{x}}_{t-1}^i \qquad\qquad j = 1, \cdots, r \\ P_{t-1}^{0j} &= \sum_{i=1}^{r} \mu_{t-1}^{i|j} \left\{ P_{t-1}^i + \left[\hat{\boldsymbol{x}}_{t-1}^i - \hat{\boldsymbol{x}}_{t-1}^{0j}\right] \right. \end{aligned} \tag{7}$$

$$\left[\hat{\boldsymbol{x}}_{t-1}^{i} - \hat{\boldsymbol{x}}_{t-1}^{0j}\right]^{\mathrm{T}}\Bigg\} \qquad j = 1, \cdots, r \tag{8}$$

where $\hat{\boldsymbol{x}}_{t-1}^{i}$ and P_{t-1}^{i} are the mean and covariance for the model i at time step $t-1$. The conditional probability $\mu_{t-1}^{i|j}$, that the system made the transition from model i to model j at time $t-1$, can be calculated as

$$\mu_{t-1}^{i|j} = \frac{1}{\bar{c}_j}\pi_{ij}\mu_{t-1}^{i} \qquad i, j = 1, \cdots, r \tag{9}$$

$$\bar{c}_j = \sum_{i=1}^{r}\pi_{ij}\mu_{t-1}^{i} \qquad j = 1, \cdots, r \tag{10}$$

where π_{ij} is the transition probability for each model m^i, and m^j according to the transition probability matrix of the Markov model. Finally, $\bar{c}_j$ is the normalization factor.

3.1.2 Filter Step

In this second step, the Bayesian filters are applied. If one assumes the Kalman filter for each model m^i, the prediction and update step are as follows,

$$\left[\hat{\boldsymbol{x}}_{t}^{-,i}, P_{t}^{-,i}\right] = \mathrm{KF}_p\left(\hat{\boldsymbol{x}}_{t-1}^{0j}, P_{t-1}^{0j}, A_{t-1}^{i}, Q_{t-1}^{i}\right) \tag{11}$$

$$\left[\hat{\boldsymbol{x}}_{t}^{i}, P_{t}^{i}\right] = \mathrm{KF}_u\left(\hat{\boldsymbol{x}}_{t}^{-,i}, P_{t}^{-,i}, \boldsymbol{z}_t, H_t^i, R_t^i\right) \tag{12}$$

where $\mathrm{KF}_p(\,\cdot\,)$ stands for the Kalman filter prediction step and $\mathrm{KF}_u(\,\cdot\,)$ for the Kalman filter update step. A denotes the system transition matrix and Q the system covariance matrix. Both are derived from the system model m^i. According to the measurement model, H represents the measurement matrix and R the covariance matrix of the measurement model. In addition to the mean and covariance, the model probability for each model m^i must be calculated.

The probability for an IMM / RMIMM filter is determined as

$$\mu_t^j = \tfrac{1}{c}\Lambda_t^j\bar{c}_j \qquad j = 1, \cdots, r \tag{13}$$

where c is the normalization constant, calculated as

$$c = \sum_{j=1}^{r}\Lambda_t^j\bar{c}_j. \tag{14}$$

Within a IMM filter the likelihood of the measurement for each model is calculated as

$$\Lambda_t^j = \mathcal{N}\left(\boldsymbol{d}_t^j; 0, S_t^j\right) \tag{15}$$

where $\boldsymbol{d}_t^j$ are the residuals of the measurements and S_t^j is the innovation covariance matrix for the model m^j in the KF update step. The likelihood for the RMIMM filter is calculated by

$$\Lambda_t^j = \begin{cases} \frac{N_t^j\mathcal{N}(\boldsymbol{d}_t^j;0,S_t^j)}{\sum_{i=1}^{r}N_t^i\mathcal{N}(\boldsymbol{d}_t^j;0,S_t^j)} & \text{if } \bar{d}_t^j \neq 0 \\ \mathcal{N}\left(\boldsymbol{d}_t^j; 0, S_t^j\right) & \text{otherwise} \end{cases} \tag{16}$$

with

$$N_t^i = \begin{cases} \left\|\bar{d}_t^i\right\|^{-1} & \text{if } \bar{d}_t^j \neq 0 \\ 1 & \text{otherwise} \end{cases} \tag{17}$$

where $\bar{d}_t^j$ is the mean value of the residuals in model i at time t. The conditional likelihood Λ^j for each filter is directly comparable to the data association problem. This problem is well known by simultaneous localization and mapping (SLAM) algorithms and has been extensively investigated [16]. The authors of [7] have pointed out that the IMM filter can be improved when the difference between the likelihood values is increased. In SLAM algorithms more features are included in an augmented state vector to obtain a greater difference between the likelihood values to avoid ambiguities [17].

3.1.3 Estimate and Covariance Combination

In this third step, the combined state estimate and covariance are calculated as

$$\begin{aligned} \hat{\boldsymbol{x}}_t &= \sum_{j=1}^{r}\mu_t^j\hat{\boldsymbol{x}}_t^j \\ P_t &= \sum_{j=1}^{r}\mu_t^j\left\{P_t^j + \left[\hat{\boldsymbol{x}}_t^j - \hat{\boldsymbol{x}}_t\right]\left[\hat{\boldsymbol{x}}_t^j - \hat{\boldsymbol{x}}_t\right]^{\mathrm{T}}\right\}. \end{aligned} \tag{18}$$

It can be seen, that the IMM / RMIMM filter is ideally suited to the analysis of longer kinematic measurement where more than one model exists in a dynamic process. Due to the acceleration there are at least two different models, at the beginning and at the end of each kinematic movement, which is otherwise considered as a constant velocity process.

3.2 Measurement Model

The aforementioned Bayesian filter also consists of a measurement model composed of a deterministic and a probabilistic model. (1) can be viewed as the deterministic model and the probabilistic model can be

derived from it with additional probabilistic parameters. With respect to (12) it can be seen, that this model and its covariance can change with each time steep. This property is important for the analysis of kinematic laser tracker measurements, due to the fact that a laser tracker generally consists of a range measuring device as well as two angle encoders. This means that the uncertainty depends on the reflector's position, which changes every time step throughout a kinematic measurement. In spite of some geometrical design differences, the 3-D point variance of a laser tracker can be estimated via the uncertainty propagation as a first-order approximation over

$$\begin{aligned}\sigma_x^2 &= (\cos\theta\,\sin\phi)^2\,\sigma_d^2 + (-d\,\sin\phi\,\sin\theta)^2\,\sigma_\theta^2 + \\ &\quad (d\,\cos\phi\,\cos\theta)^2\,\sigma_\phi^2 \\ \sigma_y^2 &= (\sin\theta\,\sin\phi)^2\,\sigma_d^2 + (d\,\cos\theta\,\sin\phi)^2\,\sigma_\theta^2 + \\ &\quad (d\,\cos\phi\,\sin\theta)^2\,\sigma_\phi^2 \\ \sigma_z^2 &= (\cos\phi)^2\,\sigma_d^2 + (-d\,\sin\phi)^2\,\sigma_\phi^2, \end{aligned} \tag{19}$$

where σ_d denotes the standard deviation of distance, σ_ϕ the standard deviation of the pitch angle, and σ_θ the standard deviation of the yaw angle, see figure 1. (19) do not take into account any correlations between the axes.

In [4] the author describes the synchronization between some trigger pulses as the main source of uncertainty caused by kinematic measurements for the Leica laser tracker model, as the PSD control point —the second error source— is determined during the initialisation of the laser tracker [18]. The synchronization uncertainty is directly linked to the speed, which results in the first order approximation of,

$$\begin{aligned} x_k &= x + V_x \cdot t_s \\ y_k &= y + V_y \cdot t_s \\ z_k &= z + V_z \cdot t_s. \end{aligned} \tag{20}$$

Hence, a kinematic 3D variance can be expressed by

$$\begin{aligned} \sigma_{x_k}^2 &= \sigma_x^2 + t_s^2\,\sigma_{V_x}^2 + V_x^2\,\sigma_{t_s}^2 \\ \sigma_{y_k}^2 &= \sigma_y^2 + t_s^2\,\sigma_{V_y}^2 + V_y^2\,\sigma_{t_s}^2 \\ \sigma_{z_k}^2 &= \sigma_z^2 + t_s^2\,\sigma_{V_z}^2 + V_z^2\,\sigma_{t_s}^2 \end{aligned} \tag{21}$$

where t_s represents the synchronization error, and σ_{t_s} its standard deviation. V is the velocity and σ_V is its standard deviation. Here it is assumed that t_s denotes the synchronization between each trigger impulse as well as the internal synchronization between the distance measuring device and the angle encoders. (20) and (21) are only valid for movement with constant velocity and if no cross correlations between the components occur.

In order to describe a kinematic 3D point uncertainty, environmental influences must also be taken into account. In (19) it can clearly be seen that the kinematic 3D point variance depends on position and synchronization. With a full description of the measurement model and its uncertainty, kinematic laser tracker measurements are appropriate for analysis using a Bayesian filter.

3.3 Multi Sensor Fusion

In order to use measurements of multiple laser trackers together, these must be fused to achieve a more accurate state estimation. In general, multi sensor fusion can be accomplished within a centralized architecture or within a decentralized architecture. The centralized architecture is also known as measurement fusion, as all raw measurements are transmitted to a single fusion node in a sensor network before they are processed. This architecture is very sensitive to spatial and temporal misalignments of the involved sensors [19]. On the other hand the decentralized architecture, also called track-to-track fusion, has a lower performance than the measurement fusion [20], [19], [21]. Within a decentralized architecture, every sensor node preforms its own Bayes filtering to gain a better state estimation, before transferring its information to the fusion node where all state estimations of all sensors are fused together [19]. It can be expected that, the transformation parameters between the laser trackers can be determined sufficient enough, along with the signals that can be precisely synchronized. Therefore measurement fusion is the only architecture type that is considered. In order to use this fusion, (12) must be adjusted as follows

$$\left[\hat{\boldsymbol{x}}_t^i, P_t^i\right] = \mathrm{KF}_u\left(\hat{\boldsymbol{x}}_t^{-,i}, P_t^{-,i}, \tilde{\boldsymbol{z}}_t, \tilde{H}_t^i, \tilde{R}_t^i\right) \tag{22}$$

with

$$\tilde{\boldsymbol{z}}_t = \begin{pmatrix} \boldsymbol{z}_t^1 \\ \vdots \\ \boldsymbol{z}_t^l \end{pmatrix} \qquad \tilde{H}_t^i = \begin{pmatrix} H_t^{i,1} \\ \vdots \\ H_t^{i,l} \end{pmatrix}$$

$$\tilde{R}_t^i = \mathrm{diag}\left[R_t^{i,1}, \cdots, R_t^{i,l}\right],$$

where l is the number of involved laser trackers should be fused. A striking feature of this method can be seen in (22), as it can incorporate measurements from distinct laser tracker models, as long as there is reliable uncertainty describing the measurements. In this fusion approach, it is assumed that the expectancy value of the delay time is zero and the variance is considered as part of the measurement model as proposed in equation (21). An approach dealing with systematically delayed measurements within Bayes filters can be found in [22].

4 Implementation

The following section describes the analysis of a kinematic laser tracker measurement using a Leica AT901 Laser Tracker that followed a cat's eye reflector manipulated by an industrial robot. The predefined trajectory along which the reflector was moved at a constant speed of 500 mm/s and can be seen in figure 4. Due to robot performance limitations, 500 mm/s was the maximum constant speed for this trajectory. The trajectory was defined by the edges of a cube with semicircles on its sides. The robot first moved the reflector along the edges of the cube and then along the semicircles.

4.1 Development of the System Model

With regard to the experiment design and the test trajectory, three system models should be considered:

- Constant velocity
- Constant acceleration
- Coordinated turn

The constant velocity model is used to model the parts of trajectory where a constant velocity can be expected, as e.g. on the edges of the cube a constant velocity of 500 mm/s.Whereas the coordinated turn model is applied to cover the semicircles on the sides.Furthermore the acceleration model is utilized to model the behaviour before and after a change of the moving direction at the corners or at the beginning and at the end of the experiment.

The constant velocity of the reflector is expressed in a continuous, white-noise acceleration model, where the velocity is a Wiener process according to [9]. Hence, the state space vector of the first model is $\boldsymbol{x}^{\mathrm{I}} = [x\ \dot{x}\ y\ \dot{y}\ z\ \dot{z}]^{\mathrm{T}}$. The discrete-time state equation is expressed as

$$\begin{aligned} \boldsymbol{x}_{t+1}^{\mathrm{I}} &= \operatorname{diag}\left[F^{\mathrm{I}}, F^{\mathrm{I}}, F^{\mathrm{I}}\right] x_t + w_t^{\mathrm{I}} \\ F^{\mathrm{I}} &= \begin{bmatrix} 1 & \Delta t \\ 0 & 1 \end{bmatrix} \end{aligned} \tag{23}$$

with the sampling period Δt. The covariance of the discrete-time process noise w_t^{I} is

$$\begin{aligned} Q^{\mathrm{I}} &= \operatorname{diag}\left[Q_c^{\mathrm{I}}, Q_c^{\mathrm{I}}, Q_c^{\mathrm{I}}\right] \tilde{q}^{\mathrm{I}} \\ Q_c^{\mathrm{I}} &= \begin{bmatrix} \frac{1}{3}\Delta t^3 & \frac{1}{2}\Delta t^2 \\ \frac{1}{2}\Delta t^2 & \Delta t \end{bmatrix} \end{aligned} \tag{24}$$

assuming $\tilde{q}^{\mathrm{I}}$ is a constant power spectral density of the process noise. The model with a constant acceleration is expressed as

$$\begin{aligned} \boldsymbol{x}_{t+1}^{\mathrm{II}} &= \operatorname{diag}\left[F^{\mathrm{II}}, F^{\mathrm{II}}, F^{\mathrm{II}}\right] x_t + w_t^{\mathrm{II}} \\ F^{\mathrm{II}} &= \begin{bmatrix} 1 & \Delta t & \frac{1}{2}\Delta t^2 \\ 0 & 1 & \Delta t \\ 0 & 0 & 1 \end{bmatrix} \end{aligned} \tag{25}$$

with the state vector $\boldsymbol{x} = [x\ \dot{x}\ \ddot{x}\ y\ \dot{y}\ \ddot{y}\ z\ \dot{z}\ \ddot{z}]^{\mathrm{T}}$ according to [9]. Here the acceleration is a Wiener process and the covariance of the discrete-time process noise w_t^{II} is

$$\begin{aligned} Q^{\mathrm{II}} &= \operatorname{diag}\left[Q_c^{\mathrm{II}}, Q_c^{\mathrm{II}}, Q_c^{\mathrm{II}}\right] \tilde{q}^{\mathrm{II}} \\ Q_c^{\mathrm{II}} &= \begin{bmatrix} \frac{1}{20}\Delta t^5 & \frac{1}{8}\Delta t^4 & \frac{1}{6}\Delta t^3 \\ \frac{1}{8}\Delta t^4 & \frac{1}{3}\Delta t^3 & \frac{1}{2}\Delta t^2 \\ \frac{1}{6}\Delta t^3 & \frac{1}{2}\Delta t^2 & \Delta t \end{bmatrix} \end{aligned} \tag{26}$$

with $\tilde{q}^{\mathrm{II}}$ the power spectral density of the process noise. The coordinated turn model assumes a constant turn rate ω in a navigation plane [10]. Here the turn rate is defined as the norm of the angle velocity vector $\boldsymbol{\Omega}$ and can be calculated as

$$\omega = \|\boldsymbol{\Omega}\| = \frac{|\boldsymbol{v} \times \boldsymbol{a}|}{v^2} = \frac{|\boldsymbol{v}|\,|\boldsymbol{a}|}{v^2} = \frac{a}{v} \tag{27}$$

if $\boldsymbol{\Omega} \perp \boldsymbol{v}$ [10]. Figure 2 shows the relationship between the velocity vector $\boldsymbol{v}$ as well as the acceleration vector $\boldsymbol{a}$ in the navigation plane, to which the angle velocity vector $\boldsymbol{\Omega}$ is perpendicular. The discrete-time coordi-

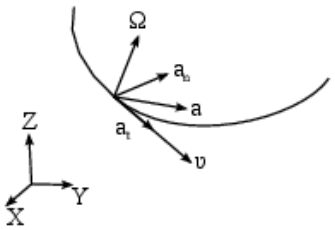

Figure 2: Coordinated turn model.

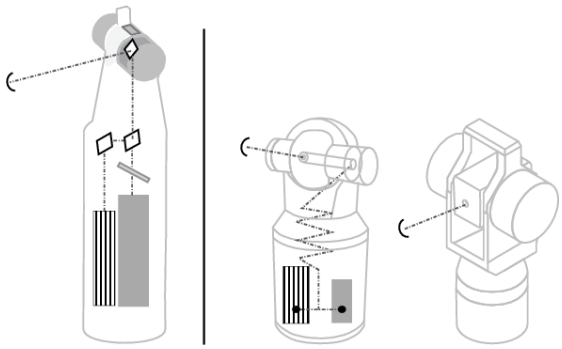

Figure 3: Different design types of laser trackers, either with a gimbal-mounted beam steering mirror or with a gimbal-mounted beam source. The ADM and IFM are depicted as striped and in grey.

nated turn model can be expressed as

$$\boldsymbol{x}_{t+1}^{\mathrm{III}} = \mathrm{diag}\left[F^{\mathrm{III}}(\omega), F^{\mathrm{III}}(\omega), F^{\mathrm{III}}(\omega), 1\right] x_t + \Gamma w_t^{\mathrm{III}}$$

$$F^{\mathrm{III}}(\omega) = \begin{bmatrix} 1 & \sin(\omega\Delta t)/\omega & (1-\cos(\omega\Delta t))/\omega^2 \\ 0 & \cos(\omega\Delta t) & \sin(\omega\Delta t)/\omega \\ 0 & -\omega\sin(\omega\Delta t) & \cos(\omega\Delta t) \end{bmatrix}$$

$$\Gamma = \begin{bmatrix} 0 & 0 & 1 & 0 & 0 & 0 & 0 & 0 & 0 & 0 \\ 0 & 0 & 0 & 0 & 0 & 1 & 0 & 0 & 0 & 0 \\ 0 & 0 & 0 & 0 & 0 & 0 & 0 & 0 & 1 & 0 \\ 0 & 0 & 0 & 0 & 0 & 0 & 0 & 0 & 0 & 1 \end{bmatrix} \tag{28}$$

with the augmented state vector $\boldsymbol{x} = [x\,\dot{x}\,\ddot{x}\,y\,\dot{y}\,\ddot{y}\,z\,\dot{z}\,\ddot{z}\,\omega]^{\mathrm{T}}$, based on [10] and the noise gain matrix Γ to define the effect of the process noise.

The three system models should be sufficient to describe the kinematic process of the robot in hybrid system estimator without losing accuracy as in a Bayes filter, which considers only one system model like, e. g., the Kalman filter. In the hybrid estimator, the curves, the constant velocities as well as the accelerations between each period, are taken into consideration.

4.2 Development of the Measurement Model

In general, commercial laser trackers can be assigned to one of two classes depending on their design. There are laser trackers with with:

- a gimbal-mounted beam steering mirror and
- a gimbal-mounted beam source

Figure 3 shows examples of different types of a laser tracker. Calibration models have been published for both types of laser trackers. A geometrical alignment model for the gimbal-mounted beam source is presented in [23] and in [24]. The Leica Laser Tracker AT901 and the LTD500, belongs to the first group. All these models describe only the geometrical alignment parameters. These are not sufficient to calculate a precise probability density function of a moving reflector, which can be used in a Bayesian filter algorithm, as they do not take into account environmental and kinematic influences.

To develop a measurement model for a trajectory measured kinematically by a Leica laser tracker AT901 or LTD500, the model described in [25] is augmented by additional terms which represent kinematic as well as environmental effects. A group of 16 parameters are used in the geometrical alignment model described in [25]. These parameters are:

- Transit axes offset e
- Mirror offset f
- Beam offset $O1x$ $O1y$
- Cover plate offset $O2x$ $O2y$
- Mirror tilt c
- Transit axis tilt, i
- Beam axis tilt Ix Iy
- Yaw angle encoder eccentricity Ex Ey
- Pitch angle encoder eccentricity Kx Ky
- Pitch angle offset j

- Distance parameter k

This model is valid in both static and kinematic measurements, but for the latter, additional parameters must be taken into consideration. A corrected value for the yaw angle θ_c, the pitch angle ϕ_c, and the distance d_c, can be calculated using these parameters and the correction equations of [25] using the following equations

$$\begin{aligned} \theta_c &= f_{\text{yaw}}\left(\boldsymbol{h}_\theta\right) \\ \phi_c &= f_{\text{pitch}}\left(\boldsymbol{h}_\phi\right) \\ d_c &= f_{\text{distance}}\left(\boldsymbol{h}_d\right) \end{aligned} \tag{29}$$

where $\boldsymbol{h}$ is parameter vector containing the parameters for the correction functions f of the yaw angle θ, the pitch angle ϕ, and the distance d.

To take environmental influences into account, the distance $dist_c$ must be additionally corrected with the formulas according to [26], which depend on

- the temperature
- the air pressure
- the relative humidity
- the wave length of the laser source
- the measured distance.

If these parameters are stored in a vector $\boldsymbol{h}_{meteo}$, the meteorology correction can be expressed in brief as

$$d_{\acute{c}} = f_{meteo}\left(\boldsymbol{h}_{meteo}, d_c\right). \tag{30}$$

To apply (30), it is assumed that these represent the current refractive index along the tracker's laser beam. After utilising the full correction process, a static 3D point can be calculated with (1) as

$$\begin{aligned} x &= d_{\acute{c}} * \cos\left(\theta_c\right) * \sin\left(\phi_c\right) \\ y &= d_{\acute{c}} * \sin\left(\theta_c\right) * \sin\left(\phi_c\right) \\ z &= d_{\acute{c}} * \cos\left(\phi_c\right). \end{aligned} \tag{31}$$

Assuming that one delay time includes the delay time for each component, i.e. the distance and the angle encoders' readings, a kinematic 3D point can be determined with

$$\begin{aligned} x_k &= d_{\acute{c}} * \cos\left(\theta_c\right) * \sin\left(\phi_c\right) + v_x t_s + 1/2\ a_x t_s^2 \\ y_k &= d_{\acute{c}} * \sin\left(\theta_c\right) * \sin\left(\phi_c\right) + v_y t_s + 1/2\ a_y t_s^2 \\ z_k &= d_{\acute{c}} * \cos\left(\phi_c\right) + v_z t_s + 1/2\ a_z t_s^2 \end{aligned} \tag{32}$$

where v expresses the speed and a the acceleration for each axis and t_s the synchronization error.

A deterministic model of a Leica laser tracker is described by (29) to (32). However, a measurement model for a Bayesian filter consists additionally of a probabilistic model. This can be deduced with the variance propagation or with the Monte Carlo Method [27]. For complex functions, it is simpler to use the Monte Carlo Method instead of the variance propagation. In addition, the Monte Carlo Method avoids linearisation errors [13]. (32) used in conjunction with the Monte Carlo Method, can be interpreted as a kinematic virtual laser tracker (kVLT), which determines the probability density for any arbitrary point by applying 30 critical parameters. Normal users can not generally obtain the PSD values during tracking and so the angle standard deviation has to be adjusted to include the behaviour of the PSD sensor. As (30) do not consider a 3D refraction index, the angle encoder readings must be further modified.

4.3 Combining within an IMM Filter

To implement the measurement model and the different system models as described in subsection 4.1, a Bayesian filter type must be chosen. Specific details about the different types of Bayesian filters can be found in [13] and [22]. This decision depends on the model type, linear or non-linear, the parameters' distribution and the approximation error. The extended Kalman filter was chosen in [9], for the non-linear coordinated turn model, and the Kalman filter for a constant velocity model. On the other hand, the particle filter was used for all model types in [15].

For all filters in the filter bank, it is assumed that the laser tracker is always the same. The measurement model is known and the measurements are normal distributed. The filter update equation (12) can be rewritten as

$$\left[\hat{\boldsymbol{x}}_t^i, P_t^i\right] = \mathrm{KF}_u\left(\hat{\boldsymbol{x}}_t^{-,i}, P_t^{-,i}, \boldsymbol{z}_t, H_t, R_t^i\right). \tag{33}$$

In (21), the kinematic variance of a point is dependent on its velocity and variance. The estimated velocity and its variance are different for each filter model. The laser tracker model of (32) is used to determine for each time instance t a covariance matrix R_t^i as follows

$$R_t^i = E\left(\left[\boldsymbol{x}_r - \overline{\boldsymbol{x}}_r\right]\left[\boldsymbol{x}_r - \overline{\boldsymbol{x}}_r\right]^{\mathrm{T}}\right) \tag{34}$$

	Anderson-Darling	Lilliefors
Normally distributed	95.1%	94.9%

Table 1: Normal distribution test.

where $\boldsymbol{x}_r$ is the state vector of $(x_k\ y_k\ z_k)$ and contains the individual random variables according to the Monte Carlo Method of (32).

Due to the assumption of normally distributed measurements, the linear constant velocity model and constant acceleration model are implemented in a Kalman filter, whereas the non-linear coordinated turn model is implemented in an Unscented Kalman filter. To achieve a higher accuracy the Unscented Kalman filter is chosen instead of the Extended Kalman filter. The unscented transformation is more accurate for the propagation of the means and the covariances than the linearisation, which is used by an Extended Kalman filter as shown in [13] and [22]. As described in [13], the Unscented Kalman filter is more convenient to use rather than the Particle Filter if the underlying distribution is approximately normal. Due to the normal distribution the implemented IMM / RMIMM can be seen as a Gaussian sum filter.

5 Results

To determine if the measurement model can be considered as normally distributed, two different tests were made. The first test is the Anderson-Darling test and the second one is the Lilliefors test. The Lilliefors test is based on the well known Kolmogorov-Smirnov test, but in contrast to the latter, the Lilliefors test can be applied even if the mean and covariance are unknown, as described in [28]. In order to compare the two the Anderson-Darling test was also applied. This is based on different statistics from the Kolmogorov-Smirnov test and performances better[29]. The test results for both tests are shown in table 1. For 95% of the test data both tests show that the measurement model can be considered as normally distributed. For both tests, 7900 data points from the test trajectory as shown in figure 4, were used in conjunction with the Monte Carlo method applied to (32) with 5000 samples. The significant level α was set to 0.05 for both tests. It is therefore justifiable to use the Kalman and Unscented Kalman filter in a hybrid system model for further analysis, as previously suggested.

To compare the new analysis methods, i.e. the RMIMM filter and the IMM filter, against more commonly used methods, i.e. the specification of Leica and the Kalman Filter, all methods were tested with the same data set. All shown results were computed with a 1-sigma-interval for the Baysian filters.

The kinematic accuracy for a Leica Laser Tracker LTD500 is specified with $\pm 20 - 40$ µm/m, in [30], [1]. According to [31], this specification can also be applied to the Leica Laser Tracker AT901. Taking account of the reflector's relatively slow speed of approximately 500 mm/s, compared with the tracker's maximum tracking speed of 6 m/s, the lower bound of 20 µm/m was chosen for the analysis. The results of this specification are shown in figure 4a where the range dependency is clearly visible. For the commonly used Kalman filter method suggested in [5], the Leica specification was used as the measurement model. The results of the Kalman filter method are shown in figure 4b. As expected, the standard deviation drops significantly from a minimum of 92 µm to 68 µm, but it is also clear that the variances were set to very large values in order to cover the inaccuracy of the applied model. This effect has already been mentioned in section 3 Bayesian Filtering.

To improve the Kalman filter method, the RMIMM filter and IMM filter were applied to the data set. Figure 5 shows the results and there is no noticeable difference between them. Due to the slow speed of the experiment and the nearly still stand at the model change points at the corners, the advantage of a faster model detection of the RMIMM filter, instead of the IMM filter, cannot be seen. In contrast, the difference between the commonly used methods in figure 4 and hybrid algorithm methods in figure 5, is obvious. With the coordinated turn model, the hybrid filters are also capable of dealing with the cross-track deviations of the robot. They are also sensitive to the low standard deviation of laser tracker measurement, which is not the case with the more common Kalman filter. The clear range dependency shows that the speed of 500 mm/s is too slow therefore the alignment errors and range dependency overlap the kinematic uncertainty effects. By contrast there must be a significant lower standard deviation at the corners where the speed drops nearly to zero in order to change its direction of movement as can

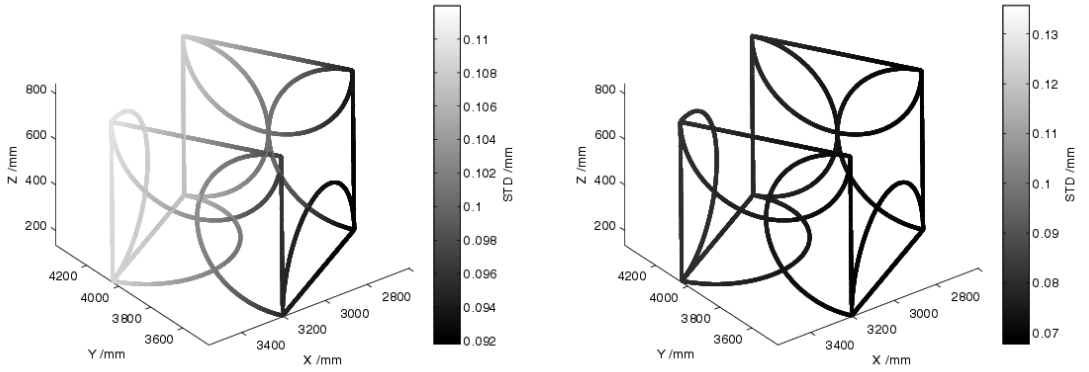

(a) Specification (b) Kalman filtering

Figure 4: Standard analysis methods.

be seen from figure 6. The higher range dependency at slower speeds, emphasizes the importance of reliable static laser tracker models, assuming the delay time can be taken as ± 5 µs as claimed in [2] and [4]. Specifying a delay time of zero could be justified by the post-processing interpolation step, as discussed in section 1 Introduction.

In order to qualify the performance of the hybrid system estimators a simulation of one edge of the cube was conducted to obtain entirely known data. In this simulation the developed laser tracker model was used, with the assumption, that dynamic and kinematic effects can be neglected. As the assumption was made, that there is a constant velocity on the edges of the cube, it is sufficient to use a Kalman filter. The result of the Kalman filter was a mean standard deviation of 21 µm, which shows how small the uncertainties in figure 5 and in the table 2 are.

Another advantage of the hybrid algorithms is that they avoid overshoots, which not only generate poor standard deviation but also slightly wrong state estimates. As expected, these overshoots are found at path corners where the system model changes. These overshoots are no specific result of the Kalman filter method. They are caused by the fact that a normal Bayes filter considers only one system model. This means also other Bayes filters, like the particle filter, would produce wrong state estimates as so shown in [6]. One example of these overshoots is shown in figure 7. Hybrid algorithms successfully prevent overshoots, due to their fast model detection. There is no occurrence of overshoots where the RMIMM filter generates a faster model detection than the IMM filter. In addition figure 7 shows, that there were no clear model change points at every corner. The robot makes a small loop instead of a curve or sharp edge, which leads to many more model changes than expected and ultimately to calculation of a higher standard deviation by the hybrid algorithms.

To compare all analysis methods, their mean standard deviations were calculated and listed in table 2. One can see that the IMM and RMIMM filters deliver the smallest mean standard deviation with 0.024 mm. With respect to the theory of the RMIMM filter it was expected, that it delivers the smallest mean standard deviation. This is dependent on the long still stand time at the beginning and at the end of the experiment. During these periods, small movements of the robot were interpreted as model changes by the RMIMM filter, which provided a higher standard deviation as a result. It can be seen, therefore, that the hybrid filters deliver roughly four times better standard deviation than the approximation of the manufacture and three times better than the common Kalman filter approach.

	RMIMM	IMM	Specific.	KF
Mean standard deviation [mm]	0.024	0.024	0.102	0.074

Table 2: Comparison between the analysis methods.

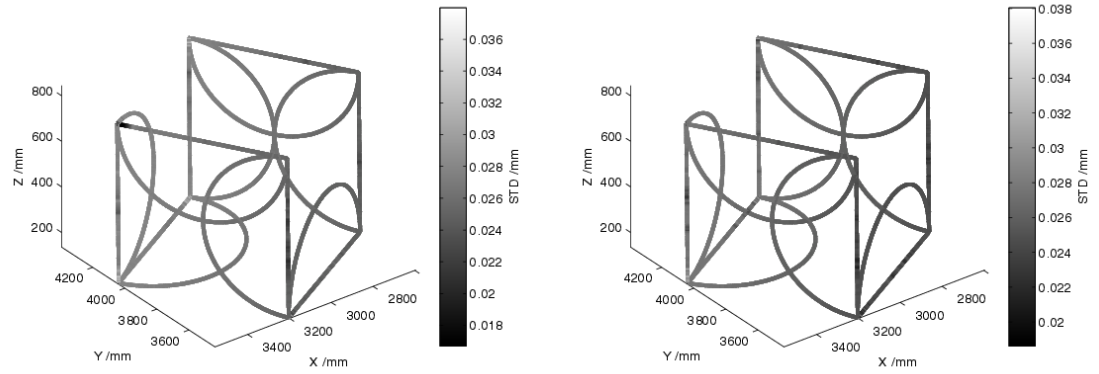

(a) Interacting Multiple Model (IMM) Filter.

(b) Residual-Mean Interacting Multiple Model (RMIMM) Filter.

Figure 5: Hybrid systems analysis methods.

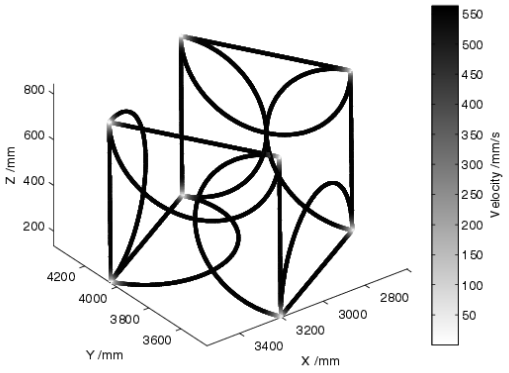

Figure 6: The reached speed for each point of the experiment.

The measurement fusion technique mentioned above is compared with the analysis method where only one laser tracker was used, figure 8 shows the result. This result was obtained with the same IMM filter constellation. It is visible, that the fusion between the two laser trackers LTD500 and AT901 achieves a better state estimation, which is 0.0181 mm. This is an improvement of roughly 25% over the IMM method, based only of the data of the AT901.

6 Conclusion

In the example presented above, of a robot following a trajectory at a constant speed, it has been shown that its analysis as a hybrid system can provide an estimation of the path's uncertainty. Due to the slow speed adopted in the test, it was not possible to determine if the RMIMM filter, in contrast to the more common IMM filter, could achieve its expected faster model detection. However, it was obvious that both hybrid system filters, in conjunction with the augmented measurement model, achieve a significantly better uncertainty estimation than a Kalman filter or the manufacturer's approximation can provide. In particular, the overshoots of the Kalman filter approach can be avoided, which makes the proposed approach suitable for more complex kinematic trajectories. Along with the capabilities of the augmented measurement model to reflect local characteristics, it is possible for the new approach to analyse the trajectory in a more appropriate way. Even if the proposed approach is also suitable for real-time applications, such as integration in a robot control loop, the sampling rate of the laser tracker must be considered.

The results reveal that the alignment errors are more important than synchronisation errors if the delay time is relatively short. This effect is larger in a more far-range application. As the environmental conditions have a significant influence on an electromagnetic beam, it would be useful to have a time-varying refractive index to correct all readings of a

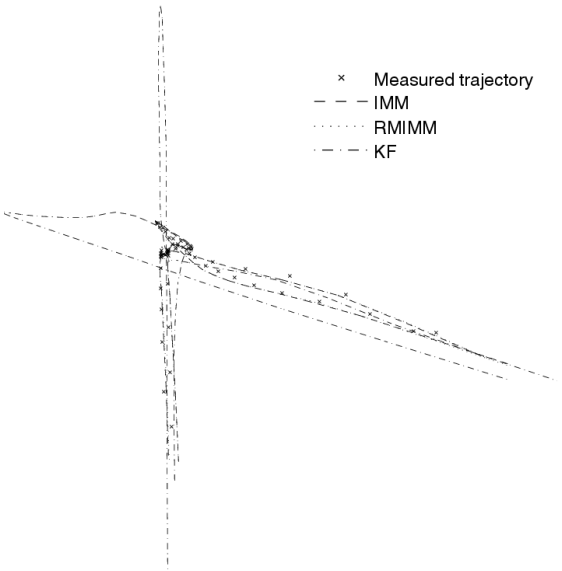

Figure 7: Over shoots provided through the Kalman filter in comparison with the estimation of the hybrid filter algorithms.

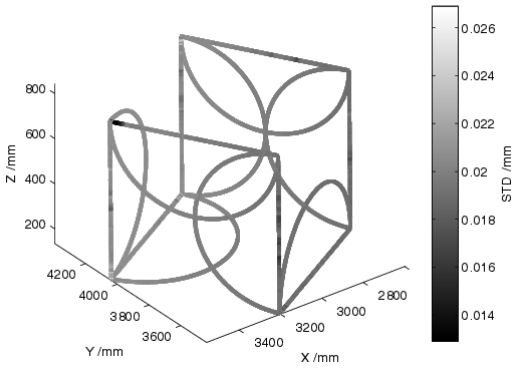

Figure 8: Improved state estimation through the laser tracker fusion.

laser tracker.

Whereas the sensor fusion between two laser trackers achieves an improvement of roughly 25%, the advantage of this method is for large volumes, where one laser tracker can compensate the range dependent uncertainty of the other if the trackers have the right constellation. Apart from that it is important to see that the fusion of a laser tracker with a higher uncertainty than one with a lower uncertainty, achieves an over all improvement of the estimated uncertainty of the state, which is postulated by the Bayesian theory.

However, the analysis of a kinematically measured trajectory with Bayesian filtering, in conjunction with a hybrid system estimator, is a reasonable way to estimate and improve its uncertainty. Nonetheless, it must be remembered that the internal system models must be roughly appropriate to the observed process.

7 Outlook

Bayesian filters rely on the first-order Markov chain assumption which is invalid if there are systematic effects not taken into consideration. It is therefore necessary to generate a kinematic reference to test the measurement model with the objective of identifying additional, missing kinematic parameters which influence the system but are only noticeable at higher speeds.

A benefit of adopting Bayesian filters is that the new proposed approach is well suited for analyzing a trajectory observed by more than one laser tracker. This sensor-fusion approach should lead to a significant lower trajectory uncertainty.

With regards to the coordinated turn model, it is possible here to calculate an approximation of the orientation angles. This approximation could be used to improve a six degrees of freedom (6DoF) estimation, where Leica's T-Cam (6DoF tracking accessory) cannot deliver readings because it has a measuring frequency of 100 Hz instead of the laser tracker's 1000 Hz.

References

[1] Henrik Kihlman, Raimund Loser, Andrew Cooke, Albin Sunnanbo, and Konrad Von Arb. Metrology-integrated Industrial Robots Ű Calibration, Implementation and Testing. In *International Symposium on Robotics (ISR)*, 2004.

[2] Leica Geosystems AG, Leica Geosystems AG Metrology Division Mönchmattweg 5 5035 Unterentfelden Switzerland. *emScon 3.5 Programmers Manual Tracker Programming Interface*, 3.5 edition, August 2009.

[3] Karl Foppe, Volker Schwieger, and Rudolf Staiger. Grundlagen kinematischer Mess- und Auswertetechniken. In *Kinematische Messmethoden Vermessung in Bewegung*, pages 3–18, 2004.

[4] R. Loser. *Weiterentwicklung eines absoluten, hochpräzisen und trackingfähigen Distanzmessers für industrielle Anwendungen*. Mitteilungen. Institut für Geodäsie und Photogrammetrie an der Eidgenössischen Technischen Hochschule Zürich. Inst. für Geodäsie und Photogrammetrie, 2001.

[5] Heiner Kuhlmann. Mathematische Modellbildung zu kinematischen Prozessen. In *Kinematische Messmethoden Vermessung in Bewegung*, pages 19–33, 2004.

[6] E. Garcia, T. Hausotte, and Amthor A. BAYES FILTER FOR IMPROVING AND FUSING DYNAMIC COORDINATE MEASUREMENTS. In *IMEKO*, 2012.

[7] I. Hwang, H. Balakrishnan, and C. Tomlin. State estimation for hybrid systems: applications to aircraft tracking. *Control Theory and Applications, IEE Proceedings* -, 153(5):556–566, September 2006.

[8] Samuel Blackman and Robert Popoli. *Design and analysis of modern tracking systems*. Artech House radar library. Artech House, Boston [u.a.], 1999. Includes bibliographical references and index.

[9] Yaakov Bar-Shalom, X. Rong Li, and Thiagalingam Kirubarajan. *Estimation with applications to tracking and navigation : [theory, algorithms and software]*. A Wiley-Interscience publication. Wiley, New York, 2001.

[10] X. Rong Li and Vesselin P. Jilkov. Survey of Maneuvering Target Tarcking, Part I: Dynamic Models. *IEEE Transactions On Aerospace And Electronic Systems*, 5428(4):1333–1364, 2003.

[11] Matthias Althoff. *Reachability Analysis and its Application to the Safety Assessment of Autonomous Cars*. PhD thesis, Technische Universität München, 2010.

[12] Branko Ristic, Sanjeev Arulampalam, and Neil Gordon. *Beyond the Kalman filter : particle filters for tracking applications*. Artech House radar library. Artech House, Boston, Mass. [u.a.], 2004.

[13] Sebastian Thrun, Wolfram Burgard, and Dieter Fox. *Probabilistic robotics*. Intelligent robotics and autonomous agents. MIT Press, Cambridge, Mass., 2005.

[14] Bureau International des Poids et Mesures. *Guide to the expression of uncertainty in measurement*. International Organization for Standardization, Genève, 1. ed. edition, 1993.

[15] Ning Yang, Weifeng Tian, and Zhihua Jin. An interacting multiple model particle filter for manoeuvring target location. *Measurement Science and Technology*, 17(6):1307, 2006.

[16] M. Montemerlo, S. Thrun, and B. Siciliano. *FastSLAM: a scalable method for the simultaneous localization and mapping problem in robotics*. Springer tracts in advanced robotics. Springer, 2007.

[17] Thomas Emter and Thomas Ulrich. Fusion of geometrical and visual information for localization and mapping in outdoor environments. In *Ubiquitous Positioning, Indoor Navigation, and Location Based Service (UPINLBS)*, oct. 2012.

[18] Raimund Loser. Kinematische Messmethoden im industriellen Nahbereich. In *Kinematische Messmethoden Vermessung in Bewegung*, pages 233–243, 2004.

[19] Harvey B. Mitchell. *Multi-sensor data fusion: an introduction*. Springer Verlag, Berlin, 2007.

[20] Huimin Chen, T. Kirubarajan, and Y. Bar-Shalom. Performance limits of track-to-track fusion versus centralized estimation: theory and application [sensor fusion]. *Aerospace and Electronic Systems, IEEE Transactions on*, 39(2):386 – 400, april 2003.

[21] Duan Zhansheng and X. Rong Li. Optimal distributed estimation fusion with transformed data. In *Information Fusion, 2008 11th International Conference on*, pages 1 –7, 30 2008-july 3 2008.

[22] Dan Simon. *Optimal state estimation : Kalman, H. [infinity] and nonlinear approaches*. Wiley-Interscience, Hoboken, NJ, 2006.

[23] B Muralikrishnan, D Sawyer, C Blackburn, S Phillips, B Borchardt, and W T Estler. ASME B89.4.19 Performance Evaluation Tests and Geometric Misalignments in Laser Trackers. *Journal Of Research Of The National Institute Of Standards And Technology*, 114(1):21–35, 2009.

[24] Ben Hughes, Alistair Forbes, Andrew Lewis, Wenjuan Sun, Dan Veal, and Karim Nasr. Laser tracker error determination using a network measurement. *Measurement Science and Technology*, 22(4):045103, 2011.

[25] Raimund Loser and Stephen Kyle. Alignment and field check procedures for the Leica Laser Tracker LTD 500. In *Boeing Large Scale Optical Seminar*, 1998.

[26] Rainer Joeckel, Manfred Stober, and Wolfgang Huep. *Elektronische Entfernungs- und Richtungsmessung und ihre Integration in aktuelle Positionierungsverfahren*. Wichmann, Heidelberg, 5., neu bearb. und erw. aufl. edition, 2008.

[27] Jcgm. Evaluation of measurement data Ů Supplement 1 to the "Guide to the expression of uncertainty in measurement" Ů Propagation of distributions using a Monte Carlo method. *Evaluation*, JCGM 101:2(September):90, 2008.

[28] Hubert W Lilliefors. On the Kolmogorov-Smirnov test for normality with mean and variance unknown. *Journal of the American Statistical Association*, 62(318):399–402, 1967.

[29] M A Stephens. EDF Statistics for Goodness of Fit and Some Comparisons. *Journal of the American Statistical Association*, 69(347):730–737, 1974.

[30] Leica Geosystems AG, Mönchmattweg 5 CH-5035 Unterentfelden (Switzerland). *Leica Laser Tracker System*, 1999. LTD500.

[31] Thorsten Terboven. Laser Tracker Specification. personal communication via email, August 2012. Hexagon Metrology GmbH.